MECHANICAL PROPERTIES OF SILICON-BASED FILMS FABRICATED BY PECVD

A STUDY OF THE MECHANICAL PROPERTIES OF SILICON-BASED THIN FILMS DEPOSITED BY ECR-PECVD AND ICP-CVD

By

OWEN TAGGART, B.ENG.

A Thesis Submitted to the School of Graduate Studies in Partial Fulfillment of the Requirements for the Degree Master of Applied Science

McMaster University MASTER OF APPLIED SCIENCE (2013)

Hamilton, Ontario (Engineering Physics)

Title: A Study of the Mechanical Properties of Silicon-Based Thin Films

Deposited by ECR-PECVD and ICP-CVD

AUTHOR: Owen Taggart

SUPERVISOR: Professor Peter Mascher

Number of pages: xv, 151

Abstract

Silicon-based dielectric thin films including amorphous hydrogenated aluminium-doped silicon oxides (a-$SiAl_xO_y$:H), amorphous hydrogenated silicon nitrides (a-SiN_x:H), and amorphous hydrogenated silicon carbides (a-SiC_x:H) were deposited by remote plasma chemical vapour deposition (RPECVD) techniques including electron cyclotron resonance plasma enhanced chemical vapour deposition (ECR-PECVD) and inductively-coupled-plasma chemical vapour deposition (ICP-CVD) on silicon (Si) wafers, soda-lime glass microscope slides, and glassy carbon (C) plates. Aluminium (Al) in the SiAlO films was incorporated by way of a metalorganic $Al(TMHD)_3$ precursor.

Thickness, refractive index, and growth rate of the films were measured using variable angle spectroscopic ellipsometry (VASE). Film composition was measured using energy dispersive X-ray spectroscopy (EDX) for the SiAlO films and Rutherford backscattering spectrometry (RBS) for the SiC_x films. Elastic modulus and hardness of the SiAlO and SiC_x films were measured using nanoindentation and their adhesion was characterized via progressive load scratch testing.

All films were observed to be optically transparent at near-IR and red wavelengths with many SiN_x and SiC_x films exhibiting significant optical absorption above 2.25eV. Modification of a previously developed deposition recipe produced doubled growth rates in SiN_x and SiC_x films. SiAlO films were produced with up to 1.6±0.1at% aluninium (Al) incorporation, while SiC_x films with composition ranging from $SiC_{0.25}$:H to SiC_2:H could be produced depending on the growth gas flow ratios. SiAlO films exhibited hardness and reduced modulus (H and E) up to 8.2±0.4 and 75±2GPa, respectively; H and E for the SiC_x films reached 11.9±0.2 and 87±3 GPa. Initially, adhesion to Si wafers was extremely poor with films delaminating at loads of 1.5±0.3N when scratched with a 3/16" alumina (Al_2O_3) sphere; implementation of a rigorous pre-deposition surface cleaning procedure produced films showing only cracking and no delamination up to 30N loads vs. a 200μm radius Rockwell C diamond stylus.

Acknowledgements

This work would not have been possible without the support and guidance of many others. First and foremost I would like to thank my supervisor, Dr. Peter Mascher, for his confidence in my abilities as a researcher, for his insight and suggestions regarding the direction of this work, for making himself constantly available for a quick discussion or email despite an extremely busy schedule, and for delivering the occasional push when it was needed. Without him, this work simply would not exist.

Dr. Jacek Wojcik, our research engineer, first suggested to me to the idea of studying the mechanical properties of films produced using our PECVD reactors; without him, this work might have taken an entirely different direction. I am also grateful for his many lessons ranging from Tauc-Lorentz ellipsometric modelling to how to find a vacuum leak with a bottle of methanol, and for his ceaseless labours in the maintenance and improvement of the reactors.

Shahram Tavakoli, research engineer, was always willing to help me sort out any “stupid nonsense” I ran into with the reactors (or anything else in the lab).

Steve Koprich and Chris Butcher, of the Canadian Centre for Electron Microscopy (CCEM), were very helpful and informative during my time there.

Jack Hendriks and Lyudmila Goncharove assisted with the RBS measurements. I must also thank Sjoerd Roorda and Martin Chicoine for their valiant attempts to find aluminium in my films using HIERDA.

I would like to thank Drs. Ludvik Martinu and Jolanta-Ewa Klemberg Sapieha for making available to me their characterization equipment at the École Polytechnique de Montréal and for providing helpful direction in the mechanical and tribological characterization of my coatings, a field with which I had very little familiarity coming from an Engineering Physics background. Their graduate students Thomas Schmitt and Duanjie Li performed the nanoindentation measurements. Etienne Bousser was very helpful in the interpretation of my scratch and wear test results.

Doris Stevanovic provided valuable cleanroom training and lessons in handling chemicals as well as friendly conversation.

Zahra Khatami and (soon to be Dr.) Patrick Wilson, of my research group, were a pleasure to bounce ideas off or simply have a nice chat with.

Last but not least I would like to thank my parents, William Taggart and Sydne Conover-Taggart, for their support and encouragement when things looked grim as well as my sister Erryl Taggart for her light-hearted conversation and *checking in on me during the writing of this work. Without them, I'm not sure that I ever would have started, let alone finished, the writing of this piece.

Contents

List of Figures

List of Tables

Acronyms

AD	As deposited
APCVD	Atmospheric pressure chemical vapour deposition
ASTM	American Society for Testing and Materials
CASINO	monte CArlo SImulation of electroN trajectory in sOlids
CCD	Charge coupled device
CCEM	Canadian centre for electron micrscopy
CMOS	Complementary metal oxide semiconductor
CVD	Chemical vapour deposition
ECR	Electron cyclotron resonance
EDX	Energy dispersive X-ray spectroscopy
EMA	Effective medium approximation
EPMA	Electron probe microanalysis
ERD	Elastic recoil detection
FCSEL	Functional Coatings and Surface Engineering Laboratory
FTIR	Fourier transform infra-red
HEPA	High efficiency particulate air
HIERDA	Heavy ion elastic recoil detection analysis
IBA	Ion beam analysis
ICP	Induction coupled plasma
IR	Infrared
LAD	Laser ablation deposition
LPCVD	Low-pressure chemical vapour deposition
MEMS	Microelectromechanical systems
MOCVD	Metalorganic chemical vapour deposition
NIR	Near infrared
NRA	Nuclear reaction analysis
PCSA	Polarizer-compensator-sample-analyzer
PECVD	Plasma enhanced chemical vapour deposition
PIXE	Particle induced X-ray emission
PVD	Physical vapour deposition
RBS	Rutherford backscattering spectrometry
RCA	Radio Corporation of America
RF	Radio frequency
RPECVD	Remote plasma enhanced chemical vapour deposition
SEM	Scanning electron microscope
TSD	Triode sputtering deposition
U de M	Universite de Montreal
UV	Ultraviolet
UVOCS	Ultra violet ozone cleaning systems
UWO	University of Western Ontario
VASE	Variable angle spectroscopic ellipsometry
XPS	X-ray photoelectron spectroscopy
ZAF	Atomic number, absorption, and fluorescence

1 Introduction

The study of the mechanical properties of materials is as old as the discipline of engineering. The successful application of any material to a mechanical design problem requires knowledge of its mechanical properties. If the strength of a material is not known or the state of the knowledge is imprecise, producing a safe, efficient design becomes a matter of trial and error rather than a mathematical process and quality assurance becomes impossible. This is obviously impractical, particularly for large projects such as bridges, ships, or buildings. The techniques of materials testing have evolved to meet the ever-increasing requirements of the discipline of engineering. One of the oldest, simplest, and best-known mechanical tests is the tensile test, which has been used to evaluate strength of structural steels since the late 19th century [1].

The importance of mechanical properties and mechanical testing to the world of microelectronics and semiconductor processing is not apparent at first glance. Certainly, knowledge of the mechanical properties of single-crystal silicon was necessary for the fabrication of thin, flat, mechanically stable wafers, but other than the substrate itself one would not expect the materials making up a semiconductor device to experience significant mechanical forces. Materials research in the swiftly growing semiconductor industry was primarily concerned with improving the electronic properties of the devices [2]. But as integrated circuits increased in complexity and the number of processing steps went up, devices began to suffer from a rash of mechanical failures. Observing the example CMOS inverter shown in Figure 1.1, one makes note of the many overlapping thin films of different materials. The conflicting internal stresses present in these films as well as their differing coefficients of thermal expansion generate a multitude of pathways for possible mechanical failure [2].

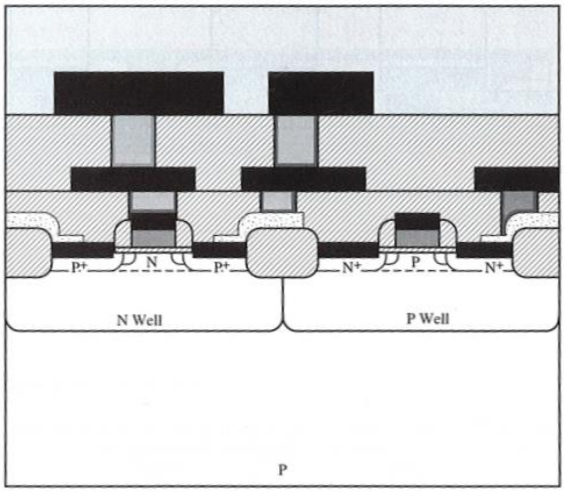

Figure 1.1: A CMOS inverter c. 2000 [3]

The emerging field of microelectromechanical systems (MEMS) also depends on knowledge of the mechanical properties of thin films. In his famous 1959 lecture, “There’s Plenty of Room at the Bottom”, physicist Richard Feynman raised the possibility of manufacturing tiny machines to accomplish tasks like producing tiny parts for computers or performing a heart surgery from the inside out [4]. By 1982, a wealth of tiny mechanical devices including inkjet nozzles, tiny switches, pressure transducers, and accelerometers were being produced using silicon wafers and semiconductor processing [5]. The area of MEMS is now a rapidly evolving field and the design of these tiny structures is increasingly reliant on knowledge of the mechanical properties of silicon and CMOS-compatible thin films.

The discipline of tribology, or the study of surfaces in contact, is based on the laws of friction originally formulated by Leonardo da Vinci as well as the work of Hertz on the contact of elastic solids [6]. The name *tribology* as applied to the study of wear and lubrication appeared around 1968 [7], by which point many important processes for wear reduction particularly on steel surfaces were already well-established. The associated engineering discipline is known as *surface engineering* and a commonly-quoted figure highlighting its importance notes that in 1987, financial losses to the U.S. manufacturing industry resulting from wear were estimated as equivalent to 1-2% of the U.S. GDP [8]. Modern surface engineers work with a wide variety of substrates including ceramics, glasses, metals, and polymers and rely on both conversion and deposited coatings to provide protection from wear, corrosion, chemical attack, and extreme temperatures.

With the demands from the semiconductor industry, MEMS, and surface engineering there has been tremendous advancement in scientific tests for wear behaviour and mechanical properties of coatings. As early as 1909, scientist George Gerald Stoney had observed that electroplated metal films used in the production of glass mirrors tended to spontaneously curl off the substrate above a certain critical thickness [9]. Stoney electrodeposited nickel films on thin sheets of steel, and observed that as the films grew thicker the sheets exhibited an increasing curvature. He concluded that the peeling was occurring due to the presence of enormous tensile stress within the films and developed an equation by which, knowing the thickness of the deposited film, the elastic modulus of the steel substrate, and the degree of substrate curvature it was possible to calculate the internal stress of the film. Stoney's equation is still used today to calculate the stress within films deposited on silicon (Si) wafers [2] albeit in a modified form to account for the circular substrate.

The application of the indentation hardness test to volumes small enough to make imaging impractical, as formalized by Oliver and Pharr in 1992 [10], was a great step forward in the materials testing of thin films. The existence of this new technique of *nanoindentation* made it possible to determine the hardness and elastic modulus of films less than 1μm in thickness, given some knowledge of the properties of the underlying substrate. This made possible the mechanical testing of thin films without removal of the underlying substrate as would have been required by previous tests.

The continuing advancement of MEMS technology requires the development of advanced materials and coating techniques suitable for the production of hard passivation and wear resistant layers on sensitive substrates. This work is a study of several such candidate materials and processes.

1.1 Objective of this Research

The goal of this work was to determine the feasibility of manufacturing protective coatings using remote plasma-enhanced chemical vapour deposition (RPECVD) techniques, with silicon aluminium oxynitride (SiAlON) as a candidate material. While not usually considered for producing wear-resistant coatings due to high complexity, RPECVD has the advantages of low processing temperature (compared to thermal CVD methods) and no damage to the substrate from plasma bombardment (in comparison with direct RF-PECVD). This makes it suitable for coating temperature- or electrically-sensitive substrates which is relevant in, for instance, encapsulation of metallized MEMS sensors [11].

Another goal of the work was to characterize the mechanical and tribological properties of silicon oxide, nitride, and carbide thin films produced by the RPECVD technique. Thus far, the RPECVD systems operated by the author's research group have been mainly used for the production of transparent optical coatings, waveguides, and luminescent silicon materials [12], [13], [14], [15], [16]. Because the mechanical properties of a thin film tend to vary significantly based on the deposition technique and even the individual reactor used for the deposition, information concerning the internal stress and Young's modulus of these films would be invaluable for the fabrication of MEMS devices using the McMaster RPECVD reactors.

1.2 Document Outline

Following this introductory chapter, this document begins by briefly defining the mechanical properties studied during this research (section 2.1) followed by a review of some of the previous work on the mechanical properties of thin-film silicon materials (Section 2.2). It goes on to briefly introduce the underlying theory of the methods by which the thin films in this study were manufactured (Chapter 0) and characterized (Chapter 0). These chapters also include descriptions of the experimental setups used in the work. Chapter 5 discusses the growth and characterization of silicon aluminium oxide (SiAlO) coatings studied as preliminary work for potential SiAlON coating production. Chapter 6 is a summary of some brief experiments on SiN_x coatings performed with the aim of increasing coating deposition rate. Chapter 0 summarizes the later work on optical and mechanical characterization of high-deposition-rate SiC_x coatings. Conclusions drawn from the present work are covered in Chapter 8 and possible directions for future research are covered in Chapter 9.

2 Mechanical Properties of Silicon-Based Thin Films

2.1 Selected Thin Film Mechanical Properties

The study of the mechanical properties of thin films is partly motivated by the discipline of tribology, which seeks to understand the behaviour of surfaces in sliding contact with the goal of minimizing the effects of wear in industrial processes. The discovery that ceramic coating layers only a few μm thick could reduce friction and exponentially extend the lifetime of wear parts spawned a surge of interest in the measurement of the mechanical properties of thin films. The emerging discipline of microelectromechanical systems (MEMS) also has requirements for knowledge of the elastic modulus and internal stress of deposited films, which are necessary in the fabrication of microstructures such as beams and diaphragms.

2.1.1 Elastic Modulus

The elastic or Young's modulus of a material is a measure of its resistance to elastic deformation along the same axis as an applied stress, and can be thought of as representing the stiffness of the material. It can be determined by measuring the slope of a stress vs. strain curve in the elastic regime. In this regime the stress-strain relationship is linear and its slope is the Young's modulus E.

$$\sigma = E\varepsilon \tag{2.1}$$

The standard method for determining the Young's modulus of a bulk metal is the tensile test, in which a sample of the material with a narrow *neck* section between two thicker end sections is stretched by hydraulic or electric motors while the distance is measured by a strain gauge until fracture. This method is not easily applicable to the measurement of the elastic modulus in thin films due to the very small forces involved and the requirement for separation of the film from the substrate. Some of the most common methods for measurement of thin film elastic moduli are shown in Figure 2.1.

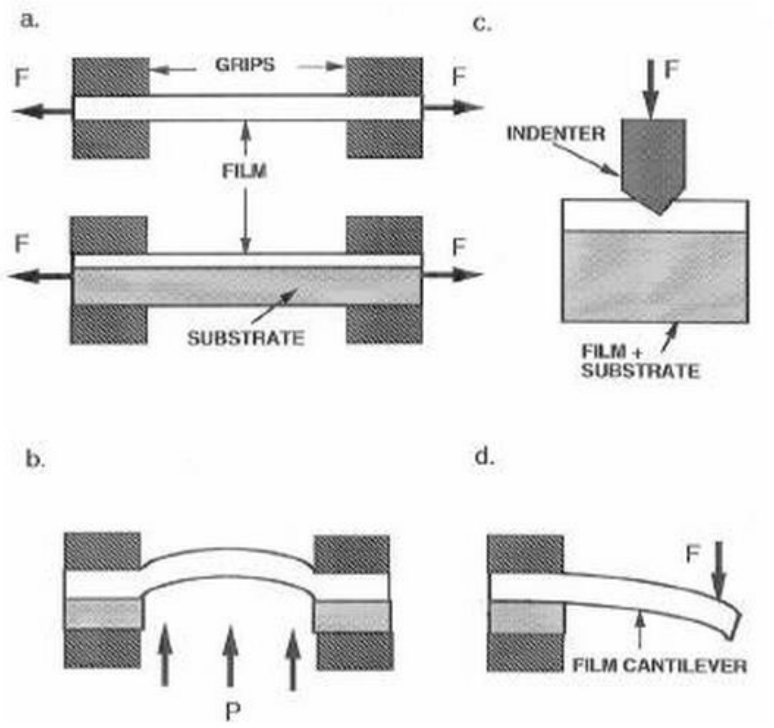

Figure 2.1: Common mechanical test methods for thin films [17]

In general, application of the tensile test (*a*) to thin film specimens is extremely problematic in practice due to even tiny loads producing massive stress in a thin film. The resulting strains will also be tiny and difficult to measure.

Performing the test with the substrate still attached leads to a host of difficulties in ensuring uniform stress throughout the system and separating effects of the substrate from those of the film [17]. The bulge test (*b*) is very commonly used in MEMS work where the problem of a free-standing membrane often arises, and can be used to determine Young's modulus as well as yield strength and Poisson's ratio of the film [18]. As is the case for the tensile test, careful sample preparation is very important. The indentation test (*c*) has an advantage in that it is applicable to a wide variety of sample geometries; for more details regarding the nanoindentation test, refer to section 4.4 of this work. A variant of the indentation test is the beam deflection test (*d*) which aims to eliminate some of the effects of the substrate on the modulus measured using indentation, but of course requires more sample preparation.

2.1.2 Hardness

Hardness is a measure of a material's resistance to plastic (permanent) deformation under an applied load. The most commonly used value for classifying hard materials such as ceramic coatings is the indentation hardness. This hardness is determined by pressing a rigid body known as the indenter of a fixed geometry into a specimen of the material under test, inducing plastic deformation in the tested material. The indentation hardness is then defined by the ratio of the size of an applied load to the surface area or projected area (depending on test standard) of the resulting impression. The measured hardness of a material is influenced by the test parameters including the size of the load and the shape of the indenter, so a variety of standardized indentation tests have been defined to provide standards by which materials can be compared. The most common tests are the Brinell, Vickers, Knoop, and Rockwell hardness tests. A more detailed description of these techniques can be found in [19], but all of them rely on regular indenter geometry and direct measurement of the side length or radius *a* of the plastically deformed region left the indenter (Figure 2.2).

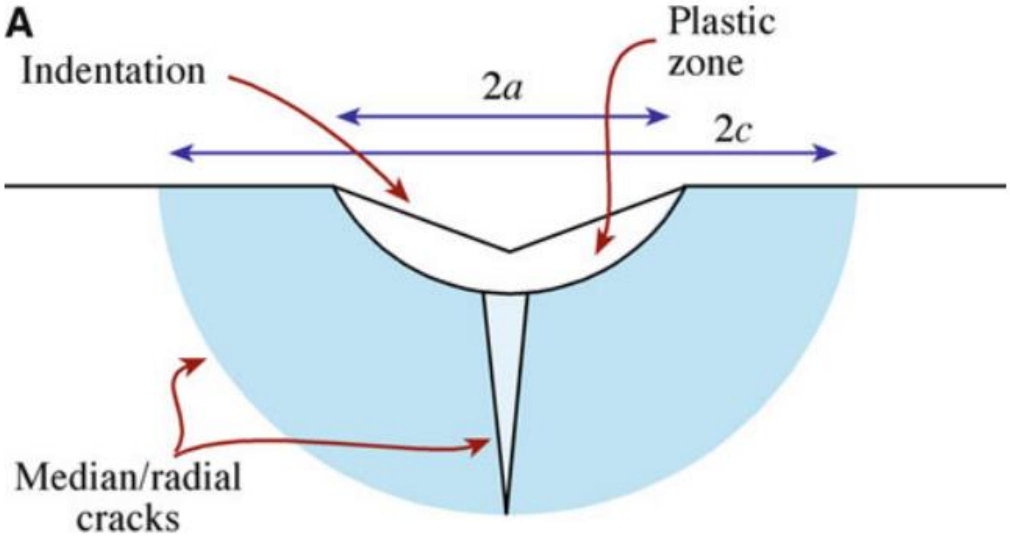

Figure 2.2: Plastically deformed region and cracking after indentation [19]

If the indentation produces regular cracks, the fracture toughness of the material can be determined from their length. In the thin film case the size of the plastic zone left by the indentation is generally too small to be conveniently measured directly. The nanoindentation technique uses force- and displacement-sensing transducers to circumvent this requirement; for a more thorough description of the technique, refer to section 4.4 of this work.

Classically, it was expected that hardness as a measure of resistance to plastic deformation would be strongly indicative of a material's wear performance. In recent years, it has been found that the ratio of a material's hardness H to its elastic modulus E was a strong predictor of the wear rate in many practical situations including impact, erosive, and abrasive wear [20]. This is counterintuitive in that sometimes relatively "soft" materials will have superior protective characteristics to "hard" but stiffer materials. H/E is representative of the ability of a material to accommodate elastic deformation without plastic failure, which may in some cases be higher for materials with low E.

2.1.3 Adhesion

Physically, adhesion is defined as the amount of energy per unit area needed to separate a coating from the substrate. The most fundamental definition of adhesion is based on the thermodynamic concept of surface energy. During delamination, the film-substrate interface with energy γ_{fs} is replaced by an equivalent area of film-ambient interface with energy γ_{fa} and substrate-ambient interface with energy γ_{sa}. The work of adhesion W_A per unit area is defined as

$$W_A = \gamma_{sa} + \gamma_{fa} - \gamma_{fs} \tag{2.2}$$

Most practical test methods for adhesion actually measure the *force* of adhesion rather than the work. It is, of course, impossible to relate force of adhesion to work of adhesion without knowledge of the path followed by the force as it debonds the coating [21]. It is intuitive that achieving good adhesion is critical to the performance of any film-substrate system, since a coating which does not stick to the coated surface is of no value whatsoever. Theoretical understanding of adhesion is still a rapidly evolving area, partly due to the many different possible interface types between a coating and the substrate (Figure 2.1).

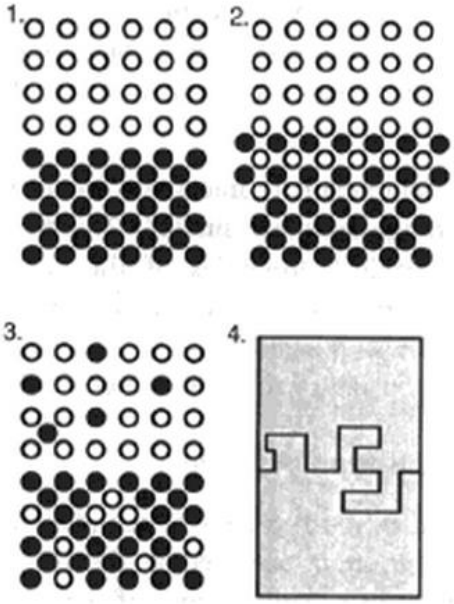

Figure 2.3: Abrupt, compound, diffusion, and mechanical interfaces [17]

Abrupt interfaces (1) form when the two materials are not chemically compatible and little diffusion occurs (for example due to low solubility or growth temperatures) and typically exhibit poor adhesion. Compound interfaces (2) formed by chemical reaction between the surfaces may also be brittle due to stresses induced by change of volume during the reaction. Diffused interfaces (3) and mechanically interlocked interfaces (4) tend to exhibit the best adhesion. In general, a clean surface is expected to exhibit superior adhesion to a contaminated one but this situation may occasionally be reversed [17].

Two of the most common practical tests for thin film adhesion are the pull test and the tape test (Figure 2.4).

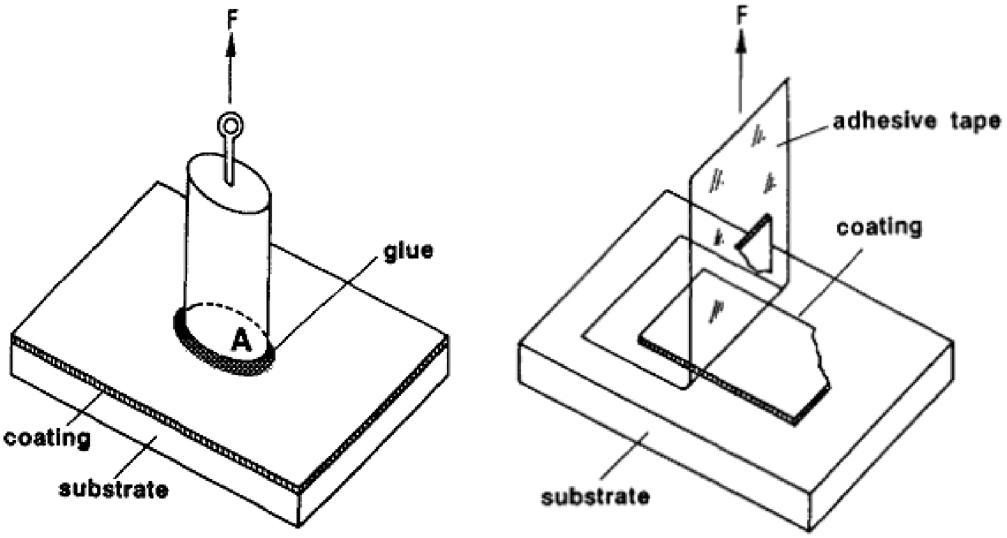

Figure 2.4: Pull adhesion test (left) and tape test (right), reprinted from [22]

The tape test, which can even be performed using common Scotch tape, is an excellent initial qualitative assessment of coating adhesion while the pull test can provide quantitative data (force of adhesion per unit area). The pull test's applicability is limited by the strength of the adhesive bonding of the tester to the film's surface, which can be on the order of 70MPa [22]. For thin, hard, well-adhering coatings such as those applied to metals by high-temperature CVD, it is frequently the case that neither the tape test nor the pull test will produce debonding of the film. In this case it is necessary to move to scratch adhesion testing, which is discussed further in Section 4.5 of this work.

2.1.4 Wear Resistance

The measured wear resistance of a material is representative of its ability to withstand service in harsh environments such as machine tool heads, gear surfaces, or turbine engines. Since it may be difficult, expensive, or involve a prohibitively long period of time to accurately simulate service conditions of a material, standard wear tests such as the pin-on-disk and slurry test were developed. There are currently ASTM wear testing standards for a wide variety of materials and test methodologies [23]. The existence of standardized wear tests also enables simple comparison between different material and coating systems. The selection of a test method is generally based on the properties of the material contact in the application (metal-metal, metal-plastic, metal-ceramic, dry, lubricated, sliding, rolling, etc.)

Probably the simplest wear test to implement is the pin-on-disk, in which a ball of a hard material is pressed by a constant load against a rotating test specimen. The instrumentation and setup for this test is discussed in more detail in section 4.6. Even for this simple case, the interactions between surfaces in dry or lubricated sliding contact are extremely complex and evolve over time as the surfaces are worn. Wear may occur by a variety of different mechanisms or through several at once, and the type wear experienced is often dependent on the sliding speed and applied load. In a 1983 study on the wear behaviour of thin films, Halling [24] identified at least six major types of wear including oxidative, adhesive, abrasive, fatigue, delamination, and pitting wear. The mode of wear observed depends on the mechanical and chemical properties of the two materials in contact as well as the ambient environment and temperature. In many cases chemical reactions between the surfaces play a role in the wear behaviour.

In general, wear resistance is quantified in terms of the wear rate, which is the volume of material removed during a sliding contact for a given distance and load. The units of wear rate are $mm^3/(N*m)$, and as with hardness the value measured will be dependent on the extrinsic parameters of the test as well parameters of the coating and substrate.

2.2 Studies of Silicon-Based PECVD Thin Films

In general, the mechanical properties of any thin film material will be strongly dependent on the temperature used for its deposition. Because plasma-enhanced chemical vapour deposition (PECVD) processes usually take place at low temperatures (100-350°C), the Si-based dielectrics deposited tend to be amorphous with significant hydrogen incorporation [25]. These amorphous hydrogenated films can be expected to have significantly poorer mechanical properties than poly- or mono-crystalline films with lower H incorporation produced at higher temperatures by methods such as low-pressure chemical vapour deposition (LPCVD). Their advantage lies in the suitability of low process temperatures for the coating of a wide variety of sensitive substrates.

The principal motivating factor for the study of the mechanical properties of silicon-based dielectric films is their application to MEMS systems designed for harsh environments. A wealth of knowledge exists regarding the growth and processing of silicon materials. Very few studies have been performed regarding the application of PECVD silicon materials as wear protective coatings. Many of the possible materials systems including silicon nitride (SiN_x), silicon carbide (SiC_x), silicon carbon nitride (SiC_xN_y), and silicon aluminium oxide (SiAlON) exhibit excellent mechanical properties including hardness, modulus, and toughness as bulk ceramics but these advantages do not always translate to the amorphous hydrogenated films deposited by methods like PECVD.

2.2.1 Silicon Aluminium Oxynitride (SiAlON) Films

The mechanical properties of SiAlON thin films have received little study. Most of the early work on this materials system was motivated by the potential application of silicon nitride (Si_3N_4) as a structural material for high-temperature ceramic turbine engines [26]. Si_3N_4 is unusual among ceramics in that it has relatively high fracture toughness in addition to high hardness. Fabrication of fully-dense shapes of sufficiently pure Si_3N_4 is difficult and expensive due to the high temperatures and purity required. It was discovered that ceramic parts based on "alloys" of Si_3N_4 and alumina (Al_2O_3) were easier to fabricate than Si_3N_4 with similar mechanical properties. Figure 2.5 is a phase diagram of the SiAlON materials system highlighting the commercially important *β'*, *O'*, and *X* phases.

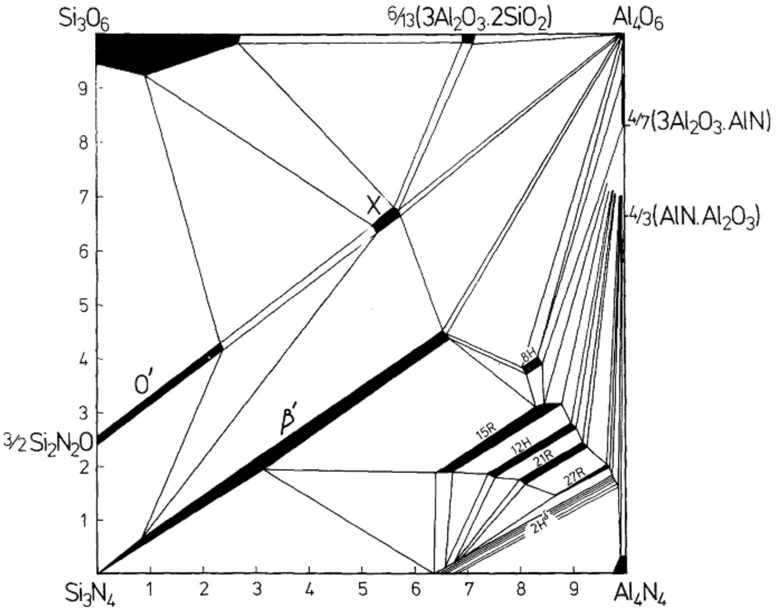

Figure 2.5: Phase diagram of the SiAlON ceramic system reprinted from [26]

Typically, these SiAlON bulk ceramics have similar crystal structure to the parent silicon material e.g. *O'*-phase SiAlONs can be understood as silicon oxynitrides Si_2N_2O with some proportion of Si atoms substituted by Al and N atoms substituted by O [27]. Of course, SiAlON thin films fabricated by methods such as sputtering and CVD are likely to be amorphous up to very high temperatures and non-stoichiometric composition can be expected.

More recently, the application of rare-earth doped SiAlON ceramics as phosphor materials has been investigated. The addition of oxides of rare earth metals such as cerium (Ce), praseodymium (Pr), europium (Eu), and terbium (Tb) in the sintering of SiAlON ceramics produces materials with photoluminescence peaking in the green, yellow, or orange region [28], [29], [30]. These phosphors have excellent thermal and chemical stability and tunable luminescence and are intended for use in the production of warm-white LEDs based on existing blue LED technology [30], [31], [32], [33].

Dreer et al. made a comparative study of compositional analysis methods including electron probe microanalysis (EPMA) for the simpler AlO_xN_y and SiO_xN_y thin film materials systems [34]. It was found that, when standardized using materials of known and similar composition such as quartz (SiO_2), corundum (Al_2O_3), and stoichiometric silicon nitride (Si_3N_4), the EPMA gave repeatable composition measurements with relative standard deviation as low as 10% even for films containing <5% Al, O, or N and agreed within uncertainty with results obtained by more precise ion beam analysis methods [34].

Dreer et al. also studied the deposition of aluminium oxynitride films by reactive DC magnetron sputtering of Al targets in O_2 and N_2 atmospheres [35]. A matrix of 26 films deposited at varying plasma power and flow rate of Ar, O_2, N_2 were evaluated for refractive index, deposition rate, hardness, and Young's modulus. Statistical modelling was used to extract the dependence of film characteristics on the various deposition parameters. A linear dependence of refractive index and hardness of the resulting films on percentage oxygen incorporation (Figure 2.6) was observed, with both index and hardness decreasing with increased O content. Growth rate was found to be strongly dependent on the sputtering power.

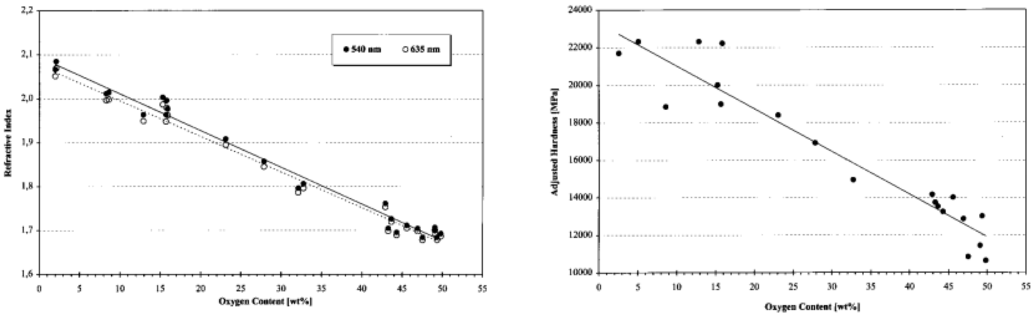

Figure 2.6: Index (left) and hardness (right) of AlON films, reprinted from [35]

2.2.2 Silicon Nitride (SiN_x) Films

The majority of work on the mechanical properties of SiN_x films has focused on the commercially-important magnetron sputtering and LPCVD processes. Both LPCVD [36], [37] and sputtered [38] SiN_x have found application as building materials in MEMS. The sputtering technique relies on energetic plasma bombardment of the growing film to desorb hydrogen and induce densification. SiN_x films with hardness and Young's modulus measured using nanoindentation to be as high as 23GPa and 210GPa, respectively, have been produced by this method [39], [40]. In LPCVD, growth temperatures as high as 800°C [41] densify the film in a manner similar to the plasma bombardment in sputtering. Films with H as high as 35GPa [42] and E as high as 325GPa [37] (H and E measured by nanoindentation) have been produced with LPCVD.

While investigating methods for extracting the true hardness and modulus of a thin film from the composite values measured during nanoindentation of a thin film on a substrate, Jung et al. present hardness and elastic modulus (H and E) values for both LPCVD and PECVD SiN_x thin films [42]. They estimated that the dense LPCVD films measured had H=35.0±0.3GPa and E=266±4GPa while the low-temperature PECVD films had H=11.5±0.5GPa and E=119±3GPa and ascribed the poorer mechanical properties of the LPCVD film to lower density or higher porosity.

A study by Winchester and Dell [43] on PECVD silicon nitrides prepared from SiH_4, NH_3, and N_2 found that the elastic modulus of the films as measured by nanoindentation depended mainly on the deposition temperature, with gas flow ratios playing a secondary role. They observed a positive linear correlation of elastic modulus with growth temperature (Figure 2.7).

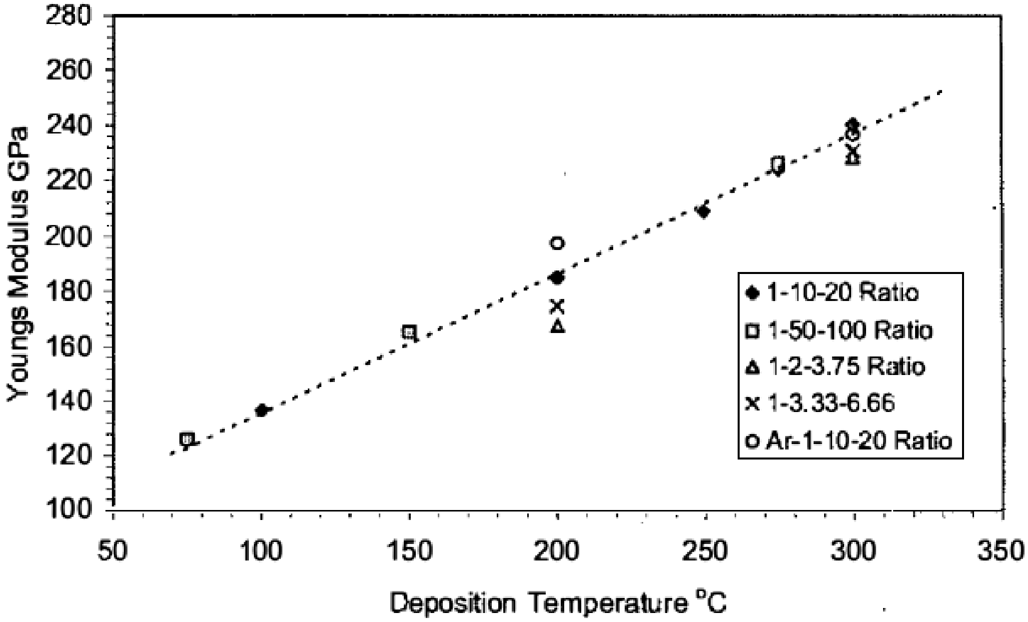

Figure 2.7: Modulus of SiN_x films grown with SiH_4:NH_3:N_2 [43] © 2000 IEEE

In a study of the mechanical properties of low-temperature PECVD silicon nitride films produced from SiH_4, NH_3, and N_2 on a commercial (Oxford Instruments) RF-PECVD reactor, Huang et al. [44] reported a strong dependence of the H and E on the density of the films, with the most dense films exhibiting H~22GPa and E~200GPa as measured by nanoindentation. For comparative purposes, an LPCVD SiN_x film with much higher density was also studied. Density measurements were performed using the change in resonant frequency of a quartz crystal oscillator, and compositional measurements were performed using energy dispersive X-ray spectroscopy (EDS). The density of the films was observed to increase linearly with the ratio of Si:N (Figure 2.8), but the study did not extend to the Si-rich nitrides with Si:N>0.75.

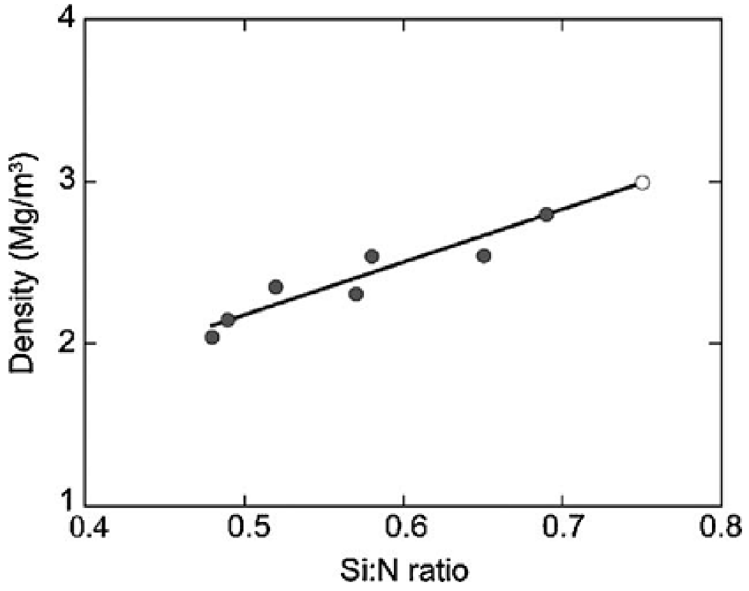

Figure 2.8: Density of PECVD SiN_x film vs. S:N ratio, reprinted from [44]

Wu et. al. studied the effects of rapid thermal annealing (RTA) on the mechanical properties (stress, *H*, and *E*) of SiN_x films produced by both sputtering and PECVD [45]. They found that annealing up to 600°C significantly increased the tensile stress in the PECVD films, regardless of their initial stress state. Further increase in the annealing temperature was seen to reduce the tensile stresses. *H* and *E* for both types of films, as measured by nanoindentation, were seen to increase significantly with annealing temperature. The greatest effect was observed above 400°C, indicating densification by reduction of porosity or drive-off of hydrogen above this temperature. The elastic modulus of the PECVD nitrides was particularly sensitive to the effects of the annealing (Figure 2.9).

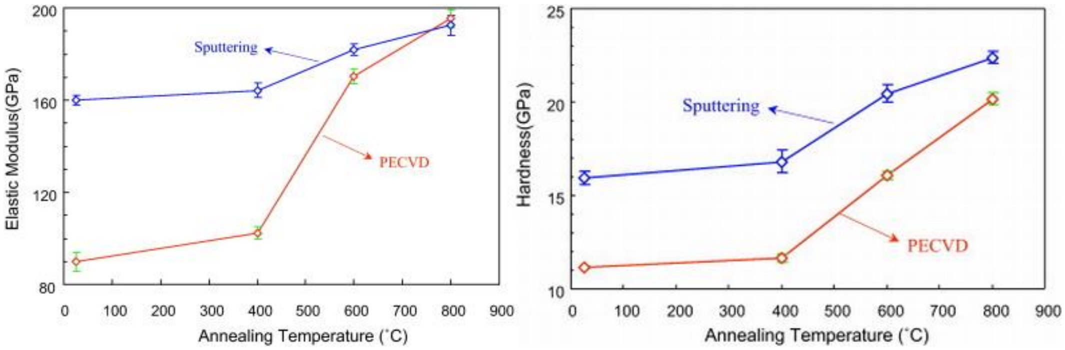

Figure 2.9: *H* and *E* of PECVD SiN_x films after annealing, reprinted from [45]

2.2.3 Silicon Carbide (SiC_x) Films

Interest in the mechanical properties of *a*-SiC_x films stems primarily from the possibility of their application to MEMS devices, but there also exist studies on their tribological properties. Due to its combination of excellent mechanical, electrical, chemical, and thermal properties with CMOS-compatible growth techniques, SiC is a very promising candidate for the next generation of harsh-environment and high-temperature MEMS sensors [46], [47]. As with SiN_x films much of the work on the mechanical properties of these materials has focused on films produced by sputtering [48], [49], [50] and LPCVD. Sputtered SiC_x films are generally amorphous and nanoindentation measurements of *H* and *E* up to 27GPa and 255GPa have been reported [50], while LPCVD carbides can be grown in polycrystalline form [51], [52], [53]. There is also a significant body of work on low-temperature PECVD deposition of SiC.

El Khakani et. al. performed nanoindentation and bulge testing to determine the hardness, Young's modulus, and Poisson's ratio of *a*-SiC and *a*-SiC:H deposited by three methods including RF-PECVD [25]. Film composition was determined using FTIR analysis. They found that hardness and Young's modulus of the PECVD films were composition-dependent and reached a maximum around 20GPa for *a*-Si_xC_{1-x} films with x~0.5, or near-stoichiometric composition. They observed a linear dependence of *H* and *E* on the Si-C bond density determined using FTIR. Si-rich or C-rich films exhibited significant Si-Si or C-C bonding, respectively, and poorer mechanical properties. They also characterized *a*-SiC films without H incorporation produced by triode sputtering deposition (TSD) and laser ablation deposition (LAD); in comparison the PECVD *a*-SiC:H films exhibited much lower *H* and *E*.

Flannery et. al. investigated the mechanical properties of PECVD amorphous carbides produced by a dual-frequency reactor as part of a study on their feasibility for use in chemically-resistant MEMS sensors [54]. They observed lower values for *H* and *E* than reported in [25]. They found the films to be very resistant to the etching action of many common semiconductor processing chemicals including sulfuric acid (H_2SO_4), hydrofluoric acid (HF), and potassium hydroxide (KOH). They also fabricated MEMS sensor devices using the film including pressure sensors, microfluidic channels, and electrochemical sensors as well as demonstrating its utility as an etch mask by fabricating deep, narrow etched channels in glass protected by the films [54].

A study by Daves et. al. on the application of PECVD *a*-SiC coatings to harsh environment MEMS sensors measured stress and composition of coatings produced from a mixture of silane (SiH_4) and methane (CH_4) [11]. They observed that based on their X-ray photoelectron spectroscopy (XPS) measurements, approximately stoichiometric carbides could be produced at a SiH_4/CH_4 flow ratio of 0.25 (Figure 2.10).

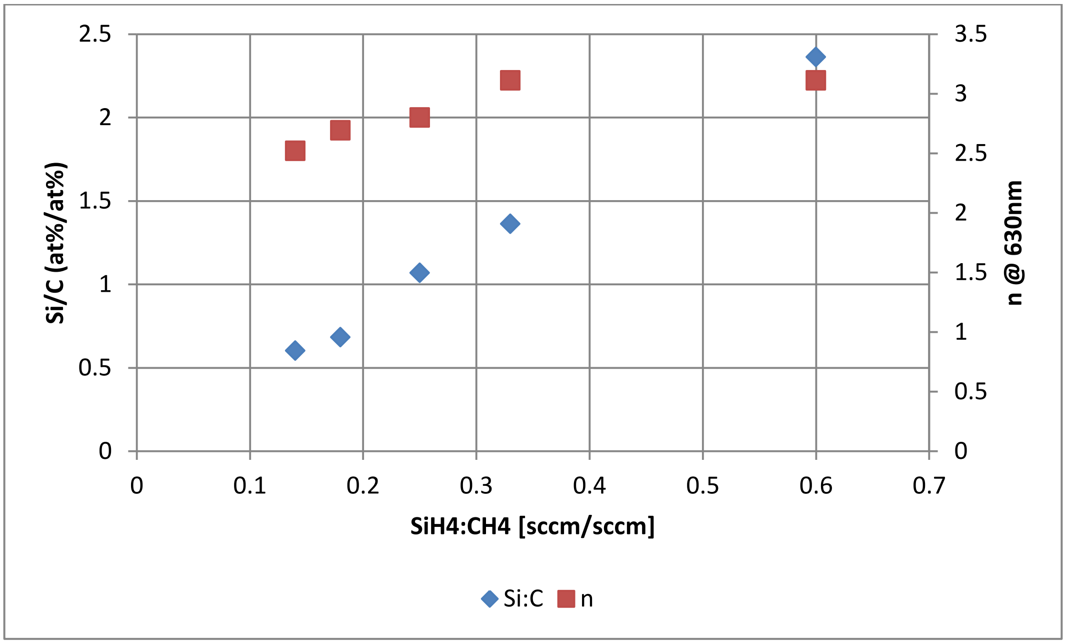

Figure 2.10: Index and stoichiometry of PECVD *a*-SiC_x films, after [11]

They concluded that of film compositions studied, these near-stoichiometric films had the best properties for their application (high-temperature passivation layers). During micro-scratch adhesion characterization of the coatings, they observed that scratch critical load actually increased from 40mN to 51mN after a 100h anneal in N_2 at 600°C. They also demonstrated the superiority of an oxide/carbide dual-layer passivation stack to conventional passivation coatings including *a*-SiO_x and *a*-SiN_x in high-temperature oxidizing environments.

Porada et. al. found that in spite of the low *H* and *E* (10GPa and 118GPa) of PECVD *a*-SiC_x coatings produced from methyltrichlorosilane (*H* and *E* measured using nanoindentation), the coatings exhibited good wear resistance and low friction compared to Si wafers when measured using a Calowear ball-on-flat tester [55]. The enhanced wear resistance was ascribed to smooth plastic deformation caused by frictional heating of the PECVD coatings due to their low thermal conductivity.

3 Sample Growth and Preparation

3.1 Substrates

To produce a uniform thin film suitable for characterization by the methods used in this work, a substrate is required to be flat with a smooth (micron or nanometre scale roughness) surface free of contaminants. When designing an experiment to characterize a given property of a thin film, it is important to choose a substrate suitable for the selected characterization technique. Optical measurements may require a transparent substrate. Some substrates may exhibit their own photoluminescence, interfering with photoluminescence measurements of the film. Electrical measurements usually require a conductive substrate, and the elemental composition of the substrate is important when attempting ion beam analysis of the film. For mechanical characterization, it is important to have a clean surface prior to deposition and its mechanical properties of the substrate should be well-known.

The most common substrate for MEMS and microelectronics work is the silicon wafer. Wafers are single crystals of ultra-high-purity electronic grade silicon. Their surfaces can be polished to nm-range smoothness by a process known as chemical-mechanical polishing. Wafers are categorized by their diameter, thickness, doping type and resistivity, surface polish, and the crystallographic orientation of their surface (with the most common being <100> and <111> surfaces). The <100> wafer is the most commonly used in microelectronics because of the ease of cleaving or dicing it into square or rectangular pieces. In fact, <100> Si wafers can be easily and precisely cleaved into smaller pieces by hand due to their tendency to fracture smoothly along a crystallographic plane. The surface orientation does however influence the surface energy of the wafer.

The CVD systems used for film production in this work accept 2” and 3” Si wafers. Silicon wafer substrates are relatively inexpensive and easily available. Of the substrate materials used in this work, Si wafer surfaces have the best understood surface characteristics and well-known cleaning procedures for them exist. Si wafers are also thermally stable up to beyond 1200°C and exhibit limited thermal expansion, making them well-suited for high-temperature annealing. The doping type of a wafer is important when designing electrical measurements and some heavy *n*-type dopants such as antimony (Sb) may interfere with RBS characterization if they are present in high levels. If scratch testing is to be performed on the film, thin (300 μm or less) wafers are generally not suitable due to the potential for them to cleave during the test.

Another common choice of substrate is glass. Nearly all glasses are in fact based on silica (SiO_2), with quartz being nearly pure silica. The most common and inexpensive type of glass is soda lime glass, which is the type found in windows and glass bottles. Soda lime glass is mostly SiO_2 and also contains significant amounts of sodium oxide (Na_2O, or *soda*) and calcium oxide (CaO, or *lime*). The extremely flat, smooth surface is produced during manufacture of the glass when molten precursors are flowed in a smooth sheet over a bath of molten tin, which is known as the *float glass process*. Soda lime glass as a substrate is extremely inexpensive and is transparent to visible light, but the presence of many different elements in significant quantity interferes with compositional characterization. It also exhibits high thermal expansion and has a low melting point near 700°C with significant softening at temperatures above ~500°C. Glass surface coating is a massive industry. As a result surface cleaning procedures for glass, while well-known, are not always public knowledge.

Glassy carbon is a specialized choice of substrate. First observed in 1951 [56], glassy carbon is formed when polymers are heated to temperatures ~2000°C in an inert atmosphere. It appears as a smooth, hard, flat, opaque black glass. It is a very pure material and widely used in organic chemistry experiments, but is relatively expensive compared to Si wafers or glass. It is also thermally stable. Surface cleaning procedures are not as well understood either. The principal advantage of using glassy carbon substrates relates to ion beam analysis, where the low atomic mass of carbon reveals elemental features in the film that might otherwise have been masked by the substrate signal.

3.2 Surface Cleaning

The importance of a clean substrate surface to the success of any vacuum coating experiment cannot be overstated. Surface contaminants may lead to poor film adhesion, impure films, micro- and macro-scale structural defects, and electrical defects at the film-substrate interface. Nevertheless procedures used for cleaning in the research arena are often poorly defined or based simply on trial and error.

The best-known procedure for Si wafer cleaning is the RCA clean, which was developed by Werner Kern around 1965 and first published in 1970 [57]. In a review paper on the subject [58], Kern identifies three major types of surface contamination that may occur during wafer processing: contaminant films, contaminant particles, and adsorbed gases. Contaminants may be additionally subdivided into organic and inorganic compounds. In addition, the protective thin oxide layer naturally formed on Si surfaces in atmosphere (native oxide) may in some circumstances be considered a contaminant. Organic compounds are particularly harmful to adhesion and during thermal treatment may nucleate SiC, while metal ions may impact epitaxial growth and interfere with electrical properties [58]. The RCA clean was developed to produce a standardized cleaning procedure that would consistently yield clean surfaces. It has two major steps with additional optional steps before, between and after.

First, the wafers are immersed for 10min in a bath of aqueous hydrogen peroxide and ammonium hydroxide (5 H_2O:1 H_2O_2:1 NH_4OH) at 75-80°C. This step is known as Standard Clean 1 (SC-1) and is mainly used to oxidize organic contaminants as well as some metals. In the second step (SC-2), the bath used is aqueous hydrogen peroxide and hydrochloric acid (6 H_2O:1 H_2O_2:1 NH_4OH), which is also performed for 10min at a temperature of 75-80°C. This step is intended to remove all remaining metallic contaminants. Both steps will leave a thin protective oxide on the Si surface, and this oxide may trap some contaminants. It may therefore be removed before step 1 or between steps by the application of an ultrapure hydrofluoric acid (HF) solution, but it is important to remember that HF-stripped Si surfaces lack the protective oxide layer and will almost immediately become contaminated [58].

For wafer surfaces with gross organic contamination (such as photoresist films or other visible contaminants), a degreasing procedure prior to RCA cleaning is generally beneficial. If organic solvents such as acetone, methanol, or trichloroethylene are used it is generally in an ultrasonic bath. The ultrasound aids in the cleaning process by inducing cavitation (nucleating bubbles) at the surface and thereby lifting particles. Since solvents may leave behind contaminants of their own, such a step is typically followed by ultrasonic treatment in deionized water. An alternative for degreasing is the “piranha” solution which is a 2:1 or 3:1 mix of H_2SO_4:H_2O_2. Like SC-1, it oxidizes and removes organic complexes and piranha cleaning is often performed at elevated temperatures.

An alternative or supplementary method for removing organic contaminants is the UV/ozone or UVOCS process. Reaching its final form during the research of Vig et. al. in 1976 [59], the process exploits the ability of ultraviolet light to break down complex polymers such as photoresist and other organic contaminants. When the ultraviolet cleaning is performed in an oxygen-containing atmosphere, the ultraviolet light also produces ozone which aids in the cleaning process by oxidizing the polymers into more volatile organic complexes. The combined action of UV light and ozone was found to be vastly more effective than either acting alone. The apparatus used by Vig et. al. in these experiments was very simple and consisted of an airtight metal box with a short-wave UV source such as a mercury (Hg) discharge lamp in the roof. When supplied with a fused-silica window, which is transparent at short-wave UV wavelengths, the Hg lamp will have strong emission at both 185nm and 254nm. The shorter wavelength is responsible for the generation of ozone while the longer one is important for driving the breakdown and oxidation of the polymer contaminants. Modern UV/ozone cleaning systems use the same concept.

Contamination of sample surfaces in the research lab comes from sources such as plastic sample containers, human operators, handling tools such as tweezers and wafer carriers, and almost anything else. An often-neglected additional source of contamination is the vacuum deposition chamber itself. As stated before, Si surfaces stripped of their native oxide by HF are highly reactive. This reactivity is beneficial for film growth but also attracts contamination. The deposition chamber will always contain some organic molecules from pump oil as well as N_2 and water vapour from residual atmosphere. In addition to interfering with adhesion, these contaminants may be broken down by the plasma and incorporated into the growing film. Their effect can be minimized by incorporating an overnight degas step into the growth, in which the sample is kept in a vacuum at high temperature while the pumps evacuate the chamber.

As a final cleaning step before deposition, a plasma surface activation step is often included. O_2 plasma has a similar effect to oxidizing chemicals and can be expected to remove some organic contamination from the sample surface. Likewise, the reducing effect of H_2 plasma may form volatile metal hydrides and thereby remove some metallic contamination. Native or other oxide may be stripped from Si surfaces by fluorine-containing plasma such as CF_4 or NF_3. Finally, sputter cleaning, which is erosion of surface layers by energetic plasma bombardment, is effective in removing all types of contaminants but will roughen the surface.

3.3 Plasma Enhanced Chemical Vapour Deposition (PECVD)

Chemical vapour deposition (CVD) refers to a broad array of thin film growth techniques of which the common feature is the chemical reaction of gaseous chemicals in a confined space to form solid film on exposed surfaces. Silicon materials commonly produced by CVD include amorphous silicon (*a*-Si), polycrystalline silicon (poly-Si), silicon oxides (SiO_x), and silicon nitrides (SiN_x). Classically, the CVD growth process is understood as consisting of at least six distinct steps (Figure 3.1): reactant introduction (A), activation and diffusion to the substrate (B), physical adsorption on the substrate (C), the actual film-forming reaction (D), desorption of gaseous reaction products such as H_2 (E), and removal of the by-products (F).

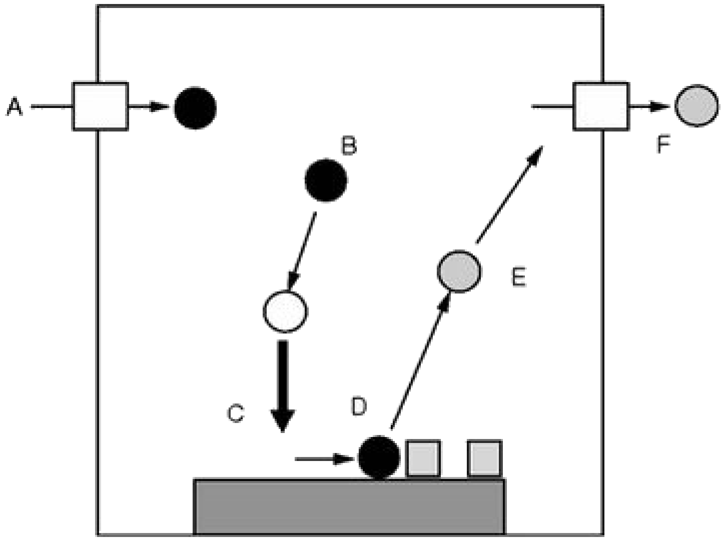

Figure 3.1: Conceptual diagram of CVD growth [60]

Of course, the real picture is vastly more complex. Reactions may occur in the gas phase rather than on the substrate; volatile by-products may be trapped by the growing film instead of desorbing; contaminants in the reaction chamber may become activated and react with the precursors to produce an impure film. Furthermore, it is intuitive that because the gaseous precursors fill the entire volume of the reaction chamber the growth reaction will occur not only on the substrate but on any exposed surface. This is actually one of the great strengths of CVD in contrast with physical vapour deposition (PVD) processes: it is a non-line-of-sight process. This enables the coating of complex surfaces as those of drill bits or gears. Furthermore, the composition of the grown film can be adjusted simply by varying the flow rates of the gaseous precursors and it very simple to grow non-stoichiometric films or multi-layer structures in this way.

In atmospheric pressure CVD (APCVD), a flow of reactant gases is provided to a closed reaction tube and displaces the atmosphere within. However, it is also possible to connect a vacuum pump to the chamber during growth and run the reaction at much lower pressure (LPCVD). Decreasing density of gas in the chamber enables operation in the molecular-flow regime rather than the viscous-flow regime. This creates a much more uniform distribution of reactants and eliminates the effects of precursor flow dynamics on growth. Figure 3.2 shows a generic tube-furnace style LPCVD reactor. The uniformity of the LPCVD process enables the simultaneous coating of large batches of parts.

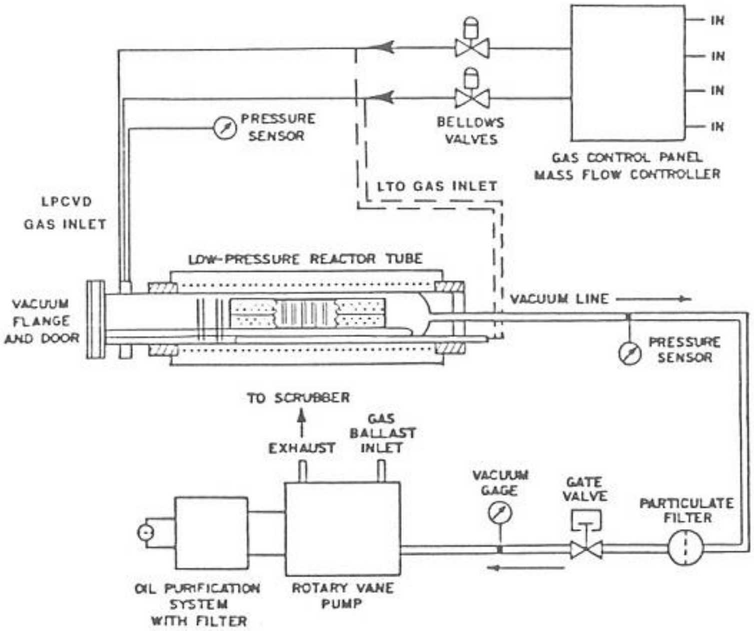

Figure 3.2: Tube-furnace style LPCVD system [61]

In both APCVD and LPCVD processes, the energy required to dissociate and react the precursors is provided by electric heating of the substrate. For production of poly-Si or SiN_x, temperatures required are around 750-900°C [61]. In the later stages of semiconductor processing such as deposition of the final dielectric passivation layers, high temperature process steps are problematic due to the possibilities for melting and diffusion of metal contacts and thermal alteration of precise dopant profiles. The plasma-enhanced chemical vapour deposition (PECVD) process was developed to enable deposition of *a*-Si and Si-based dielectrics at much lower temperatures (100-350°C). In addition to late-stage semiconductor processing, PECVD is also capable of coating temperature-sensitive substrates such as polymers.

The PECVD process occurs at low pressure and temperature within a glow discharge. The energy to promote the growth reaction comes from a combination of heat and externally supplied electric power. PECVD is distinct from sputtering in that the film-forming elements come from gaseous precursors rather than a solid target and in that the growth proceeds by chemical reaction. In the simplest configuration, known as the parallel-plate reactor (Figure 3.3), energy to drive the reaction is provided by an RF power supply applied across two conductive plates with the substrate on one of them. Energy transfer to the glow discharge occurs by capacitive coupling.

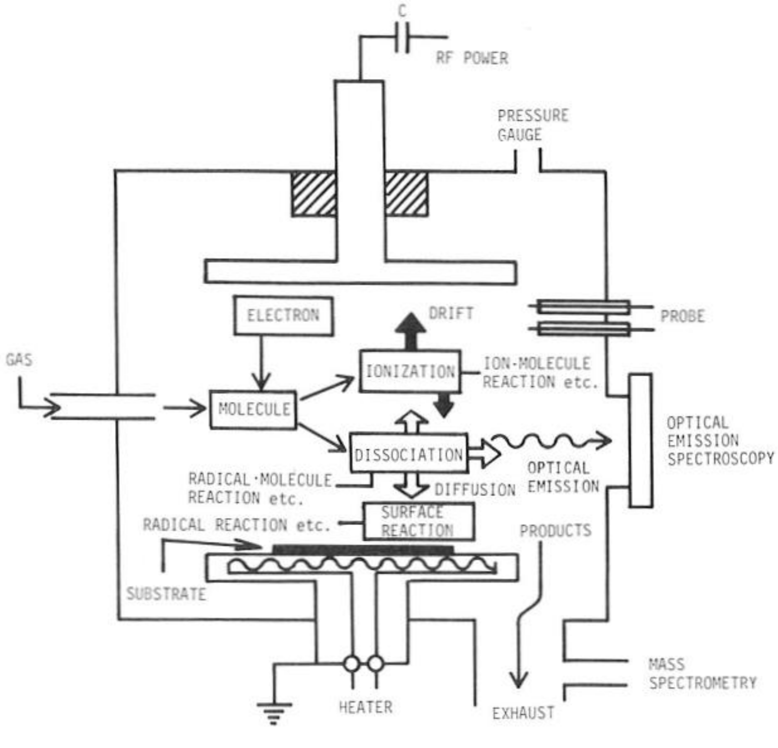

Figure 3.3: Reactions in a parallel-plate PECVD system [62]

In a typical RF-PECVD system, the gas temperature in the plasma region may be only a few hundred Kelvin while the dissociated electrons have an effective temperature as high as 10^4 Kelvin [62]. This disparity occurs because the mass of the electrons is so different compared that of the ions and neutrals, leading to little energy exchange in elastic collisions between the species. The high-temperature electrons, however, have sufficient energy to ionize and dissociate the precursor molecules by inelastic collision. Placing the substrate on the grounded electrode leads to mostly neutral radicals forming the film, while placing it on the powered electrode causes significant ion bombardment of the film as it forms. Depending on the application, either may be desired.

In simple RF-PECVD systems such as that of Figure 3.3, the growing film is always subject to some bombardment from the energetic species in the plasma. This can lead to the generation of electrical defects such as surface states, increased compressive stress, or the accumulation of charge within the film [63]. Furthermore, the efficiency of capacitive coupling to the glow discharge is quite low. This limits achievable plasma density to around $10^{11}/\text{cm}^3$ and thereby limits the efficiency of dissociation of the reaction [62]. Remote PECVD reactors and high-density plasma sources using inductive coupling or electron cyclotron resonance were developed to circumvent these limitations.

3.3.1 Induction Coupled Plasma Enhanced Chemical Vapour Deposition (ICP-CVD)

Using a similar RF power supply as for the parallel-plate reactor, it is also possible to generate plasma in a low-pressure gas by means of inductive coupling. The gas flows through an insulating tube with the RF power applied to a solenoid wrapped around the tube (Figure 3.4). Effectively, the gas becomes the secondary of a transformer with the primary being the solenoid.

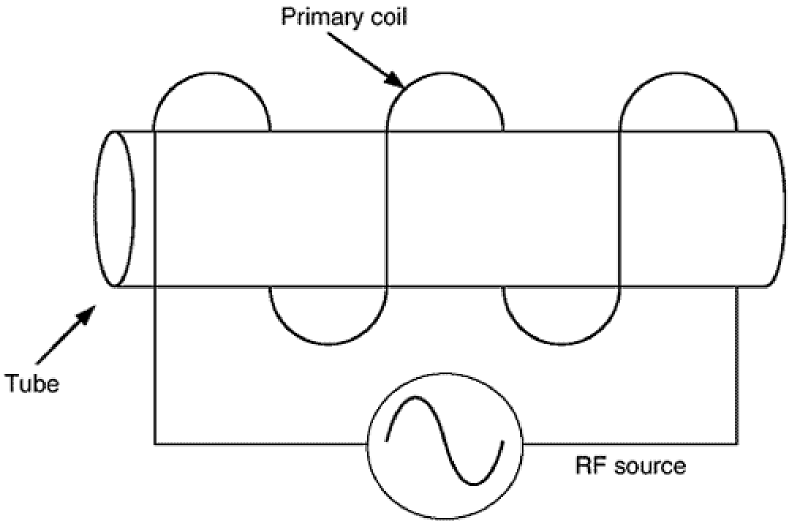

Figure 3.4: Inductively coupled plasma generation [64]

At low applied power, energy coupling to the plasma is in fact primarily capacitive and occurs due to the appearance of high electric potential on the solenoid rather than inductive coupling [64]. This mode of operation is known as the E-discharge and plasmas in this regime are very similar to those produced in parallel-plate reactors. As RF power is increased, inductive coupling begins to dominate and the plasma density increases (H-discharge). The higher density of inductive vs. capacitive coupling enables the placement of the plasma source remote from the reaction chamber (Figure 3.5). The reaction proceeds by means of neutral free radicals produced by plasma decomposition of the source gases. To avoid coating the interior of the ICP source, film-forming gases such as silane (SiH_4) are introduced through a ring or showerhead located inside the chamber.

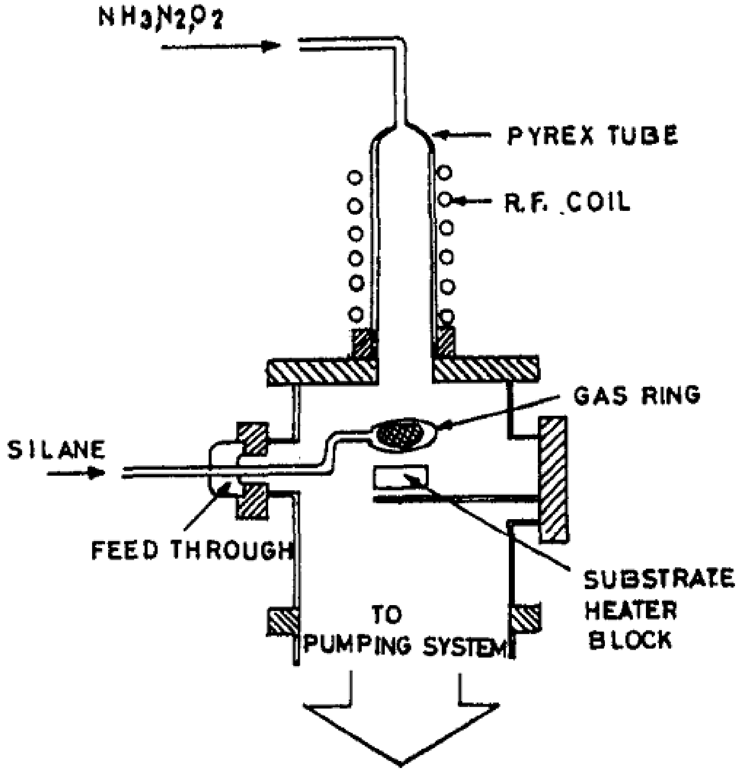

Figure 3.5: Remote ICP-CVD of Si-based films, reprinted from [65]

If ion bombardment of the film is desired, a second RF power supply can be used to apply a negative bias voltage to the substrate. The use of separate plasma and bias power supplies enables independent control of the plasma density (which affects growth rate) and the ion current (which affects film stress and morphology) in a way that wouldn't be possible in a parallel-plate reactor. The efficiency of inductive coupling peaks at lower gas pressure than for capacitive coupling, but the higher efficiency of precursor dissociation counteracts this effect. The McMaster ICP-CVD reactor was used for depositing many of the SiN_x and SiC_x films studied in this work. Figure 3.6 is a schematic of this reactor.

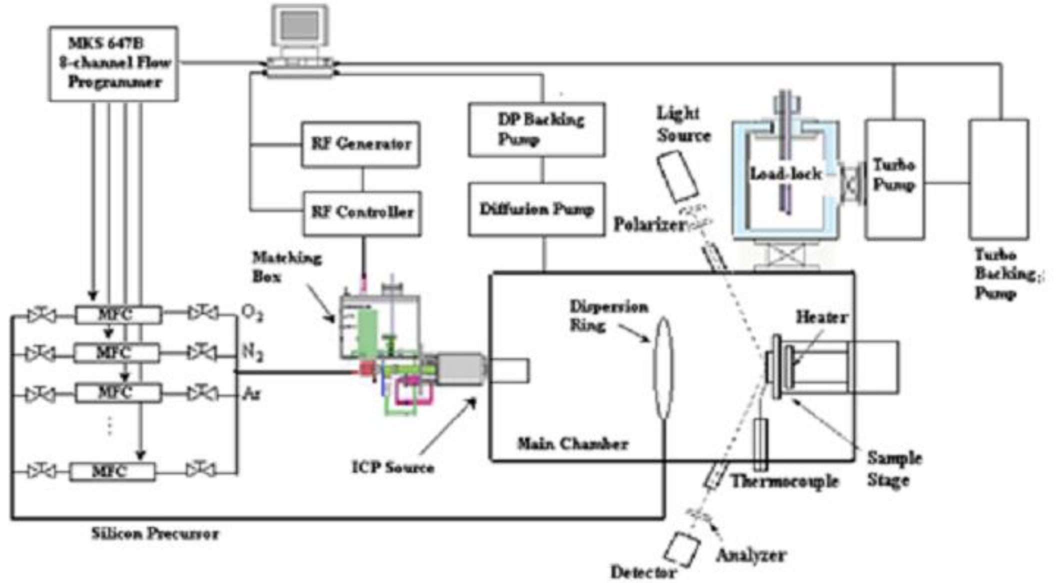

Figure 3.6: Simplified schematic of McMaster ICP-CVD reactor [66]

For a more thorough description of the reactor, refer to [66]. The main components of the reactor are the gas delivery system, ICP source, vacuum system, sample stage, load lock, and control system. The system is capable of producing a variety of silicon-based thin films with variable stoichiometry including *a*-Si, SiO_x, SiN_x, SiC_x, and combinations of the above. Plasma-forming gases such as Ar, O_2, and N_2 are introduced through the ICP torch while SiH_4 and CH_4 are introduced by a dispersion ring. Plasma power is applied to the ICP coil through a reactive matching network by a 1500W-capable 13.56MHz RF power supply. A high-throughput diffusion pump backed by a roots blower and rotary vane pump maintains ultra-high-vacuum base pressure as well as evacuating process gases through a scrubber. The sample stage, which is large enough for a 3” Si wafer or equivalent sized substrate, is rotated at a constant 60rpm by an electric motor during growth and contains a silicon carbide heating element capable of temperatures up to 1200°C. During the initial calibration of the system, it was found [66] that the temperature of the substrate was linearly related to the heating element’s temperature (both in °C) according to

$$T_{substrate} = 0.3303T_{heater} + 21.58 \qquad (3.1)$$

The ICP-CVD is provided with a load-lock to minimize the effects of atmospheric contamination and speed the growth cycle. Transfer of the sample stage between load lock and main chamber is accomplished by a vertical motorized arm and a horizontally movable bellows with a locking system to hold the sample stage. An in-situ Woolam M-44 spectroscopic ellipsometer is available to measure the thickness of the growing films. The system is partially automated with load lock pump-down and pump switchover under automatic control. It is also possible to perform automated multi-step depositions using a recipe mode.

3.3.2 Electron Cyclotron Resonance Plasma Enhanced Chemical Vapour Deposition (ECR-PECVD)

An alternative to inductive coupling for the generation of high-density plasmas is the electron cyclotron resonance (ECR) technique. This system uses perpendicular electric and magnetic fields to accelerate the ionized electrons. A constant axial magnetic field is provided by a large electromagnet coiled around the plasma source, which contains a low-pressure gas. The Lorentz force causes any free electrons within the field to move in circular or helical trajectories (Figure 3.7).

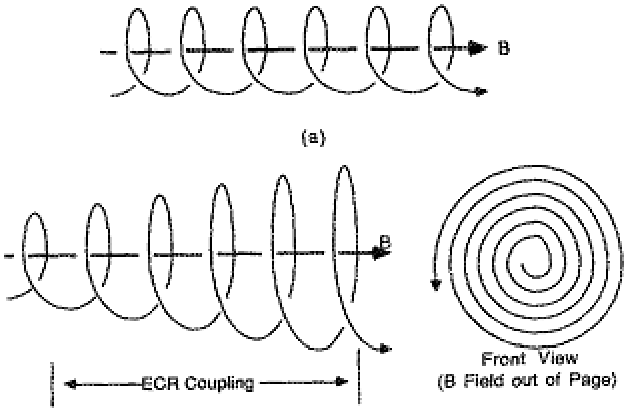

Figure 3.7: Electron trajectories in a static magnetic field, reprinted from [67]

Because the electrons have a constant charge and mass, these orbits will have a frequency which depends solely on the strength of the external magnetic field B [67]. This is known as the electron cyclotron resonance frequency.

$$\omega = \frac{eB}{m_e} \tag{3.2}$$

If an external alternating electric field of this frequency is applied perpendicular to the magnetic field, the electrons will be accelerated by the electric field during each circular orbit. The trajectory of the electron becomes a rapidly widening spiral as it picks up speed and its energy increases. It is therefore possible to produce very efficient energy coupling to the plasma electrons. In practical devices a 2.45GHz microwave power supply is commonly used, which will meet the resonance condition at an external magnetic field of 875 Gauss [67]. Figure 3.8 is a schematic of an ECR plasma source similar to that used in the Group IV-McMaster ECR-PECVD system.

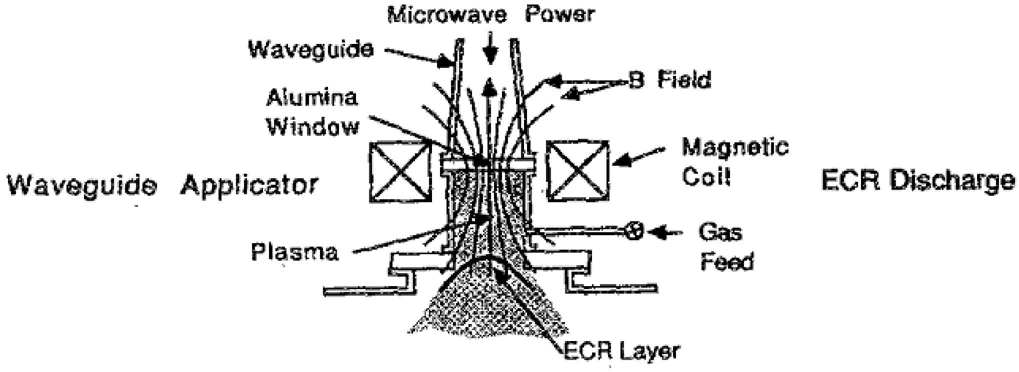

Figure 3.8: Simplified diagram of ECR plasma source, reprinted from [67]

The microwave power is supplied to the gas through a rectangular metal waveguide while the magnetic field is supplied by a large electromagnet coiled around the source tube. An alumina or sapphire window separates the vacuum conditions inside the plasma source from the atmosphere in the waveguide. As with ICP sources, the ECR source can be located remote from the growth chamber allowing free radicals to pass through while minimizing ion bombardment. In the case of the Group IV-McMaster ECR-PECVD system, plasma gases (Ar, N_2, O_2) are introduced through dispersion holes in a double-layer sapphire window while film-forming gases (SiH_4, CH_4) are introduced through a separate dispersion ring in the chamber. A block diagram of the system is given in Figure 3.9.

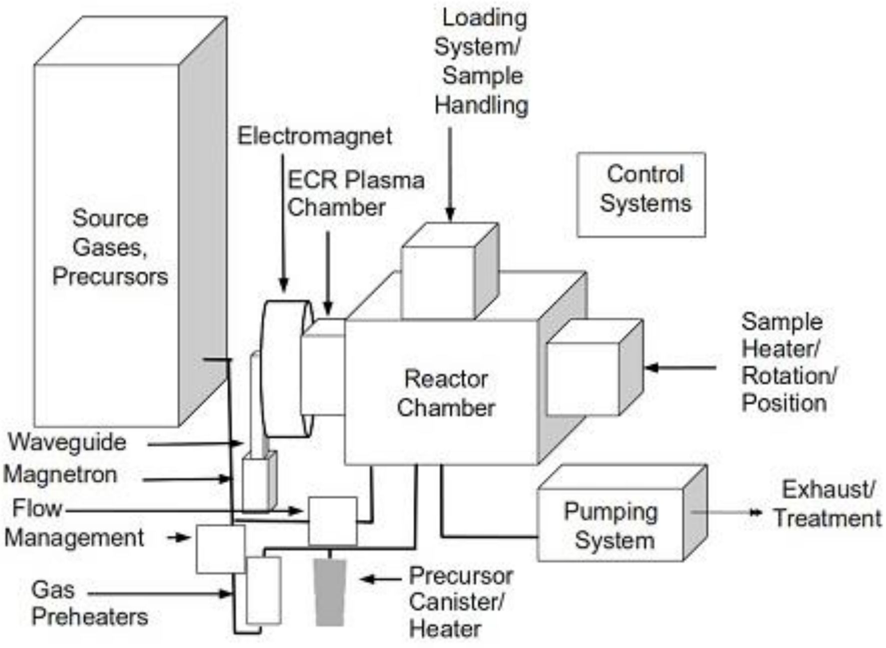

Figure 3.9: Diagram of Group IV-McMaster ECR-PECVD reactor [12]

A more thorough description of the Group IV-McMaster ECR-PECVD system can be found in [12]. The design of this ECR-PECVD system was heavily influenced by that of the earlier ICP-CVD system. The systems feed from a common gas cabinet and thus are capable of depositing the same set of materials (*a*-Si, SiO_x, SiN_x, SiC_x). Microwave power for the ECR source is supplied by a 1500W-capable Astex 2.45GHz power supply while the electromagnet runs at a constant current of 180A. Ultra-high base vacuum pressure is maintained by a high-throughput turbomolecular pump backed by a Roots blower and rotary vane pump. Load lock, sample stage, sample transfer system, and control software are almost identical to those of the ICP system described in section 3.3.1.

A significant difference between the systems is that the Group IV-McMaster ECR-PECVD incorporates metalorganic precursors for producing rare-earth and aluminium-doped films. The precursors, which are solid powders, are stored in insulated heating jackets connected to the system by valved ¼” stainless steel piping. The temperature of the cells is controlled by Eurotherm temperature controllers on their electric heaters. An additional controller maintains the temperature of the connecting piping. The piping is insulated with fiberglass filler and aluminium foil to maintain its temperature. It is critical to maintain the pipes at a higher temperature than the precursor source cell to avoid solidification of the precursor within the piping. Vapour from the precursor is carried along the pipes to the reaction chamber by a flow of argon carrier gas.

The precursors themselves are metalorganic complexes from a chemical family known as the metal β-diketonates. The particular chemical used for producing Al-doped films is known as aluminium tris (2,2,6,6-tetramethyl-3,5-heptanedionate) or $Al(TMHD)_3$, and consists of a single Al atom weakly bonded to three large organic TMHD complexes (Figure 3.10).

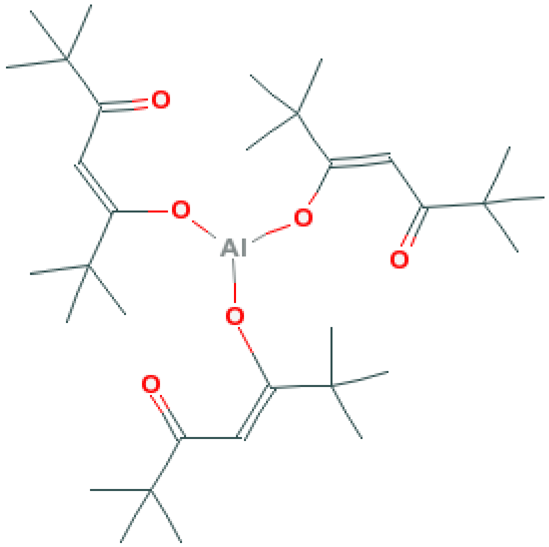

Figure 3.10: Chemical structure of Al(TMHD)$_3$ precursor [68]

The design of metalorganic precursors for CVD is a complex subject in its own right and will not be discussed in detail here. In general, however, the precursors are designed to be stably solid at room temperature with increasingly high vapour pressure at 100-250°C. Other concerns in precursor design are to ensure that the bonds between the metal atom and the organic ligands are the weakest in the structure and that the ligands themselves are fairly unreactive once separated from the metal.

3.4 Annealing Treatments

Post-deposition thermal treatment of plasma-deposited thin films can be used for a variety of purposes including densification, hydrogen removal, dopant activation, and adjustment of stress states. In non-stoichiometric films, it is also known to promote nucleation and growth of Si nanocrystals or nanoclusters and thereby enhance photoluminescence. In general, to avoid oxidizing the film, it is necessary to perform this annealing under an inert atmosphere such as argon (Ar) or nitrogen (N_2). High-purity N_2 for annealing is delivered from a pressurized N_2 gas cylinder. Temperatures used range from 400-1200°C, with a typical treatment time being 60min.

A common apparatus for thermal treatment in research environments is the quartz tube furnace. In the tube furnace, controlled atmosphere is produced by flowing gas in a continuous sheet along the tube exiting at one end via an oil trap. Temperature is monitored by thermocouples and controlled by electric heaters. The upper temperature limit of 1200°C is enforced by the potential for damage to the quartz tube, while at temperatures below 400°C little effect on the film properties can be expected. Due to the imprecise nature of the measurement of high temperatures, when performing annealing in different tube furnaces it is generally necessary to check temperature with a calibration thermocouple to ensure consistency between results. Typical absolute accuracy of temperature measurements in the range used for annealing is around ±40°C.

4 Characterization Techniques

4.1 Variable Angle Spectroscopic Ellipsometry

Ellipsometry is an optical measurement technique that relies on the change in polarization of light as it interacts with a material. A beam of linearly polarized light containing both *p* and *s*-polarized components is reflected off the sample being measured (Figure 4.1).

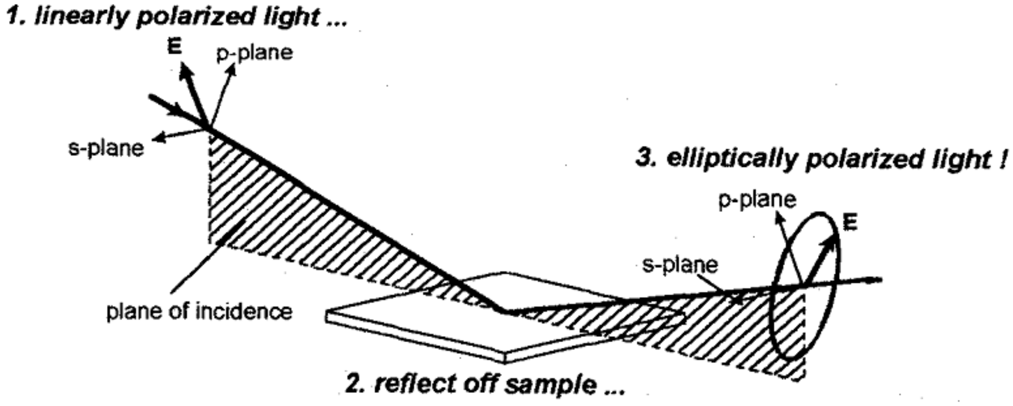

Figure 4.1: Conceptual diagram of ellipsometric measurement [69]

The reflectance of the sample for the *s*- and *p*-polarized components is based on the index difference between the ambient (n_a) and the sample (n_s) and is described by the Fresnel equations. In general, lower index contrast between ambient and sample reduces the reflectance of the interface and leads to less available signal. The difference in interface reflectance for *s*- and *p*-polarized light modifies the amplitude ratio for the *s*- and *p*-components of the electric field in the reflected beam, and also introduces a phase shift between them. In other words, the reflected beam's polarization is now elliptical.

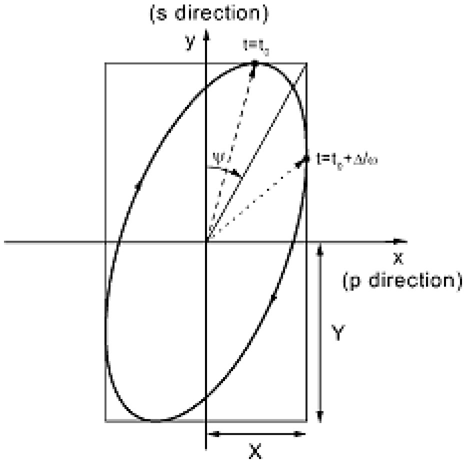

Figure 4.2: Elliptically polarized light propagating toward the reader [70]

The polarization state of the elliptically polarized beam can be expressed in terms of the amplitude ratio ψ and the phase shift Δ (Figure 4.2). For the case of a linearly polarized beam reflected from an interface, ψ and Δ for the resulting beam are dependent on the ratio of complex reflectances (ρ).

$$\frac{r_p}{r_s} = \rho = \tan\psi\, e^{i\Delta} \tag{4.1}$$

The key optical elements of an ellipsometer are the *polarizer* which generates linearly polarized light from the incoherent source and the *analyzer* that measures the polarization of the reflected beam. Many ellipsometers include a *compensator* plate as well, which converts linearly polarized light into circularly polarized light. A common location for the compensator is between the polarizer and the sample, creating the popular PCSA configuration (Figure 4.3).

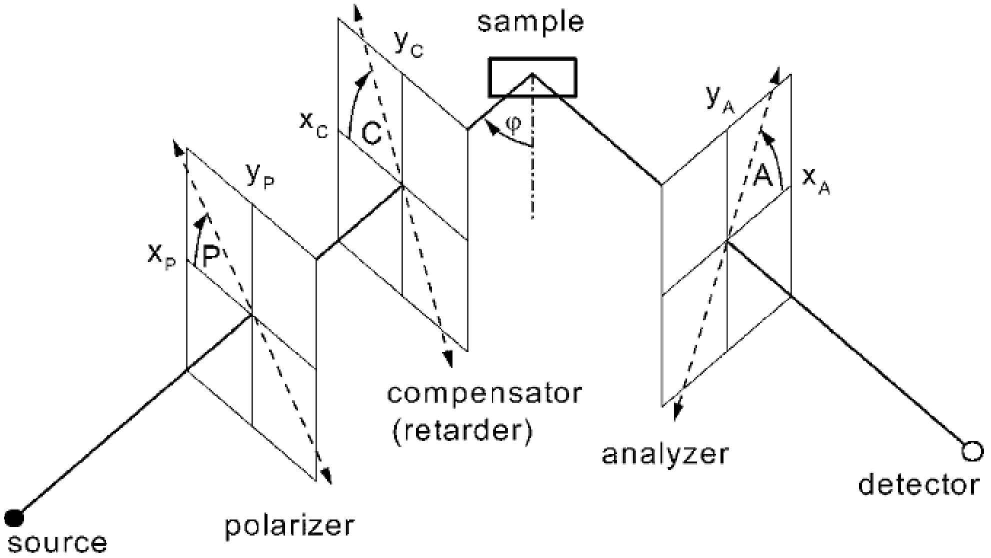

Figure 4.3: Configuration of optical elements in a PCSA ellipsometer [70]

In classical null ellipsometry, the polarizer azimuth *P* and compensator azimuth *C* are adjusted so as to produce elliptically polarized light that is converted to linearly polarized light by the action of the sample-ambient interface. The analyzer azimuth *A* is then adjusted until the light intensity at the detector is zero, indicating that the analyzer's axis is orthogonal to the polarization of the beam returning from the sample. For a quarter-wave compensator set at azimuth $C=\pi/4$, the ellipsometric angles can be simply extracted from the polarizer and analyzer azimuths [70].

$$\psi = A, \Delta = 2P + \frac{\pi}{2} \tag{4.2}$$

The nulling technique, though accurate, is rarely used in automated ellipsometers due to the long acquisition time and requirement for manual adjustment of the optical elements. An alternative is to rotate one of the optical elements while measuring the received light intensity as it varies with the angle. This configuration is known as the rotating polarizer, analyzer, or compensator ellipsometer depending on the element being rotated. Another possibility is to employ a photoelastic modulator to control the polarization of the incident beam, enabling a rapid scan of polarizations. More detailed descriptions of each topology can be found in [70].

If a smooth, homogeneous sample with no surface oxide or roughness is assumed, and the angle of incidence ϕ is known, it is possible to directly determine the complex refractive index or dielectric function of the sample [69]

$$\varepsilon_1 + i\varepsilon_2 = (n + ik)^2 = \sin\phi^2 \cdot \left[1 + \tan\psi^2 \cdot \left(\frac{1-\rho}{1+\rho}\right)^2\right] \qquad (4.3)$$

Of course, these assumptions are rarely satisfied in practice and this simple equation doesn't allow for the determination of the thickness of a film on a substrate. Thickness determination for a thin film is only possible if the film is thin and transparent enough for some of intensity of the beam to survive passage through the film, reflection from the film-substrate interface, and passage back through the film (Figure 4.4). The ψ and Δ values measured in this case contain information about the complex reflectance of both the film-ambient and film-substrate interface. For a thin film with a thickness t and complex refractive index $n+ik$, it is possible to determine only two of the three quantities. For transparent films such as SiO_2, the assumption $k=0$ is commonly used.

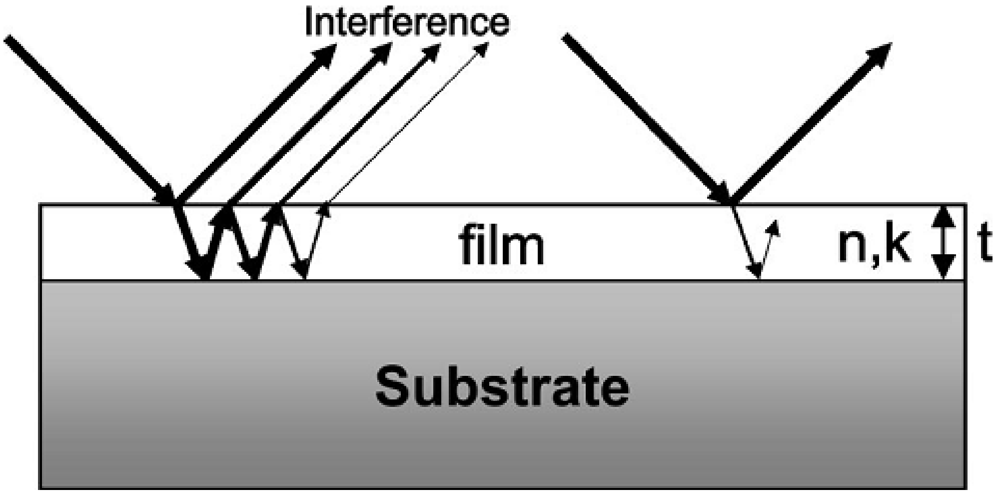

Figure 4.4: Transparent (left) and absorbing (right) films, repinted from [71]

The limitations of single-wavelength ellipsometric measurements are overcome by the variable angle spectroscopic ellipsometry (VASE) technique, in which ψ and Δ are measured at multiple angles and sometimes as many as hundreds of wavelengths. The greater amount of available parameters enables the characterization of complex multi-layer structures and improves precision in determining the thickness of single layers. The visible and near-infrared wavelengths are commonly used for spectroscopic ellipsometry because they are easy to generate and detect, and for optical materials provide information about the behaviour of the material over the spectral range in which it will be used. In order to make use of the data from the VASE measurement, it is necessary to have some knowledge of how the complex refractive index of a material varies with wavelength.

The Cauchy dispersion equation is an empirically-derived expression for the variation of refractive index of a transparent material with wavelength. Most transparent materials (air, glass, etc.) can be said to exhibit *normal dispersion*, whereby the refractive index increases with decreasing wavelength. Of course, this is true only over a limited energy range below the energy necessary to cause interband absorption transitions. For dielectric materials such as SiO_2, Al_2O_3, and stoichiometric Si_3N_4, the Cauchy dispersion relation has been found to be effective over the visible and near-IR spectral range [72].

$$n(\lambda) = A + \frac{B}{\lambda^2} + \frac{C}{\lambda^4} \tag{4.4}$$

$$k(\lambda) = 0 \tag{4.5}$$

Often, the value of the C parameter is extremely small and the A and B parameters are sufficient to describe the film's dispersion over some wavelength range. The Cauchy dispersion relation is only useful for the case where absorption in the film is small enough so as to be negligible. For materials like amorphous Si and SiC, where the optical bandgap falls within the visible region, a more sophisticated model is mandated. The Tauc-Lorentz oscillator model calculates the imaginary part of the material's dielectric function, ε_2, by multiplying the Tauc formulation for the density of states above the bandgap with the ε_2 predicted by the classic Lorentz oscillator model of interband transitions [73]. Below the bandgap, the assumption ε_2=0 is employed. The value of ε_1 is obtained by Kramers-Kronig integration of ε_2.

$$\varepsilon_1 = \varepsilon_\infty + \frac{2}{\pi} P \int_{E_g}^{\infty} \frac{\xi \varepsilon_2(\xi)}{\xi^2 - E^2} d\xi \tag{4.6}$$

$$\varepsilon_2 = \frac{AE_0\Gamma\left(\mathrm{E}-\mathrm{E_g}\right)^2}{(E^2-E_0^2)^2+\Gamma^2E^2}\frac{1}{E}, E > E_g \tag{4.7}$$

$$\varepsilon_2 = 0, E \leq E_g \tag{4.8}$$

Where A is the amplitude of the Lorentz oscillator, E_0 is its center energy of the oscillator, Γ is a term representing the broadening of the oscillator, E_g is the bandgap or transition energy at which the onset of absorption occurs, and ε_∞ is a constant representing the effects of optical transitions at higher energy. Thus, the Tauc-Lorentz formulation for the dielectric functions of absorbing materials has five parameters that can be adjusted to fit a particular set of data.

Once a model structure has been decided upon for the characterization of the film, it is necessary to vary the model parameters to fit the model to the data measured in the ellipsometry experiment. The experimenter is responsible for selecting the correct model for the film-substrate system and checking the results to ensure that they are reasonable. Typically, an algorithm such as the Marquardt-Levenberg is used to determine values for the fit parameters that produce the best possible agreement between the measured ψ and Δ spectra and the optical model. For n measured wavelengths and m fit parameters in the model, the MSE can be calculated by summing the χ^2 estimators for ψ and Δ at over all possible wavelengths.

$$MSE = \sqrt{\frac{1}{2n-m}\sum_{i=1}^{n}\left(\frac{\psi_i^{mod}-\psi_i^{exp}}{\sigma_{\psi,i}^{exp}}\right)^2+\left(\frac{\Delta_i^{mod}-\Delta_i^{exp}}{\Delta_{\psi,i}^{exp}}\right)^2} \tag{4.9}$$

As long as the film surface is optically smooth (roughness is small in comparison with the wavelength of light in use), the surface roughness layer can be modelled using a Bruggeman effective medium approximation layer incorporating 50% film and 50% void. The model used may also need to account for the presence of native oxide on the Si wafer prior to film deposition.

The J.A. Woolam M-2000 VASE ellipsometer used for characterizing thin films in this study is of the rotating compensator type and uses a CCD sensor to collect data at multiple wavelengths simultaneously. It is capable of measuring ellipsometric parameters over a broad spectral range from 245-1690 nm, sampling at 676 different wavelengths. The typical measurement programme consists of 5-second measurements at 5 different angles (55°, 60°, 65°, 70°, 75°). The M-2000 comes with the CompleteEASE data analysis software, which includes the Cauchy and Tauc-Lorentz dispersion models as well as many others. It also includes reference optical constants for a variety of common materials including Si wafers.

4.2 Ion Beam Analysis

Ion beam analysis involves the interaction of a high-energy beam of ions with the sample and collection of the resulting signals. High energy ions impacting a solid may be elastically backscattered (RBS), recoil atoms from the target (ERD), generate X-rays (PIXE), or undergo nuclear reactions (NRA). Methods of ion beam analysis used in this study include Rutherford backscattering spectrometry (RBS) and elastic recoil detection (ERD).

4.2.1 Rutherford Backscattering Spectrometry

In RBS, the sample being analyzed is bombarded with a beam of He ions (or α particles) with energies typically in the range of 0.5-2MeV. Within this energy range, the interaction between the incident ion and the target atom is dominated by Coulomb forces and can be modelled as an elastic collision in which energy is conserved. The energy of the ion after the collision (E_1) is related to its initial energy (E_0) by the kinematic factor k [74], which is dependent on the atomic mass of the incident ion (M_1) and target ion (M_2) as well as the scattering angle (θ).

$$E_1 = kE_0, k = \frac{M_1 \cdot (\cos\theta \pm \sqrt{\left(\frac{M_2}{M_1}\right)^2 - \sin^2\theta}}{M_1 + M_2} \tag{4.10}$$

The low mass of the He ions relative to the target means that they will tend to scatter backwards off the target similar to the concept of throwing a ping-pong ball at a bowling ball. The backscattered ions are collected by a detector located at an angle β from the sample surface. Two of the most common geometries for RBS experiments are shown in Figure 4.5.

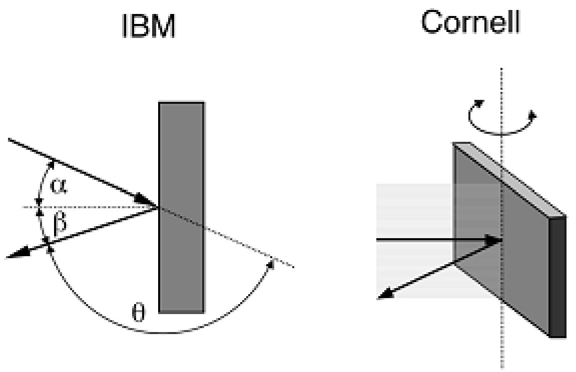

Figure 4.5: IBM and Cornell geometries for an RBS experiment [74]

The detector is sensitive to the energy of the backscattered ions, making it possible to distinguish between elements of different atomic mass within the sample. In order to establish the concentration of each element, however, it is also necessary to know the probability of such an event occurring. As long as the collision between the He ion and the target atom is elastic, this depends only on the atomic numbers of the incident (Z_1) and target (Z_2) atoms, the incident energy (E_0), and the scattering angle (θ) and is predicted by the Rutherford formula [75]:

$$\frac{d\sigma}{d\Omega}\alpha\frac{Z_1Z_2}{E_0^2}\frac{1}{\sin^4(\theta/2)} \tag{4.11}$$

It is therefore possible to determine both the sample composition and concentration based on the backscattered ion signal. As the ions pass through the solid sample, they lose energy due to inelastic collisions with the electrons at a rate given by the material's differential stopping power. This results in a spreading of the energy peak observed for each element and enables distinguishing between elements at different depth in the sample (Figure 4.6).

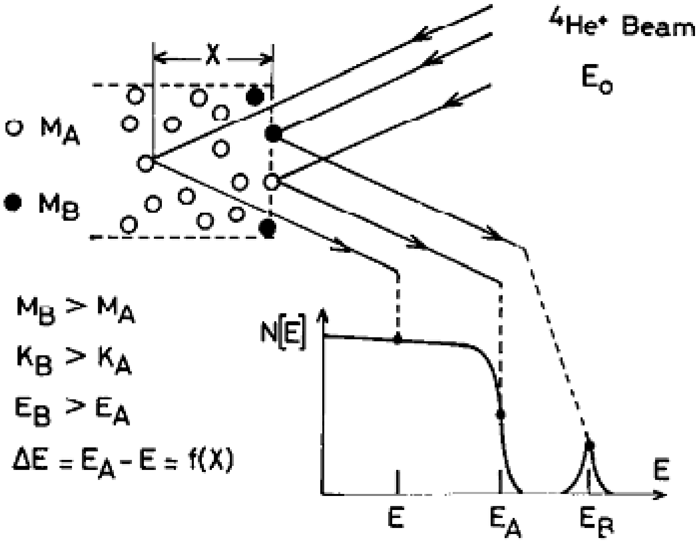

Figure 4.6: Energy spectrum collected in an RBS experiment [75]

It is important to note that the stopping power is a strong function of the ion energy, and is only known to within about 5% for most elements [74]. This is one of the limiting factors in the determination of film composition by RBS. The presence of a film of mixed composition (such as SiO_x or SiN_x) on a pure substrate is easily visible in the RBS spectrum. For the case where an element (such as Si) appears in both the film and the substrate, Si in the film will appear as a low-amplitude "shoulder" on the broader substrate signal (Figure 4.7).

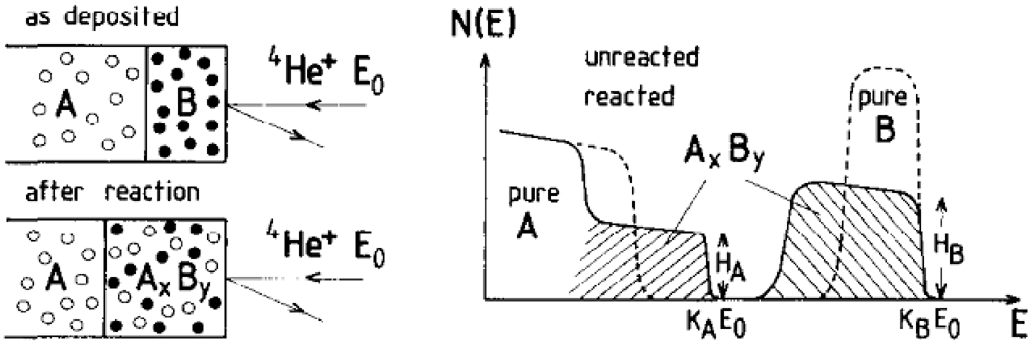

Figure 4.7: RBS spectra of pure and mixed thin films, reprinted from [75]

For the case of an amorphous film on a crystalline substrate, it is possible to align the ion beam to minimize the signal from the substrate. This can be envisioned as the parallel ion beam “tunneling” or “channeling” between the nuclei along crystal plane of the material. This practice allows a clearer resolution of the elemental peaks in the amorphous film (Figure 4.8)

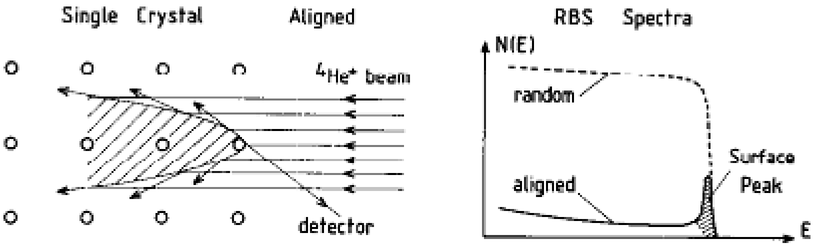

Figure 4.8: Effect of ion channeling on RBS spectra, reprinted from [75]

RBS studies performed in this work were undertaken at the Tandetron accelerator facility at Western University, London, Ontraio, a 1.7MV linear tandem ion accelerator. The Tandetron uses the Cornell geometry due to its advantages of large scattering angle and grazing incident angle [74]. Data analysis was performed using the SIMNRA software, of which further details can be found in [76].

4.2.2 Elastic Recoil Detection

Elastic recoil detection also relies upon elastic collisions between an incident ion beam and the atoms of the target, but in ERD a beam of ions heavier than the target's atoms is used. This results in *forward* scattering, or recoiling, of the target atoms (Figure 4.9) and enables the detection of all elements lighter than the beam ions. For Si-based films on Si substrates, a 35 MeV Cl beam is a common choice. Unlike RBS, ERD is sensitive to H content in the films.

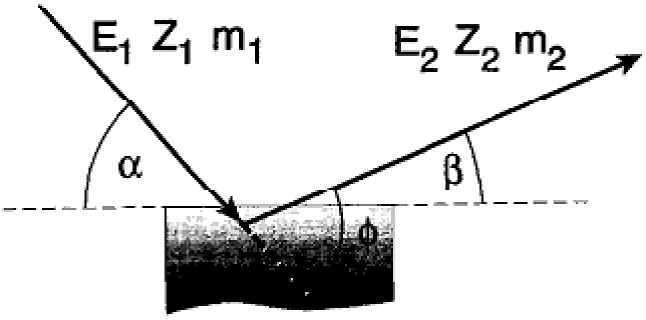

Figure 4.9: Basic geometry of an ERD experiment, reprinted from [77]

A common detector used for ERD measures both the energy of recoiled ions and their time-of-flight. Knowing both the energy and speed of the ion enables determination of its mass, and the resulting spectrum is a 2-dimensional matrix containing information both about the composition of the sample and the variation of the composition with depth. ERD is generally able to resolve compositional information that in RBS might be masked by overlapping peaks.

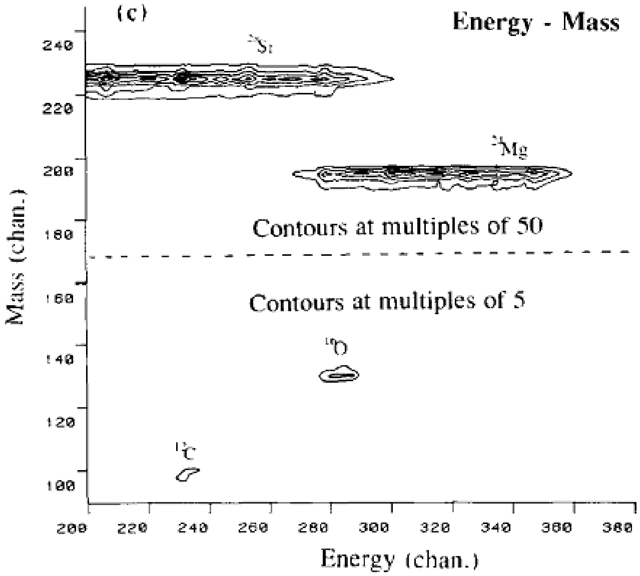

Figure 4.10: ERD spectrum for an Mg film on Si, reprinted from [78]

ERD studies in this work were performed at the Ion Beam Laboratory at the Université de Montreal, using a 35 MeV Cl beam and a time-of-flight detector (TOF-ERD system).

4.3 Energy-Dispersive X-ray Spectroscopy

Energy-dispersive X-ray spectroscopy (EDX), makes use of a scanning electron microscope (SEM) to obtain information about the elemental composition of a sample. Electrons in an SEM are accelerated to an energy of typically 5-25keV, which making them capable of removing electrons from the *M*- or *L*-shells of any element or from the *K*-shell of light elements like Si. These electrons are the signal used by the SEM to form an image (beam electrons may also scatter backwards off the target). If an inner shell electron is removed, an outer shell electron will drop down to replace it, producing energy that may be released as an X-ray or give rise to an Auger electron. Because the generated X-rays interact only weakly with matter, they can originate from a much greater depth within the sample than other signals produced in an SEM (Figure 4.11).

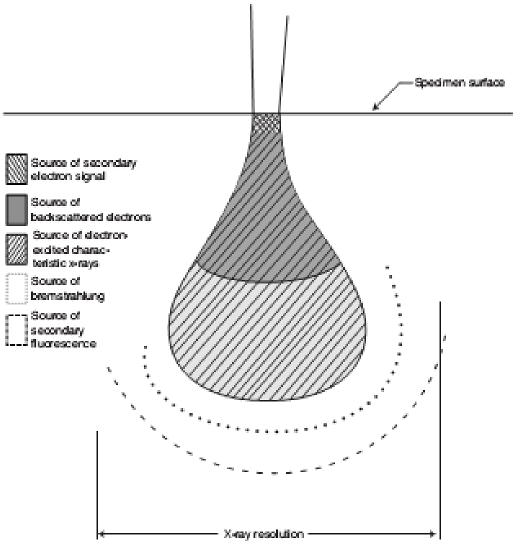

Figure 4.11: Source of signals produced in SEM [79]

X-rays may also originate from the *bremsstrahlung* process which occurs as the high-energy electrons have their trajectories bent and slowed by the attractive effect of the target's nuclei. This produces a continuous background spectrum of X-rays from the target in addition to the characteristic rays produced from electron transitions [80]. The characteristic X-rays are named for the atomic shell transition that produced them (Figure 4.12).

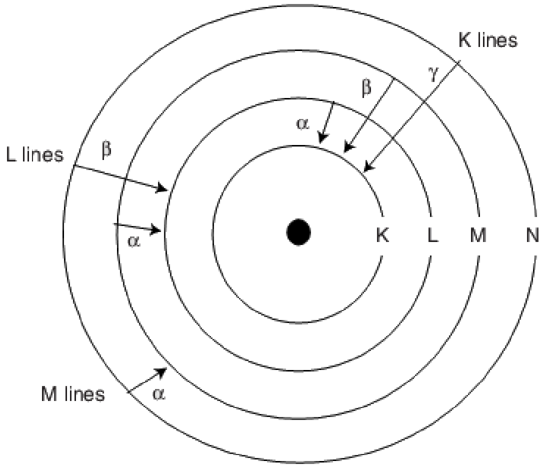

Figure 4.12: Characteristic X-ray nomenclature [79]

For any given element, the K-rays will have the highest energy since they originate from transitions with the greatest energy level difference. The energy of characteristic X-rays produced is also dependent on the atomic number of the emitting element. Heaver elements produce X-rays of higher energy because the higher number of protons within the nucleus creates a deeper potential well for any given shell (Figure 4.13).

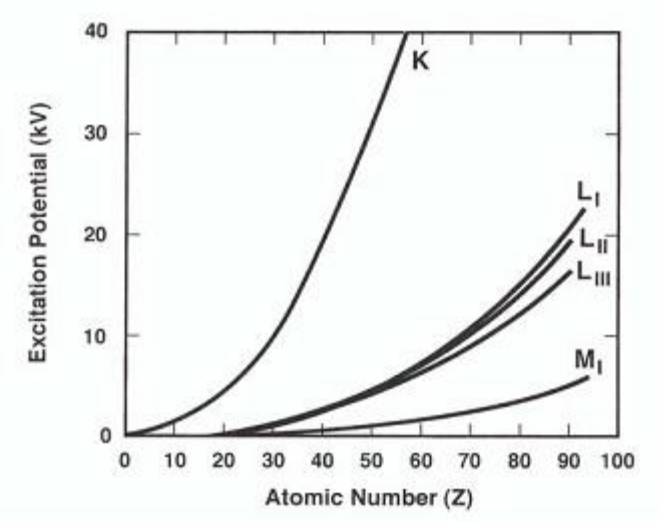

Figure 4.13: Energy of characteristic X-rays by atomic number [81]

The energy of a characteristic X-ray for a given shell transition (K, L, M) has a quadratic dependence on the atomic number of the emitting element. This relationship is known as Moseley's law [79] and forms the basis of EDX analysis.

$$E = c_1(Z - c_2)^2 \tag{4.12}$$

The efficiency of production for X-rays of a given energy E_c is dependent on the energy of the incoming electron. In general, the X-ray intensity for electron energy E_0 and beam current i_b approximately follows the empirical relationship [80]

$$I = Ci_b(E_0 - E_c)^{1.7} \tag{4.13}$$

It follows that X-ray intensity is maximized for electron energies of 2-3 times the desired X-ray energy, and falls off only slowly with increasing electron energy. A commonly used technique for EDX is to select an accelerating voltage of twice the highest expected X-ray energy from the sample. For lighter elements, competitive processes such as Auger electron emission are more efficient than X-ray production (Figure 4.14). This limits the applicability of EDX for light elements by reducing the amount of signal detected.

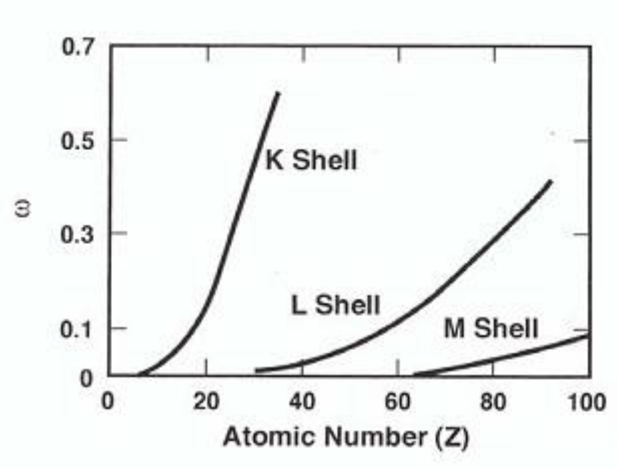

Figure 4.14: Efficiency of X-ray production by atomic number [81]

The combination of the characteristic and bremsstrahlung X-rays produces an X-ray spectrum consisting of a continuous background with sharply resolved peaks corresponding to the elements in the sample (Figure 4.15). Modern EDX detectors have sufficient spectral resolution to easily resolve K-lines even from elements adjacent in the periodic table. However, overlaps may occur for instance where a K- or L-line from a lighter element is at a similar energy to a L- or M-line from a heavier element.

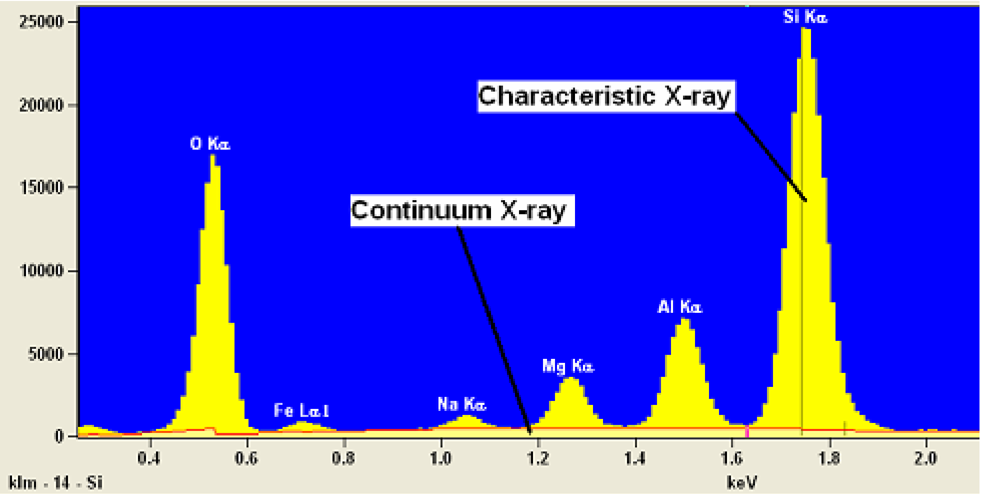

Figure 4.15: EDX spectrum of a sample containing Na, Mg, Al, Si, and Fe [81]

In principle, it should be possible to quantify the elemental concentration within the sample by simply integrating over each characteristic X-ray peak and comparing the total counts to the counts from a reference standard of the pure element. In practice, a collection of effects known as *ZAF* (atomic number, absorption, and fluorescence) makes this impossible and necessitates an iterative technique [80]. An initial concentration is estimated based on the observed intensities and used to calculate ZAF corrections. The corrections thus calculated are used in a re-calculation of the atomic concentrations. The process is repeated until further iterations show little change. The accuracy of this process is improved by the use of a reference standard with composition similar to that of the sample, since it will have similar ZAF effects.

The sensitivity of EDX to light elements is ultimately limited by the presence of a Be window on the detector. The Be window protects the detector from the inferior vacuum conditions inside the SEM. Because the efficiency of

EDX for light elements is low anyway, this is not usually significant. Contamination of the sample surface or the detector window surface can affect the accuracy of quantitative calculations.

For thin-film samples of several microns thickness or less, it is generally necessary to perform a calculation or simulation of the electron trajectories to ensure that characteristic X-ray production is occurring within the *film* and not the substrate. A commonly used Monte Carlo simulation program for this purpose is the CASINO electron simulator [82], developed at the University of Sherbrooke. CASINO simulates electron trajectories and X-ray production in a solid sample given input concerning the beam energy, detector angles, and sample composition.

EDX studies in this work were performed at McMaster University's Canadian Centre for Electron Microscopy using the JEOL JSM-6610LV SEM. This instrument comes equipped with a large-area EDX detector from Oxford Instruments and the accompanying spectrum analysis software, INCA Energy. In addition to performing spectral analysis and ZAF corrections, INCA Energy includes options for compositional mapping and allows for standardization on measured samples. A commonly used standard for EDX analysis of Si-based PECVD films is thermal SiO_2, since it has a well-defined composition.

4.4 Nanoindentation

The use of indentation techniques to measure the hardness of a material has a long history. Classic hardness tests such as the Vickers and Brinell tests measure the resistance of a material to plastic deformation by pressing a rigid indenter (such as a diamond) at a fixed load into the surface and visually inspecting the size of the resulting impression. The hardness of a material is not a fundamental physical property but an arbitrary value that is nevertheless indicative of its resistance to plastic deformation. In general, hardness refers to the ratio of applied force F to the surface area A of the resulting impression left by the indenter for some fixed geometry (such as a spherical or square pyramidal diamond).

$$H = \frac{F}{A} \tag{4.14}$$

Although hardness can be expressed in units of pressure such as GPa, it is not a pressure and is distinct from the contact pressure because it uses surface area and not projected area. The applied force used determines the 'scale' of the test and the size of the resulting impression. For indentation of μm-range thickness layers such as hard tribological coatings, the impression can be mere tens to hundreds of nm in size. This makes it very difficult to accurately measure with optical or even electron microscopy. As a result, a technique was developed [10] to make use of force- and depth-sensing indentation instruments to extract material properties from the load-displacement curve directly.

The most common indenter geometry for nanoindentation is the Berkovich tip, a three-sided pyramid of diamond with a face half-angle of 65.27°. The pyramid has three sides rather than four because this makes it much easier to grind to a single point. A new Berkovich indenter may have a tip radius as small as 50nm [83]. As the indenter is pressed into the surface of the sample and then retracted the applied load and penetration depth are continuously measured, producing a curve with a distinctive shape (Figure 4.16).

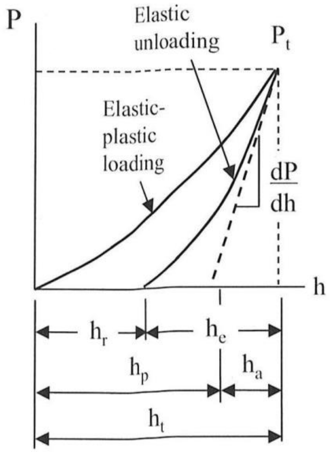

Figure 4.16: Load-displacement curve of a nanoindentation experiment [84]

It was empirically determined [10] that the shape of the unloading curve with depth could be accurately modelled using a power-law fit with two fit constants α and m.

$$P = \alpha(h - h_r)^m \tag{4.15}$$

The four critical quantities measured during the indentation experiment are the maximum load P_t, the maximum depth h_t, the unloading stiffness $S=dP/dh$ (measured during the initial steep part of the unloading curve), and the residual depth h_r of the indentation. Deformation induced during the test is plastic in the region under the indenter and elastic in the surrounding area, causing a "sink-in" of the tip during the test (Figure 4.17). Afterwards, elastic recovery occurs; measuring the slope at this point enables extraction of the material's modulus. The plastic deformation results in a permanent impression of depth h_f.

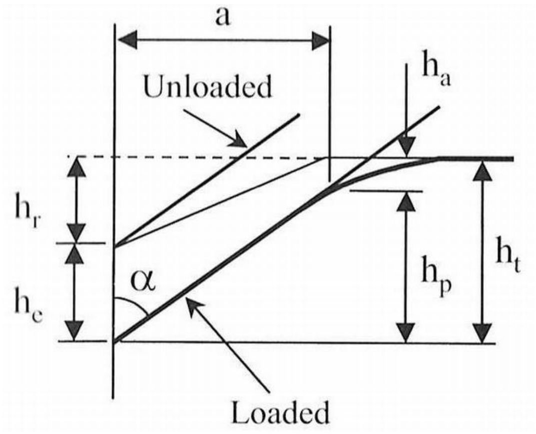

Figure 4.17: Geometry of a nanoindentation experiment [84]

Elastic models show that the sink-in depth h_a can be determined based on only the applied load, the measured contact stiffness, and a geometrical constant which typically approximated as ε=0.75 for a Berkovich indenter [85]. It is thus possible to determine the true depth of the contact at maximum load (h_p).

$$h_p = h_t - \varepsilon \frac{P_t}{S} \tag{4.16}$$

Once the contact depth is known, it is possible to determine the surface area of the indentation for a given depth based solely on the geometry of the indenter. The relationship of surface area to depth for the indenter is known as the area function *F(h)*.

$$A = F(h_p) \tag{4.17}$$

The indentation hardness of the material can now be very simply determined using $H=P_t/A$. Furthermore, the elastic modulus E_r can be extracted from the contact stiffness.

$$S = \beta \frac{2}{\sqrt{\pi}} E_r \sqrt{A} \tag{4.18}$$

The measured modulus E_r is known as the reduced modulus and is dependent on the elastic moduli of the both the specimen (E) and indenter (E_i). If the specimen's Poisson's ratio is known, it is possible to extract the true modulus of the specimen alone.

$$\frac{1}{E_r} = \frac{1-\nu^2}{E} + \frac{1-\nu_i^2}{E_i} \tag{4.19}$$

For the case of a thin film on a substrate the situation is more complicated because some of the deformation induced by the indenter occurs within the substrate, leading to measured hardness and modulus being composite values of the film-substrate system. As the ratio of the indentation depth h to the film thickness d increases, the observed hardness and modulus trend smoothly from the true values for the film toward the values of the substrate.

The most common strategy for extracting the film-only modulus is to perform indentations at several depths on a substrate with known modulus and extrapolate a fit through the data to zero depth. A wide variety of fitting functions have been used [42], [83], [86], [87] with the simplest, a linear function, only being valid for $h/d<0.15$. A similar technique can be used for hardness or the

"10% rule" can be applied, which notes that in most cases plastic deformation will occur entirely within the film for $h/d<0.1$ [83].

Nanoindentation studies in this work were performed using the Hysitron TriboIndenter at École Polytechnique de Montréal. This instrument offers automatic power-law fitting of load-displacement curves, is capable of loads as small as 10μN, and has a precision of ±1nN and ±0.04nm for load and displacement measurements, respectively.

4.5 Scratch Testing

A variety of methods exist for determining the adhesion of a thin film to its substrate, with the most common being the slip test, peel test, laser shockwave ablation test, and the scratch test [22]. For the case of very thin (µm range), hard, strongly bonded layers such as tribological coatings for tools or dielectric layers on Si, the slip and peel tests are unlikely to produce useful information because of their reliance on the strength of an external adhesive to attach the tester to the film. Laser-induced shockwave tests are very difficult to model and quite dependent on substrate influence [22]. The scratch test has therefore become the method of choice for determining adhesion of thin hard layers. In this test, a hard body such as a spherical diamond tip is drawn across the coating under a constant or increasing load (Figure 4.18). The applied load, frictional force, and acoustic emission from the coating are all monitored during the test.

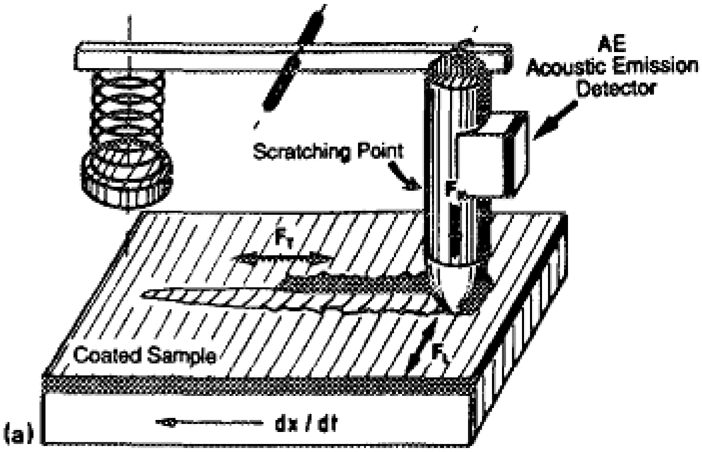

Figure 4.18: Schematic diagram of scratch adhesion test, reprinted from [22]

To obtain information about the coating's adhesion, the test parameters are modified until some type of failure is observed. The motion of the rigid indenter across the surface of the film produces stress fields both ahead of and behind the advancing tip, eventually leading to some type of failure in the film, substrate, or interface (Figure 4.19). The applied load at which failure occurs is known as the *critical load* (L_c) and the magnitude of the critical load is indicative of the quality of adhesion of the film to the substrate.

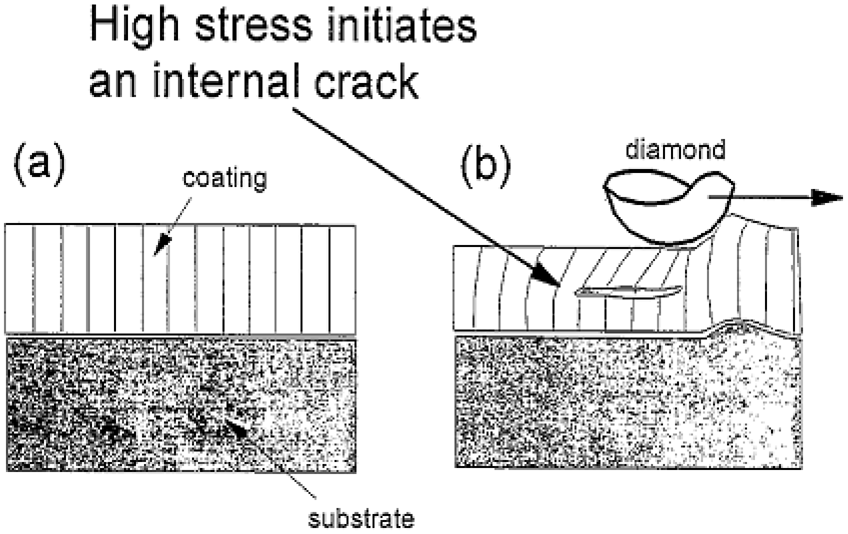

Figure 4.19: Coating failure during scratch test, reprinted from [88]

In the progressive load scratch test, the load is steadily increased as the indenter tip is drawn across the coating. This is commonly used for a quick first assessment of L_c. In the constant load scratch test, the load is not varied during the scratch but rather between successive scratches, allowing for more precise determination of L_c. The failure of the coating is typically noticeable in the scratch test data by a sharp increase in acoustic emission [22] and an inflection point in the frictional force curve [88]. However, a more precise means of determining the critical load is by using optical or electron microscopy to observe the scratch track. For the progressive load test, because the applied load increases linearly with distance travelled, it is possible to relate the location of a feature (such as a crack) in the scratch track to the applied load at that point.

If the test parameters (tip radius, load, loading rate, scratch speed) for a progressive-load test are well chosen, it may be possible to observe multiple stages of failure in the same scratch track and thereby delineate multiple critical loads L_{c1}, L_{c2}, etc. There is some variation between researchers in the criteria applied for determining each critical load, with commonly used points being the load at which the first crack appears, the load beyond which cracking becomes continuous, the load at which the film begins to chip or flake off the substrate, the load beyond which the film is continuously removed, and so on. It is therefore necessary to clearly explain when discussing scratch test data the definition of each critical load being compared.

In many cases the *type* of failure observed at the critical load is more important than its actual magnitude. In addition to film-substrate adhesion, the magnitude of a scratch testing critical load is affected by the substrate hardness, coating hardness, coating thickness, coating-indenter adhesion, and the radius of the indenter tip used [22]. Magnitude of a critical load is therefore mainly only useful in comparing between similar coatings on the substrate. Quantitative determination of the film’s adhesion strength and interface toughness is possible but requires extensive knowledge of the mechanical properties of the film and substrate and relies on simplifying assumptions [89]. Some of the most common failure modes during scratch testing are shown in Figure 4.20.

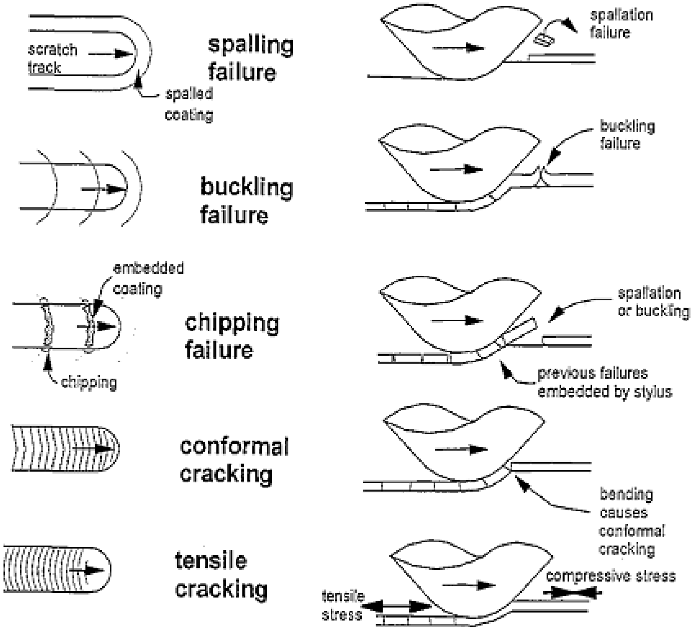

Figure 4.20: Failure modes in scratch adhesion testing, reprinted from [88]

Large-area spallation, chipping, or buckling of the coating is typically indicative of poor adhesion between the coating and interface. In the case of good adhesion, failure is more likely to occur by cracking within the film or in the case of brittle substrates, cracks penetrating the film and substrate [90]. Likewise the direction of the cracks develops information about the initial stress state of the film. Hard, brittle films or those under compressive stress will tend to exhibit buckling, conformal cracking, or Hertzian cracking while tensile cracking may be observed for softer films or those with an initially tensile stress state. Hertzian cracking, not shown in Figure 4.20, is indicated by the presence of cracks with a distinctive circular direction of propagation. At low loads, one may observe a single circular crack in the coating; at higher loads, a pattern of interlocking rings appears along the scratch track. This type of crack gets its name because it can be produced by the pressure of a spherical indenter on the flat surface of a brittle material, which was the original surface contact problem described by Hertz in 1881 [6]. The presence of this type of crack generally indicates that significant plastic flow is not occurring prior to failure.

Scratch testing in this work was performed using the CSM Instruments Micro-Combi Tester (MCT) at École Polytechnique de Montréal. The MCT supports scratch and microindentation (though not nanoindentation) testing as well as reciprocating wear testing using counterbodies such as Al_2O_3 balls. It is equipped with load sensing, frictional force sensing, acoustic emission detection, an optical microscope, and depth profiling tools. Maximum load for scratch testing is 30N and load resolution is 0.02N. Constant load, progressive load, and multi-pass scratch tests can be performed and Rockwell spherical diamond tips of 800μm, 200μm, 100μm, and 50μm are available. Determination of critical loads was performed using optical microscopy.

4.6 Pin-on-Disk Testing

Coatings for applications such as cutting tools or gears are required to withstand abrasive wear during their working lives. The pin-on-disc is the simplest and most common of several test geometries used to study the lifetime of a coating under wear conditions. In the pin-on-disc test, a steel or ceramic ball (pin) is pressed onto a flat sample (disc) of the material being tested by a hinged arm (Figure 4.21). The contact can be dry or lubricated; lubricated contacts are used for the characterization of lubricants or the characterization of contacting materials under lubricated sliding conditions. A constant load is applied to the pin and the disc is forced to rotate at a constant speed by an electric motor.

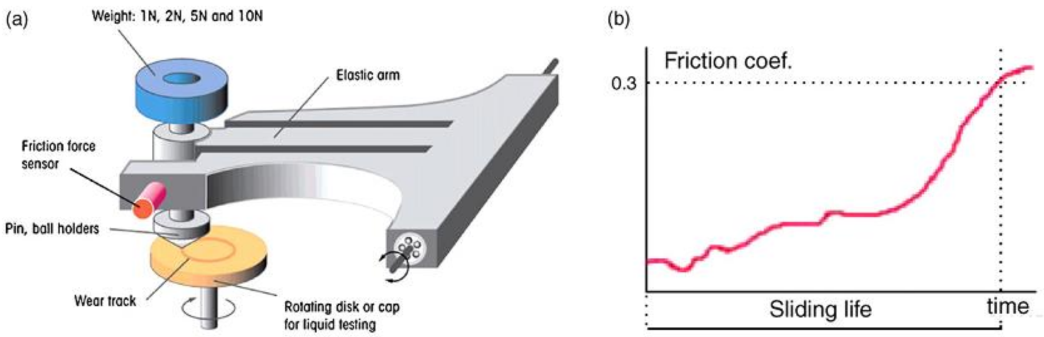

Figure 4.21: A pin-on-disc test setup, reprinted from [91, p. -]

The sliding pressure of the pin on the disc wears away material from both interacting bodies. As this process occurs, the frictional force, total sliding distance, and normal force are monitored to determine the evolution of the friction coefficient over time. Many instruments will also incorporate an acoustic emission sensor similar to the case for the scratch test. Eventually, a sharp increase in the friction coefficient is observed as the coating begins to fail. If the test parameters (load, sliding speed, number of revolutions) are well chosen, the coating will be left with a circular wear scar with approximately uniform depth and width. If the coating is completely removed during the test, it will not be possible to calculate a wear rate.

Typically, for hard tribological coatings, the most reliable way to estimate the volume of the scar is by using an optical or mechanical profilometer. The depth across the scar is scanned at several locations around its circumference, and integrals are computed to determine the cross-sectional area. Averaging the cross-sectional area from a few locations and multiplying by the circumference of the track determines the volume of material removed. The wear rate is the volume of material removed per unit applied energy and is expressed in units of $mm^3/(N*m)$. It is important to note that wear rate is strongly dependent on the test parameters as well as the material coupling itself.

Pin-on-disc testing in this work was performed at École Polytechnique de Montréal's Functional Coatings and Surface Engineering Laboratory (FCSEL). The pin-on-disc setup uses discrete masses to provide loads from 0.5 to 50N, and is capable of sliding speed ranging from 0.01 to 0.5 m/s. Available counterbodies include Al_2O_3, Si_3N_4, WC-Co, and high-speed steel balls of 3/16" and 1/8" radius.

5 Silicon Aluminium Oxide (SiAlO) Films

Prior to undertaking the growth of SiAlON materials using the ECR-PECVD system, it was decided to prepare and investigate a set of films from the simpler SiAlO materials system. It was intended to develop relationships between gas ratio, film refractive index, actual composition, and mechanical properties. Previous studies [12] of SiAlO materials grown on this ECR-PECVD system estimated Al incorporation of up to 6% depending on precursor cell temperature, but precise compositional characterization via RBS proved difficult due to the close atomic masses of Al and Si. To that end, it was decided to grow thin (<50 nm) films for RBS in an attempt to obtain separate Al and Si peaks. Substrates used were 3” p-type <1 0 0> Si wafers of 525 μm thickness. This substrate was chosen due to thickness (for durability in mechanical testing), system compatibility, and availability. Native oxide was not removed prior to deposition.

By contrast, mechanical characterization (nanoindentation, scratch testing, pin-on-disk) requires thick (~1 μm) films in order to obtain consistent results. For these reasons it was decided to grow two sets of SiAlO films with identical deposition conditions but different growth times. Growth parameters from [12] were used as the starting point for the study. It was expected that significant (at least several %) Al incorporation would be required in order to noticeably affect optical and mechanical properties of the films. Starting with a reference film of SiO_2 (5 sccm SiH_4/Ar to 30 sccm O_2/Ar), the Al content was modified by increasing the precursor cell temperature. To reach even greater Al content, the

SiH_4/Ar flow was then decreased down to a minimum of 2 sccm with O_2/Ar being adjusted at lower flow rates to avoid producing oxygen-rich films.

A set of eight calibration films, including a reference film without Al incorporation, as well as five thicker films for mechanical testing were deposited in February 2012 (Table 5.1). Stage heater temperature was 350°C, producing a substrate temperature of 137°C, and plasma power was 500W. Chamber base pressures ranged from $1.6*10^{-7}$ to $2.9*10^{-6}$ Torr.

Table 5.1: SiAlO films deposited on Group IV-McMaster ECR-PECVD

Sample	Date	Gas flow [sccm]			Partial pressure [mTorr]				Al cell temp [°C]	Run time [min]
		SiH_4 in Ar	O_2 in Ar	Al carrier	SiH_4 in Ar	O_2 in Ar	Al carrier	Total		
SiO2-ref2	01-Feb	5	30	0	0.55	3.05	0	3.6		9
SiAlO-01	02-Feb	5	30	10	0.55	3.05	1	4.6	182	9
SiAlO-02	03-Feb	5	30	10	0.55	3.05	1	4.6	196	9
SiAlO-03	03-Feb	5	30	10	0.55	3.05	1	4.6	213	9
SiAlO-04	04-Feb	4	30	10	0.45	3.05	1	4.5	217	10
SiAlO-05	04-Feb	3	30	10	0.35	3.05	1	4.4	217	12
SiAlO-06	04-Feb	2.5	25	10	0.3	2.6	1	3.9	216	14
SiAlO-07	06-Feb	2	20	10	0.25	2.15	1	3.4	218	16
SIAlO-03T	22-Feb	5	30	10	0.6	3	1.1	4.7	216	300
SIAlO-04T	23-Feb	4	30	10	0.5	3.1	1	4.6	218	360
SIAlO-05T	24-Feb	3	30	10	0.4	2.9	1.2	4.5	216	480
SIAlO-06T	25-Feb	2.5	25	10	0.3	2.7	1	4	218	600
SIAlO-07T	26-Feb	2	20	10	0.25	2.2	1.05	3.5	216	600

5.1 Ellipsometric Characterization

SiAlO films produced for this study were characterized using the Woollam M-2000U VASE system (with NIR option). Data were collected over 676 wavelengths from 245-1690nm (0.735-5.038eV) at 5 angles (55°, 60°, 65°, 70°, 75°) using a 5-second acquisition time. Samples were stabilized by the in-stage vacuum system during acquisition. The samples were dusted with high-pressure N_2 gas prior to measurement to avoid the effects of contaminant particles. It was intended to quantify the thickness and refractive index of the deposited films while also gaining qualitative data regarding their dielectric properties.

Both SiO_2 and Al_2O_3 exhibit Cauchy dispersion behaviour over the wavelength range of interest. Significantly Si-rich films containing Si nanocrystals or nanoclusters will exhibit different dispersion behaviour, but SiAlO films produced for this study were expected to be near-stoichiometric (excepting substitution of Si by Al). In practice it was found that modelling the optical constants of the films using only the first two terms of the Cauchy dispersion relation and neglecting the effects of absorption ($k=0$) was sufficient to produce agreement with collected data. In the interest of consistency between results and minimizing the number of fit parameters, a simple model with only three layers (Si wafer substrate, native oxide, uniform Cauchy film) was used. This model was used to fit the thickness and refractive index of the seven thin SiAlO films and a reference SiO_2 film grown on the same system (Table 5.2).

Table 5.2: Thickness, refractive index, and growth rate of thin SiAlO films

Sample	Al cell temp (°C)	Al carrier : SiH_4 ratio	Thickness (Å)	n @ 632.8nm	Growth rate (Å/min)
SiO_2-ref2	0	0.0	274.9±0.4	1.4875±0.0007	30.55±0.03
SiAlO-01	182	6.1	260.6±0.3	1.4867±0.0007	28.95±0.03
SiAlO-02	196	6.1	298.5±0.3	1.4877±0.0006	33.16±0.03
SiAlO-03	213	6.1	252.5±0.3	1.4982±0.0008	28.05±0.03
SiAlO-04	217	7.4	249.8±0.4	1.5045±0.0008	24.98±0.03
SiAlO-05	217	9.5	239.1±0.4	1.5099±0.0008	19.92±0.03
SiAlO-06	216	11.1	239.6±0.5	1.517±0.0008	17.11±0.02
SiAlO-07	218	13.3	240.8±0.5	1.4821±0.0009	15.05±0.02

Goodness of fit for the thin (~25 nm) films was excellent, with the MSE estimator less than 2 in all cases. Attempting to account for optical absorption did not appear to produce much improvement in the fit quality or change in the fit parameters, validating the assumption $k=0$. Likewise, accounting for the surface roughness of the films using the effective medium approximation had little impact on the model; this indicates a smooth (<5Å roughness) film surface and is not surprising given the low thickness of the films.

Increasing the aluminium cell temperature from 180°C (SiAlO-01) to 220°C (SiAlO-03) appeared to have little impact on the refractive index of the deposited films. This indicates that the amount of aluminium being incorporated under these growth conditions is relatively low (probably <1%), which is consistent with previous studies on Al-doped SiO_x films [12]. However, all Al-doped films had increased refractive index in comparison with the undoped SiO_x reference. This could be an effect of the increased Ar partial pressure of the dopant carrier gas, or the increased total deposition pressure. With the cell temperature at 220°C, increasing the ratio *R* of Al carrier to SiH_4 produced an upward trend in the refractive index, indicating greater Al incorporation. Optical constants for all SiAlO films displayed very similar shape (Figure 5.1).

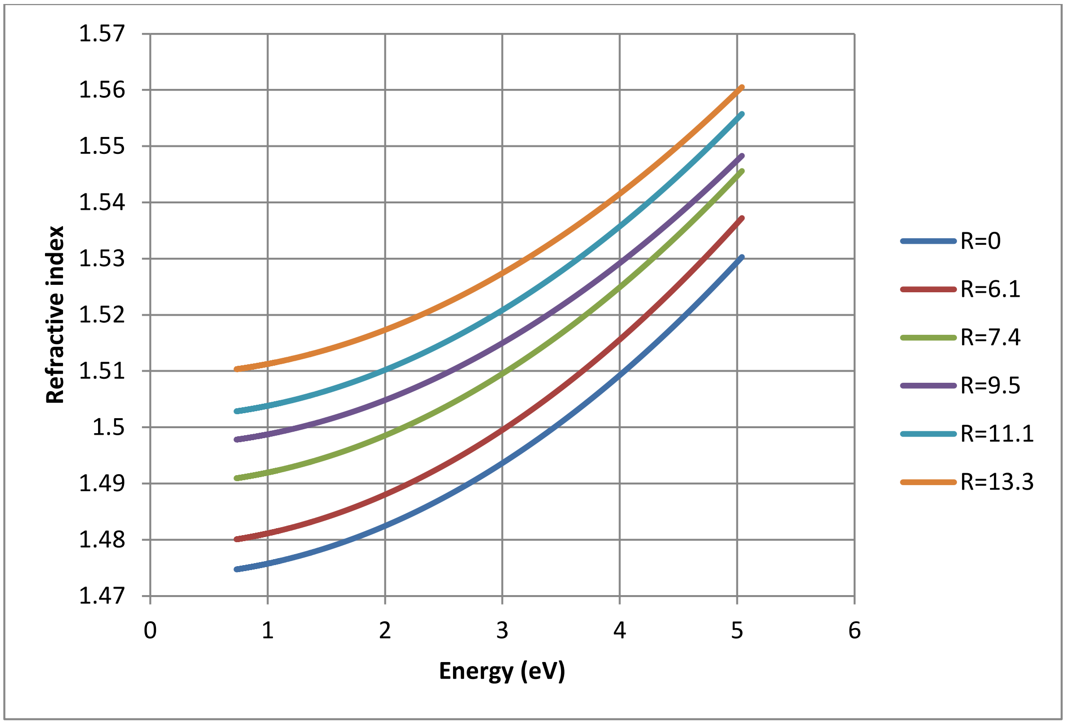

Figure 5.1: Refractive index of thin SiAlO films vs. photon energy

A plot of the refractive index *n* of the films at the HeNe laser wavelength (632.8nm or 1.960eV) against the gas ratio *R* exhibits a clear linear dependence of *n* on *R* (Figure 5.2). However, the changes in *n* were small in magnitude despite the large range in *R* studied. This is not surprising given the relatively small difference in *n* between SiO_2 and Al_2O_3.

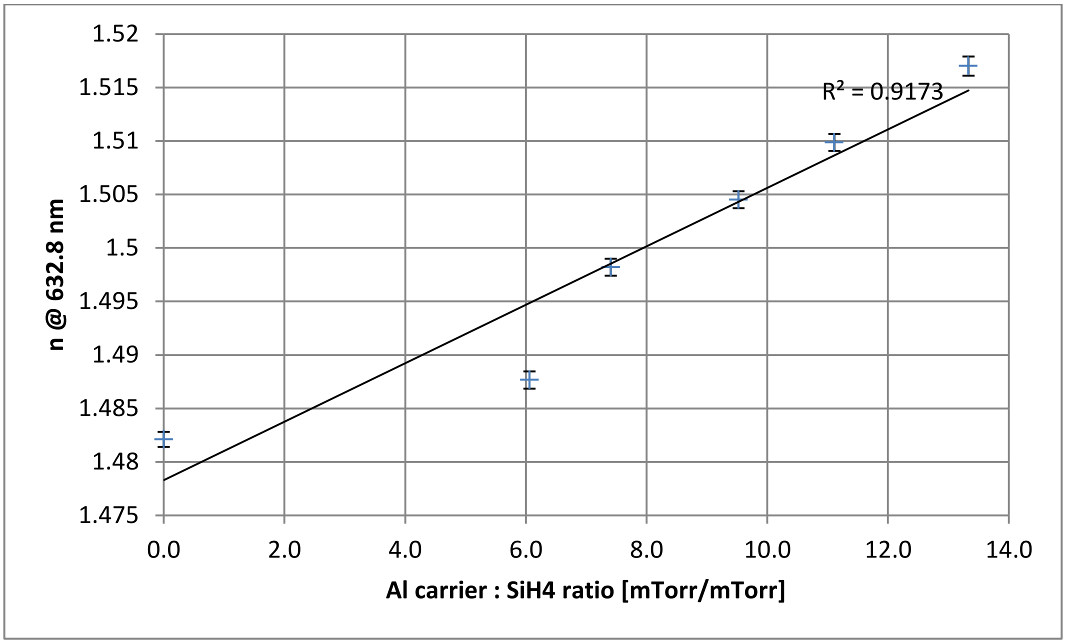

Figure 5.2: Refractive index vs. partial pressure ratio for thin SiAlO films

The ellipsometric model had to be adjusted for the analysis of the thicker SiAlO films. The influence of the thin (1-3nm) native oxide is less significant and it was removed from the model to cut down on free parameters. Inclusion of an effective medium approximation layer simulating surface roughness significantly improved fit quality (MSE reduced by 6). There are thus three layers in the model (substrate, Cauchy film, and roughness EMA layer). The films showed absorption in the ultraviolet (>3.351 eV) region of the spectrum. To allow for the use of the assumption *k=0*, analysis was confined to the near-IR and visible regions of the spectrum (1.378-3.351 eV). This model produced fits to collected spectra with MSE<15 for all five films (Table 5.3) Surface roughness was estimated at 60-100 Å, or approximately 1% of film thickness.

Table 5.3: Thickness, refractive index, and growth rate of thick SiAlO films

Sample	Run time (min)	Al carrier : SiH_4 ratio	Thickness (Å)	n @ 632.8nm	Growth rate (Å/min)
SiAlO-03T	300	6.1	9718±3	1.4843±0.0003	32.394±0.001
SiAlO-04T	360	6.7	9297±2	1.4796±0.0003	25.825±0.001
SiAlO-05T	480	10.0	9228±2	1.482±0.0003	19.225±0.001
SiAlO-06T	600	11.1	9905±2	1.4787±0.0003	16.508±0.001
SiAlO-07T	600	14.0	7370±2	1.4731±0.0003	12.283±0.001

No clear trend in refractive index with gas ratio was observed and variation across the five films was very slight. This correlates with the low film Al incorporation measured in Section 5.3. Growth rates of both thin and thick films were linearly correlated with SiH_4 flow (Figure 5.3).

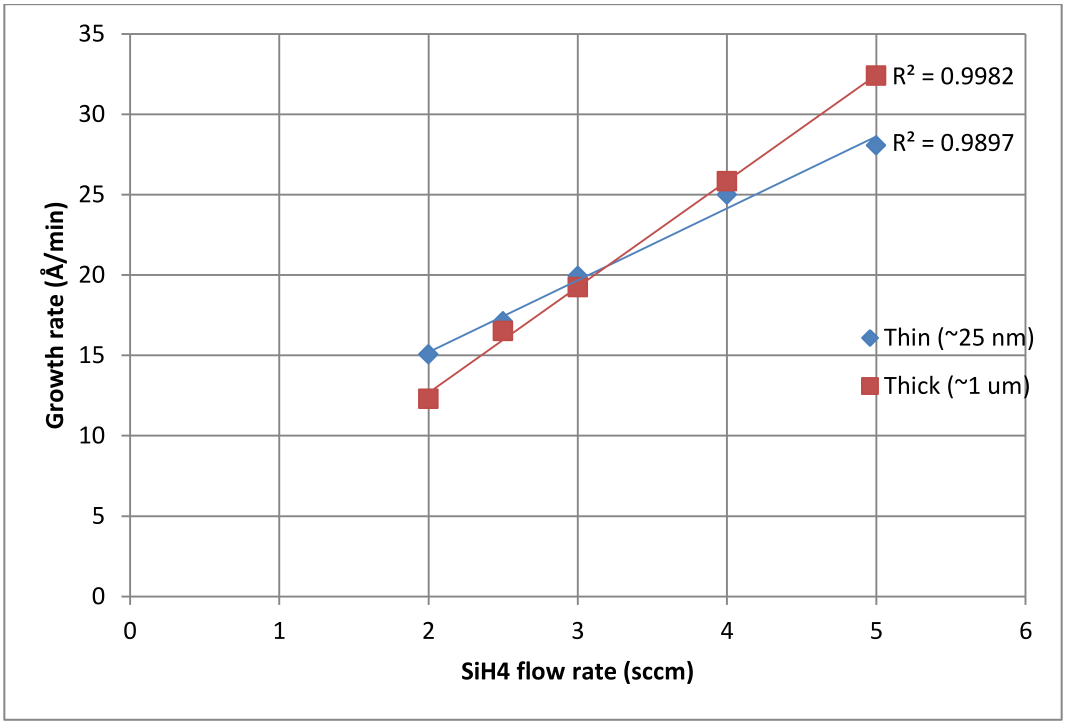

Figure 5.3: Effect of silane flow rate on growth of SiAlO films.

5.2 Ion Beam Analysis

It was desired to determine the atomic concentration of Al in the SiAlO films and develop a relationship between this quantity and the optical and mechanical properties of the films. It was expected that higher Al content would lead to improved mechanical properties of the films, and that the effects would not be very noticeable at less than a few percent Al. The seven thin SiAlO films and the SiO_x reference were analyzed using RBS at Western University in London, Ontario, and the five thick SiAlO films were analyzed using HIERDA at the Université de Montreal (U de M).

5.2.1 Rutherford Backscattering Spectrometry (RBS)

Previous RBS studies on Al-doped SiO_x films produced by the Group IV-McMaster ECR-PECVD had demonstrated Al incorporation up to 6 at% [12], but also highlighted some of the difficulties in quantifying the Al content of the films. Obstacles interfering with the quantification of Al in a SiAlO film include the decreased sensitivity of RBS to lighter elements, the close atomic masses of Al and Si leading to spectrum overlap, and the difficulty in resolving the small signal produced by the few percent of Al in the film when it is riding on top of the much larger signal from the Si film and substrate. Based on simulations, for a typical 100 nm SiAlO film consisting of approximately stoichiometric SiO_2 with 6% Al incorporation, the Al peak would appear only as a slight (50-100 counts) lip on the Si substrate signal and a change in shape of the Si “shoulder” produced by the film (Figure 5.4). When the effects of noise are added in (typically also in the range 50-100 counts), accurate quantification becomes extremely difficult.

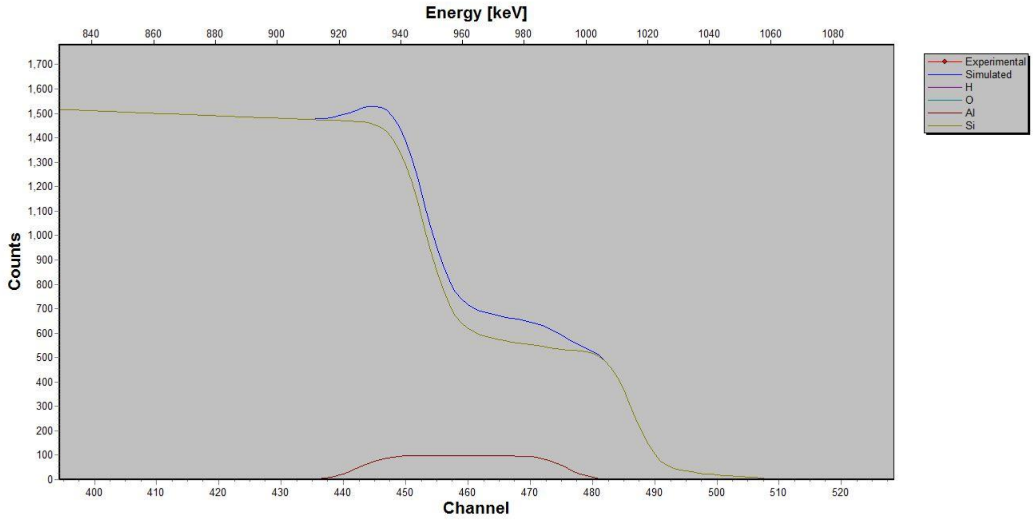

Figure 5.4: Simulated 1.8 MeV RBS spectrum for 1000 at/cm^2 SiAlO film

Three steps were taken to overcome these difficulties. First of all, it was decided to move to thinner (~25 nm) films in an attempt to produce data with separated Si and Al peaks. Secondly, it was decided to increase the ion energy to produce sharper peaks with less sloping sides and therefore less overlap. And finally, to eliminate the large background signal from the Si substrate, it was decided to attempt a channelled ion measurement. It was hoped that these steps would produce clearly visible and separately resolved Al and Si peaks and thereby enable simple, accurate quantification. Assuming the effects of the substrate signal could be completely eliminated; simulation results appeared promising (Figure 5.5).

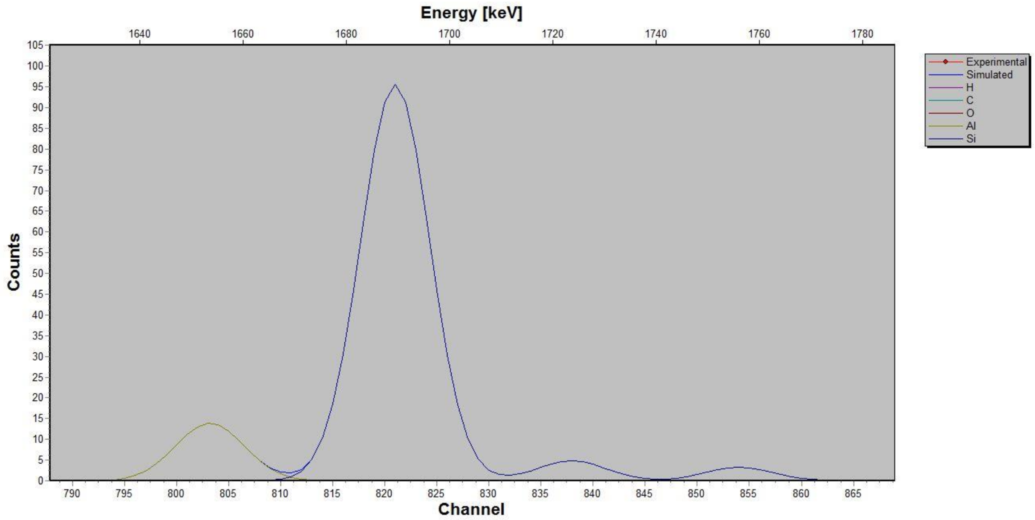

Figure 5.5: Simulated 3 MeV RBS spectrum for 250 at/cm^2 SiAlO film

Unfortunately, increasing the energy of the ion beam for RBS leads to reduced interaction cross section with the atoms in the film and substrate. This results in each peak containing far fewer counts thereby reducing the accuracy of the estimated elemental composition. For the SiAlO films, the estimated Al peak contained an integrated total of ~100 counts which indicates at least 10% relative uncertainty (because uncertainty in statistical measurements scales with the inverse square root of counts). Furthermore, the channeling procedure failed to completely eliminate the Si substrate signal and what remained of the signal became very difficult to model. And finally, given the typical 50-100 counts of noise in the data it becomes impossible to distinguish a legitimate Al peak from experimental noise (Figure 5.6).

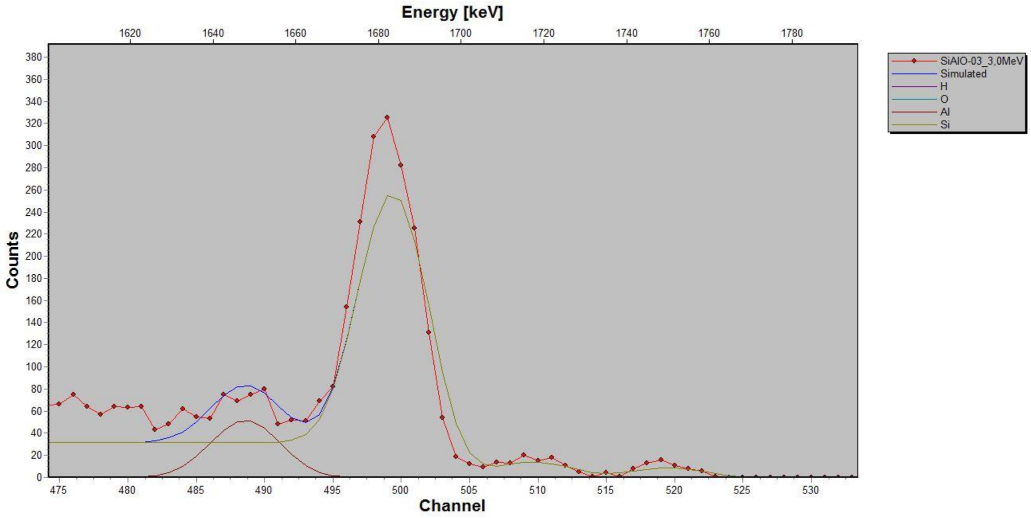

Figure 5.6: Fit to RBS spectrum collected from SiAlO film

It was decided given the difficulty involved with modeling channeled data, the lack of a clearly visible Al peak, and the likely poor quality of any fits that could be produced, to abandon RBS as a technique for characterizing the SiAlO films' composition. While it is possible that the difficulties could be worked out with better experimental design or longer data collection time, other alternatives for compositional characterization appeared more attractive.

5.2.2 Heavy-Ion Elastic Recoil Detection Analysis (HIERDA)

As part of the effort to evaluate the Al content of the SiAlO samples, the five thick samples were analyzed using the HIERDA technique at the Université de Montreal's heavy ion beam facility. Samples were bombarded with a beam of 35 MeV Cl ions with recoiled atoms being collected by a time-of-flight detector. Unfortunately, no trace of Al was visible in the HIERDA results (Figure 5.7).

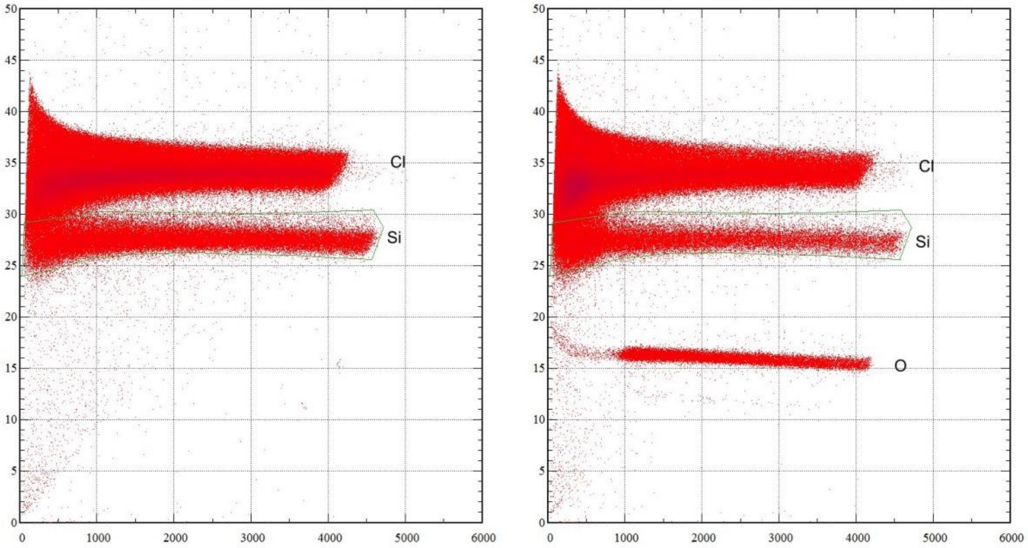

Figure 5.7: HIERDA results for Si reference (left) and SiAlO film (right)

It was indicated by researchers at the ion beam laboratory at U de M that their detection limit for Al in SiO_x was likely on the order of a few at%, and that below this level it was likely that the wide Si signal would overlap and drown out the Al signal (similar to the issue encountered during RBS analysis). Nevertheless, some useful data was gleaned from the HIERDA analysis. Approximate upper limits for Al (~3at%), C (~5at%), and H (~10at%) content in the films were determined by means of this study.

5.3 Energy Dispersive X-ray (EDX) Analysis

With the results of ion beam analysis failing to conclusively demonstrate the presence of Al in the deposited films, it was decided to undertake an SEM-EDX study of the thicker films in an attempt to analyze the Al content. Unlike IBA, EDX was expected to be able to clearly resolve separate peaks corresponding to Si and Al fractions in the films. This was also beneficial in that while thick and thin films were deposited at identical gas flow ratios, directly measuring the composition of the thicker films would be better able to account for shifts in system behaviour between runs.

The ellipsometric characterization of the thick SiAlO films had indicated thicknesses ranging from 730-990 nm. An accelerating voltage of 5 kV was selected to ensure efficient excite the Si K X-ray at 1.839 keV, which was the highest energy ray expected from the films. CASINO Monte Carlo electron trajectory simulator was used to confirm the suitability of the selected voltage for analyzing the films, since it was necessary to ensure that the electrons would not generate X-rays from the Si substrate or skewed compositional data would result. A film composition of 10% H, 5% C, 56% O, 6% Al, and 28% Si was assumed for the purposes of the simulation as a worst-case scenario (because electron stopping power is lowest in the light elements). The results indicated that the X-ray emission volume would be confined to the region of the SiAlO film (Figure 5.8).

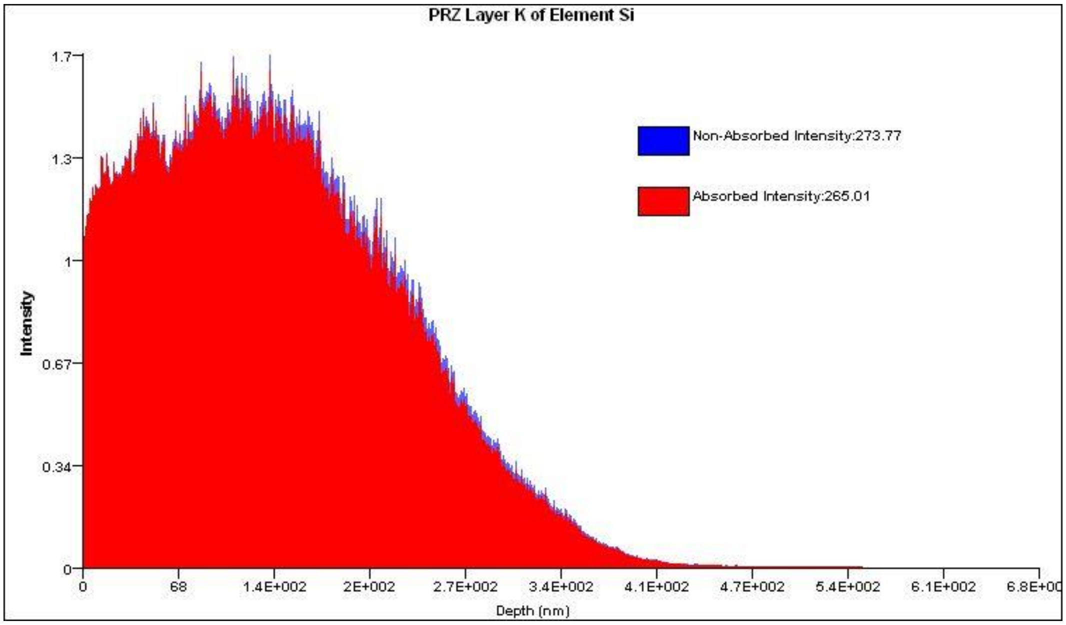

Figure 5.8: Simulated Si X-rays from 730 nm SiAlO:H film at 5 keV

EDX data were collected using the JSM-6610LV SEM at the CCEM. A capture time of 100 s was used to ensure sufficient X-ray counts for good statistics. To avoid charging, the samples were pre-coated with 9nm of C, which was used instead of Au to prevent interference with the generated X-rays from the light elements (O, Al, Si). X-ray spectra were collected as the electron beam was scanned across a large (~1-5mm^2) region to obtain a compositional average for the sample. Measurements were repeated three times using different areas of the sample to improve result quality. A 1.3μm film of thermal SiO_2 was used for comparative purposes during the characterization and to standardize the Si and O peak intensities. Contemporaneous standardization minimizes measurement errors incurred due to detector drift.

As expected, with increasing Al carrier/SiH_4 gas flow ratio during deposition the Al fraction in the deposited films was seen to increase (Figure 5.9). However, the measured Al content was significantly lower than that observed in [12] for films deposited under identical conditions (0.7 at% vs. 6 at%). This was determined to be most likely due to clogged precursor lines or a depleted Al precursor.

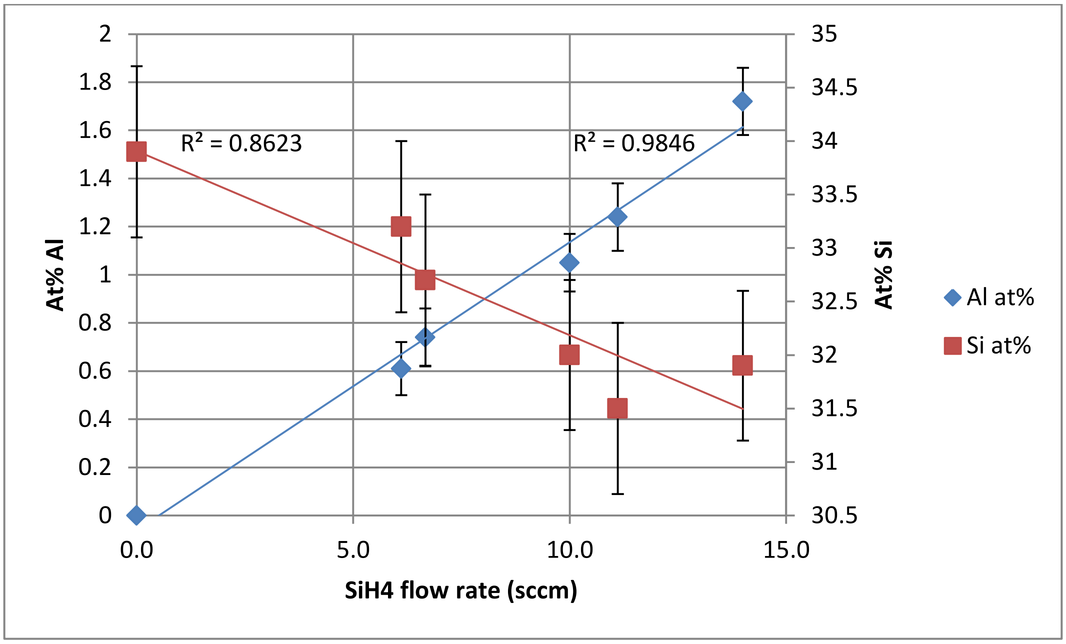

Figure 5.9: Al and Si atomic fraction (neglecting C and H) of SiAlO films

It is important to note that Al and Si concentrations estimated here are in truth *atomic fractions*, and not the true atomic concentration in the film. This is because H is not detectable by EDX, and the C coating eliminates the option of quantifying C in the film from this study. EDX returns quantification results in terms of wt%, which are converted to at% using the relative atomic mass A_r. For the example of Al, and assuming the film consists solely of H, C, O, Al, and Si, the value plotted in Figure 5.9 is calculated as

$$at\%\ Al = \frac{\frac{wt\%\ Al}{A_r, Al}}{\frac{wt\%\ O}{A_r, O} + \frac{wt\%\ Al}{A_r, Al} + \frac{wt\%\ Si}{A_r, Si}} \tag{5.1}$$

C K-rays were observed from both the SiAlO films and the thermal SiO_2 reference, which is expected due to the C coating. However, the count was noticeably higher in the case of the SiAlO films (Figure 5.10). This suggests the presence of C within the films' bulk, which is indicative of incomplete breakdown of the organic Al precursor.

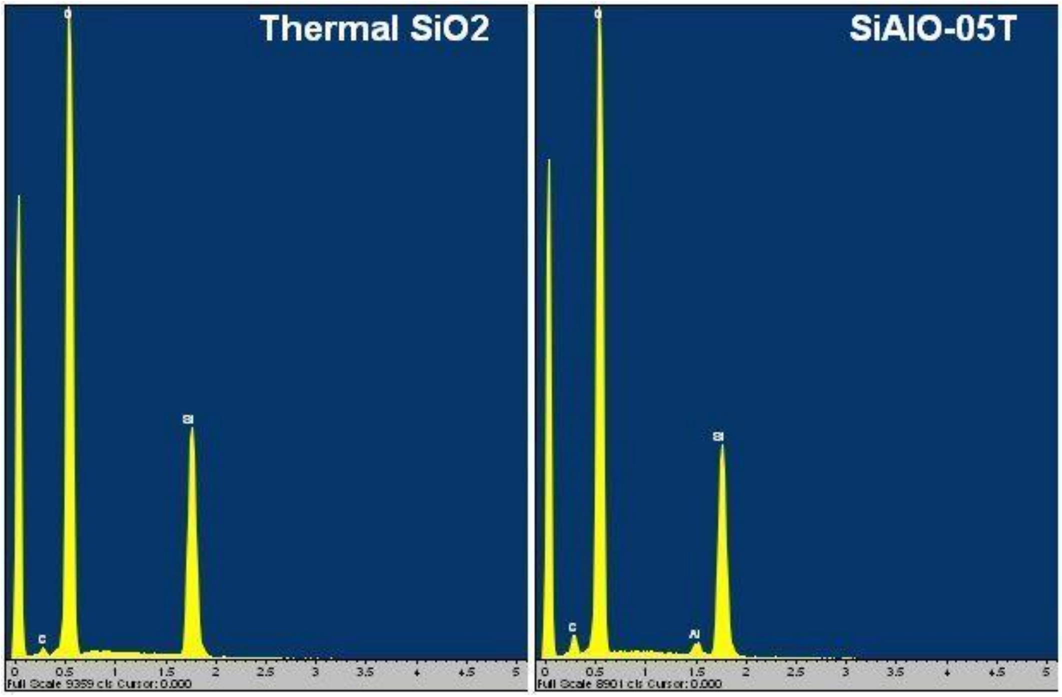

Figure 5.10: EDX spectrum comparison of thermal SiO_2 and SiAlO film

It was therefore decided to attempt quantification of C in the films by performing EDX on uncoated samples. However, C K-rays were still observed from uncoated thermal SiO_2 as well as the uncoated SiAlO samples. The C signal persisted following thorough (20 min) sonication in a solvent sequence of acetone-methanol-deionized water. This almost certainly indicates that C deposition is occurring *inside* the SEM chamber during the measurement, which is confirmed by the shift in secondary electron intensity in the rectangular regions scanned by the electron beam during EDX (Figure 5.11).

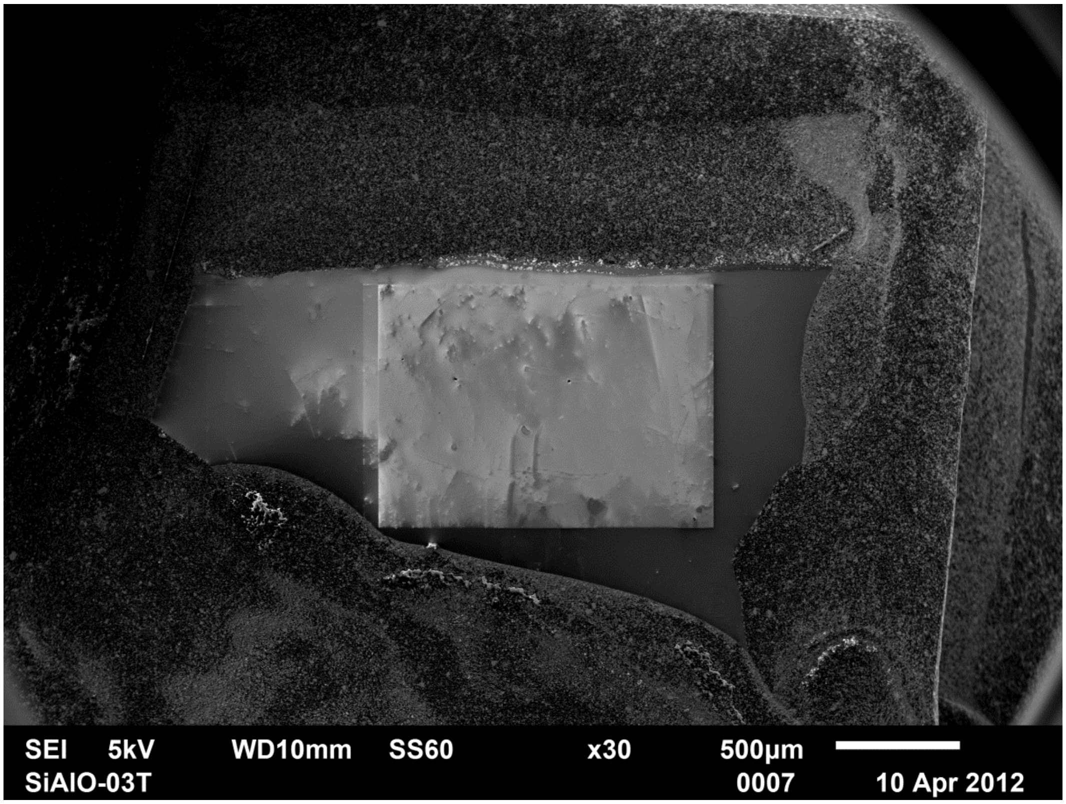

Figure 5.11: Evidence of C deposition during EDX raster scan

While it can be argued that the random C deposition occurring during the course of the EDX measurement makes accurate quantification of C impossible, it is notable that all SiAlO films measured exhibited a higher estimated C fraction than the thermal SiO_2 reference and that for any given film the estimated C fraction incorporated is larger than the Al fraction (Table 5.4). This is strongly indicative of incomplete breakdown of the precursor during deposition and suggests that multiple C atoms are incorporated along with each Al atom. It is therefore difficult to isolate the effects of Al incorporation on film optical and mechanical behaviour from the effects of increased C and precursor fragment content.

Table 5.4: Estimated atomic fractions (including C) of SiAlO films

	Al carrier : SiH_4 ratio	C (at%)	O (at%)	Al (at%)	Si (at%)
Thermal	0.0	2.3±0.3	65±1	0	32.5±0.7
SiAlO-03T	6.1	3.9±0.4	65±1	0.8±0.1	30.4±0.7
SiAlO-04T	6.7	3.5±0.4	66±1	0.9±0.1	29.9±0.7
SiAlO-05T	10.0	5.6±0.4	64±1	1.2±0.1	29.4±0.7
SiAlO-06T	11.1	3.8±0.4	65±1	1.5±0.1	29.4±0.7
SiAlO-07T	14.0	2.5±0.3	66±1	1.6±0.1	29.9±0.7

5.4 Nanoindentation Results

It was desired to determine the hardness and reduced modulus of the SiAlO films and relate these properties to film composition. The films were characterized using nanoindentation on the Hysitron TriboIndenter at Université de Montreal. The contribution of the substrate to the measured hardness of a film-substrate system is usually negligible if the indentation depth is less than 10% of the film's thickness; however this rule of thumb may not always apply to very thin (<1µm) films [87]. Accordingly, a series of 10 indentations with a Berkovich diamond was performed on each film at loads ranging from 1-10 mN, developing information about the change in mechanical properties with indentation depth in an attempt to extract information about the film alone.

5.4.1 Reduced Modulus

The measured reduced modulus of a film-substrate system (E') can be roughly approximated as linearly correlated with indentation contact depth h_c up to about 15% of the film's total thickness t [86]. The SiAlO films exhibited E_r increasing with h_c (Figure 5.12), indicating that the substrate Si wafer was stiffer than the film on top of it. The greatest relative depth reached during any measurement was 274.2±0.2 nm, corresponding to 0.37t for the 737±0.2 nm thick film SiAlO-07T. If it is desired to fit the E_r data with a linear trend, it is necessary to restrict the fitting to the region $h_c<0.15t$.

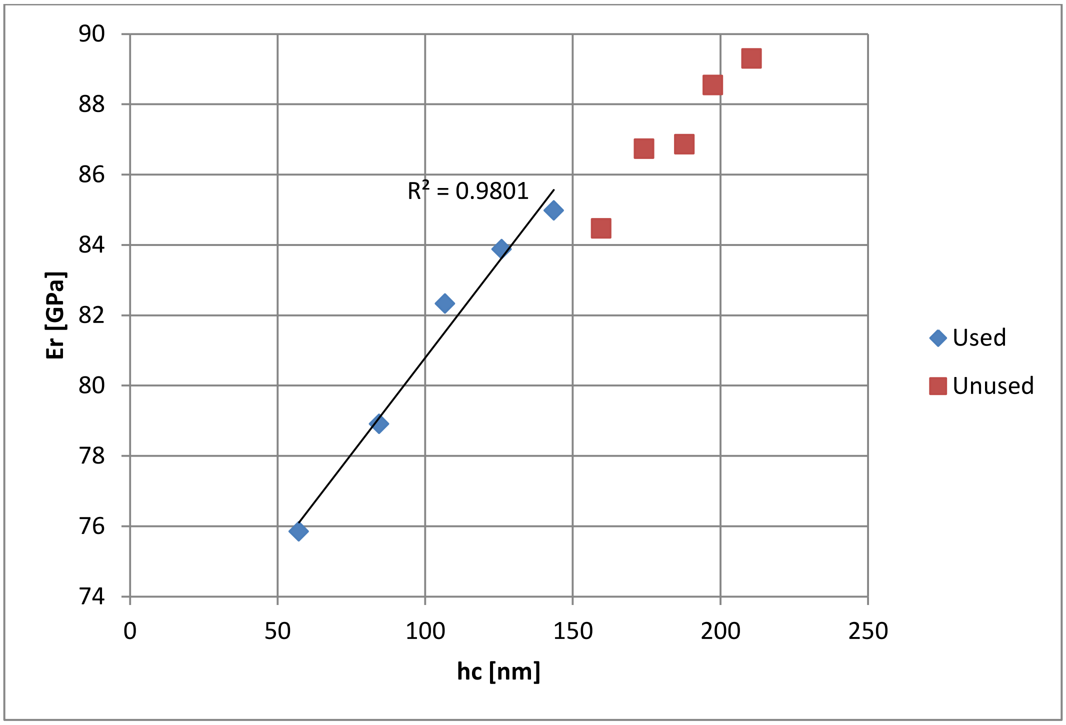

Figure 5.12 Measured reduced modulus vs. depth for film SiAlO-03T

For each SiAlO film measured, it is therefore possible to extract the film-only reduced modulus E_f from the measured modulus *E'* by first ruling out all indentation data with $h_{max} > 0.15t$ and then performing a linear regression fit to the remaining data. The fitting function used is given by

$$E' = E_f + (E_s - E_f) \cdot \frac{h}{t} \tag{5.2}$$

It can be seen that the extrapolation of *E'* to *h/t=0* yields the film-only reduced modulus E_f, which is also equal to the y-intercept of the linear function. Thus, E_f can be estimated by linear regression for all SiAlO films studied and the standard error of the intercept provides is an estimator of the accuracy. E_f, which is equal to the film-only reduced modulus E_r, is plotted against the Al content of the films in Figure 5.13.

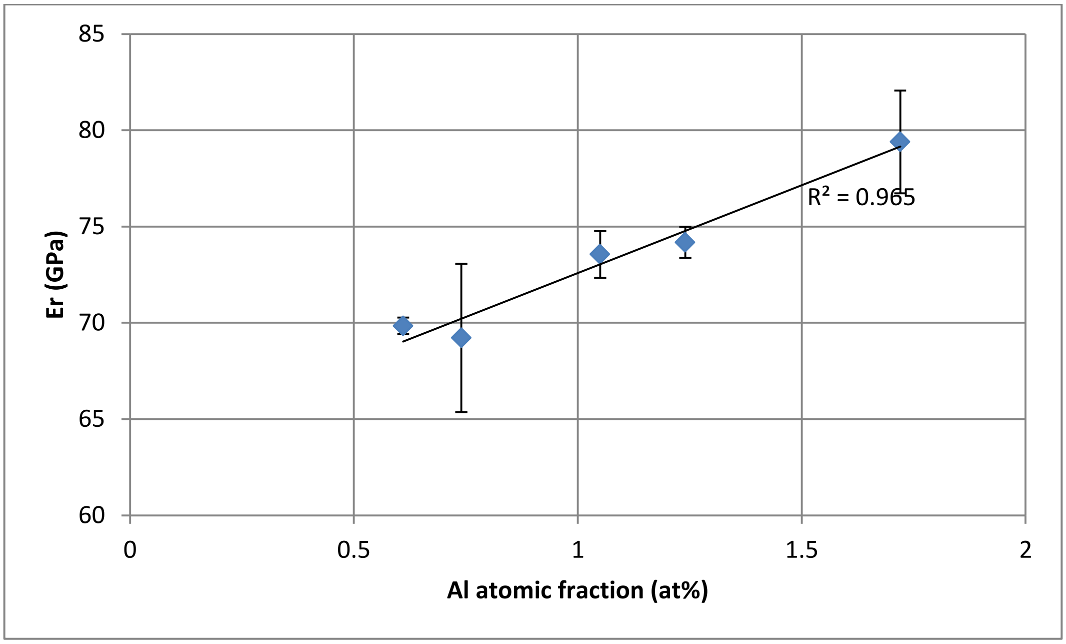

Figure 5.13: Reduced modulus vs. Al content for SiAlO films

As might be expected given the higher Young’s modulus of Al_2O_3 with respect to SiO_2, E_r linearly increases with Al content. This may also be related to the increased C incorporation from the Al precursor. The increase is small with respect to the overall magnitude of the reduced modulus or the size of the error bars, which is unsurprising given the small amount of Al in the film. In order to convert from E_r to the true Young’s modulus of the films, it would be necessary to know their Poisson’s ratio which was not measured in this study.

5.4.2 Hardness

For the case of a soft film on a hard substrate, the influence of the substrate on the measured hardness of the film-substrate system is generally insignificant for indentation depth h_c less than the film thickness [87] due to confinement of plastic deformation within the softer film. As expected, the hardness data measured did not exhibit any clear trend with h_c (Figure 5.14).

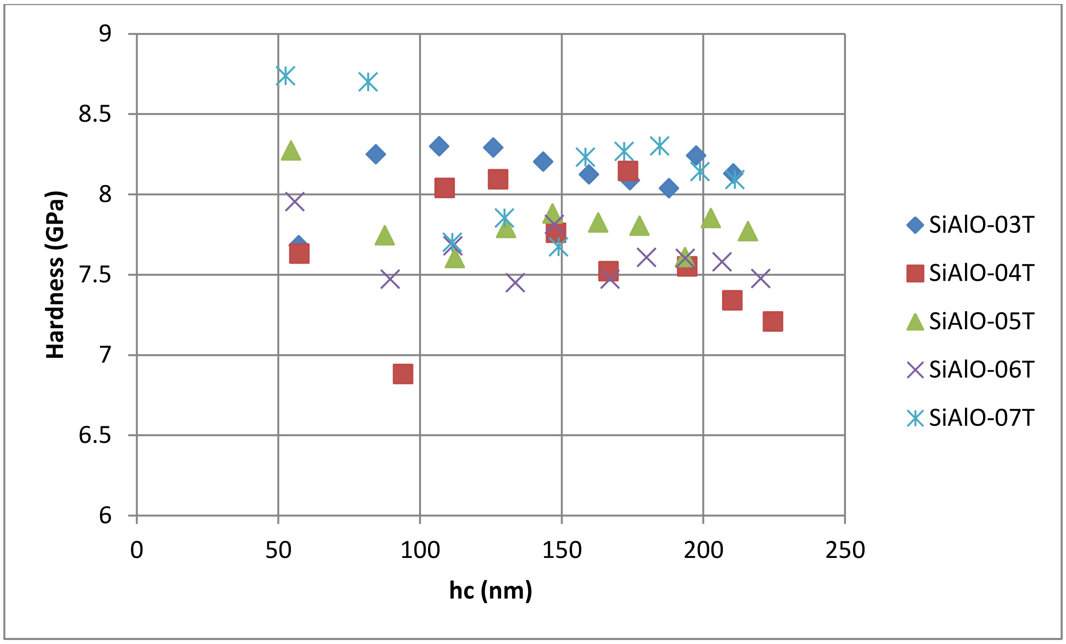

Figure 5.14: Hardness vs. indentation depth in SiAlO films

The film hardness and an estimate of the uncertainty in this measurement can therefore be found by computing the mean and standard error of the measured hardness data from each sample. The hardness data for the SiAlO films are plotted against their Al content in Figure 5.15. No clear dependence of the hardness on Al content was observed.

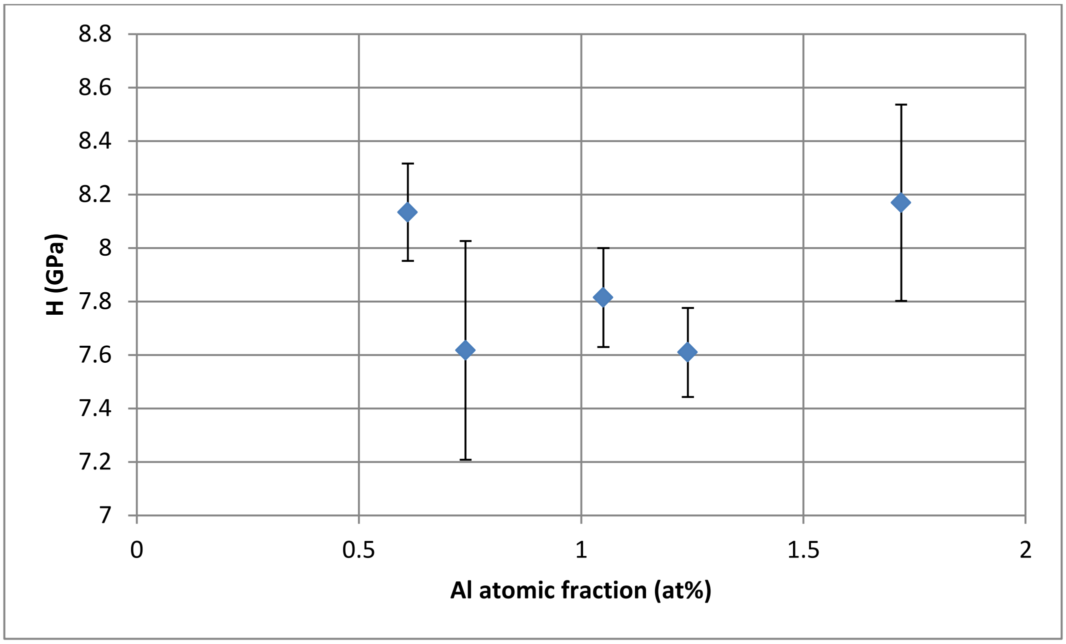

Figure 5.15: Hardness vs. Al content for SiAlO films

It is worth noting that the Young's modulus and hardness of bulk silica (SiO_2) are approximately 70±7 and 10±1 GPa respectively, while those of crystalline Si are 169.5±1.2 and 12.7±0.1 GPa [42]. Thus, the SiAlO films exhibited similar hardness and modulus to ordinary SiO_2 and have poorer mechanical properties than the Si substrate. This is to be expected given the relatively low Al incorporation in the films (<2% in all cases).

5.5 Pin-on-Disk Results

It was decided to characterize friction and wear behaviour of the five thick SiAlO films using the pin-on-disk tester at the Université de Montreal. Experimental parameters selected were a load of 1N (the minimum possible for the system), sliding distance of 10m, and sliding speed of 1m/min with dry 3/16" Al_2O_3 ball counterbody. Examination of the wear track indicated complete removal of the coating and significant wear of the substrate. Reduction of the sliding distance to 1m produced inconsistent wear with portions of the film being removed completely while others remained (Figure 5.16).

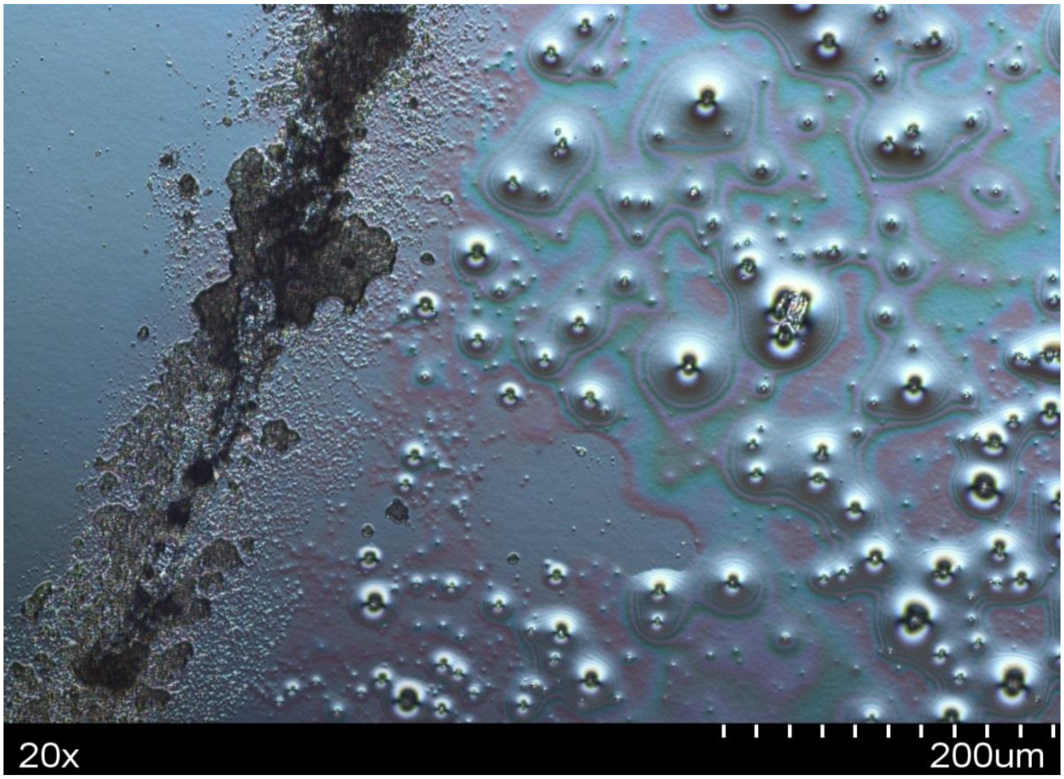

Figure 5.16: Wear track from pin-on-disk test on a SiAlO film

Based on these results, it was concluded that wear resistance of the coatings was too low to allow for any kind of friction or wear rate characterization using the pin-on-disk system. Accurate wear rate measurement requires a smooth consistent wear track with depth remaining entirely within the coating in order to be able to estimate the volume of material removed during the test. Also notable in Figure 5.16 is the presence of strange bubble-like growth defects in some areas of the films. These defects were likely caused by an insufficiently cleaned wafer surface prior to film deposition.

5.6 Scratch Results

Results of the pin-on-disk testing indicated the likely culprit for the poor wear resistance of the SiAlO films to be adhesion. It was therefore decided to attempt to compare and quantify the films' adhesion via scratch testing on the CSM Micro-Combi Tester at Université de Montreal. Initial experiments determined that a progressive load of 1 to 10 N applied along a 1 cm scratch track produced at 10 mm/min by a 3/16" Al_2O_3 ball allowed for the observation of a transition from no damage to occasional cracking to complete delamination of the coating. The scratch was repeated three times for each film to assess repeatability of the results. Based on observations of the first few scratch tracks, it was decided to compare the films by means of four critical loads:

1. Load at which the first crack in the film appears along the scratch track
2. Load at which cracking becomes continuous along the scratch track
3. Load at which delamination of the film from the substrate is first seen
4. Load at which the film is continuously delaminated from the substrate along the scratch track

Critical loads for each test were defined by observation at 20x magnification using an optical microscope. The manner in which the films failed was very similar in all cases, and consisted of tensile cracking in the film followed by delamination of chips of the film from the substrate (Figure 5.17).

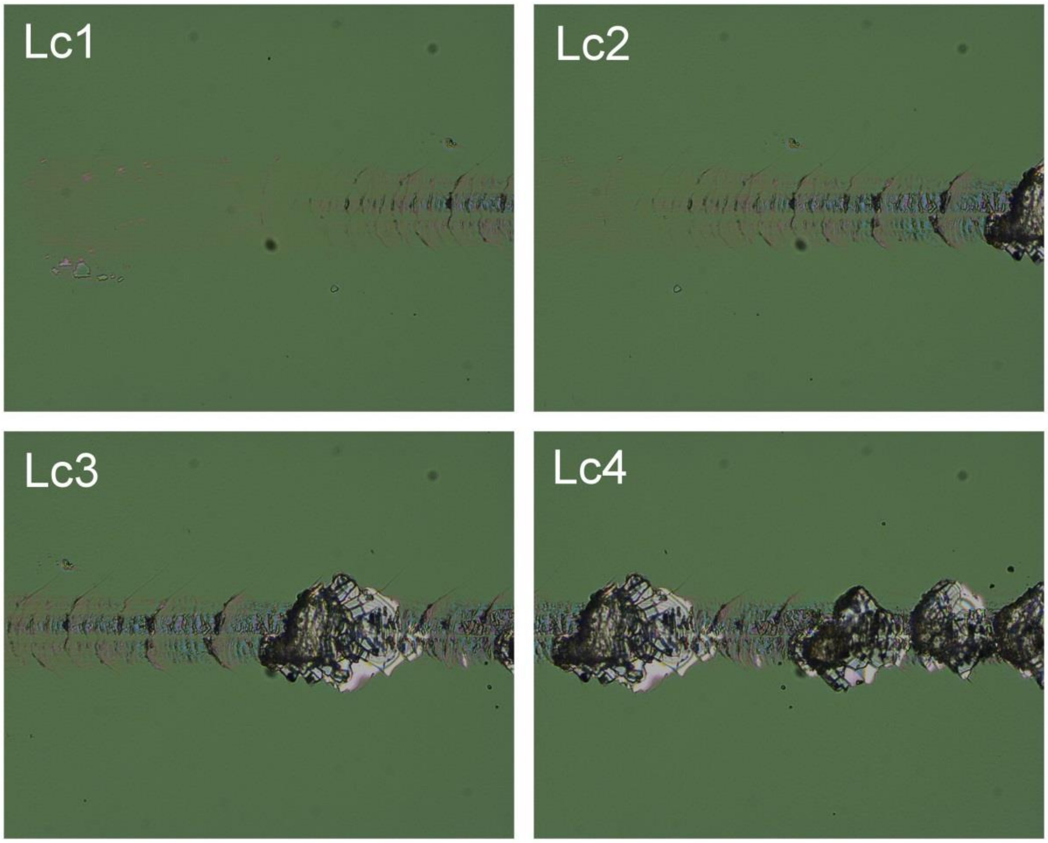

Figure 5.17: Critical loads 1-4 on sample SiAlO-03T, scratch direction to right

Qualitatively, there are two important things to note regarding the scratch tracks. The first is that cracking along the scratch tracks is of the *tensile* type, meaning that the film is being pulled apart as the loaded ball passes over it. This implies that the film is softer than the substrate on which is deposited. Secondly, it is notable that little chipping of the film is observed prior to its delamination from the substrate. This indicates that the adhesive strength of the film is inferior to its cohesive strength. Because the coating is transparent, the areas where it is lifted off the substrate can be observed by the presence of interference fringes.

For tribological coatings, good performance is indicated by delamination occurring at loads >20N when scratched with a 200 µm diamond tip. The use of a large radius Al_2O_3 ball reduced the magnitude of the stresses produced under the scratch tip and spreads them over a wider area. Despite this, all SiAlO films were observed to delaminate at loads between 1.5 and 2.5N (Table 5.5).

Table 5.5: Scratch test critical loads for five SiAlO films

Film	Lc1 (N)	Lc2 (N)	Lc3 (N)	Lc4 (N)
SiAlO-03T	1.2±0.1	1.5±0.3	1.7±0.3	1.8±0.4
SiAlO-04T	2.5±0.4	4±0.5	5±1.1	6.3±1
SiAlO-05T	1.2±0.1	1.3±0.1	1.5±0.1	1.8±0.3
SiAlO-06T	1.4±0.3	1.6±0.4	1.6±0.4	2.2±0.3
SiAlO-07T	1.3±0.1	1.3±0.1	1.3±0.1	2.2±0.6

SiAlO-07T exhibited the poorest scratch performance of the five films. This is not surprising given that it is significantly thinner than the others (737µm vs. >900µm). Thinner films have less volume in which to absorb the stress produced by the scratch and therefore tend to exhibit poorer performance. The much higher resistance to cracking and delamination exhibited by film SiAlO-04T indicate that this film has superior adhesion in comparison with the others. This is almost certainly due to a cleaner wafer surface prior to deposition. It is very unlikely that the improved adhesion of SiAlO-04T is related in any way to the growth parameters of this film.

6 Silicon Nitride (SiN_x) Films

Given the difficulties with Al incorporation from the precursor and quantitative estimation of Al content in the films, it was decided to move to studying mechanical properties of a simpler system such as SiN_x. The switch from oxides to nitrides was also expected to improve mechanical properties of the resulting films. Based on feedback received while measuring the SiAlO films at the FCSE facilities, it was decided to implement several changes to the film deposition recipe:

1. Increase growth temperature to improve density and lower H content
2. Increase gas flow rate to improve film deposition rate
3. Modify plasma power to improve film deposition rate
4. Strip native oxide using HF before deposition to improve adhesion

Before depositing the thicker films required for mechanical characterization, it was decided to undertake a study of the effects of these recipe changes on growth rate and refractive index of the deposited SiN_x films. Generally, a higher refractive index and the presence of absorption in the deposited film are indicative of a silicon-rich material. It was anticipated that films of lower refractive index (near-stoichiometric) would have superior mechanical properties to silicon-rich ones. Therefore, the objective of the search was to find deposition parameters that produced significantly increased growth rate without much increase in refractive index. The McMaster ICP-CVD system was selected for growing these films due to its higher ion energy and ability to use pure N_2 plasma, speeding growth.

Table 6.1: Selected SiN_x films deposited on McMaster ICP-CVD

Sample	Date	N_2 source	Gas flow (sccm)			Partial pressure (mTorr)			Plasma power (W)	Growth temp (°C)	Run time (min)
			Ar	N_2	SiH_4 in Ar	Ar	N_2	SiH_4 in Ar			
WNS-09	11-May	Plasma	27	3	10	2.15	0.2	0.6	500	187	30
WNS-10	14-May	Plasma	25	5	10	2	0.45	0.7	500	187	45
WNS-11	15-May	Plasma	0	30	10	0	2	0.5	500	187	30
WNS-12	15-May	Plasma	0	30	15	0	2	0.9	500	187	20
WNS-13	16-May	Ring	20	10	10	1.65	0.7	0.85	500	187	20
WNS-15	17-May	Ring	15	10	15	1.3	0.6	0.9	500	187	20
WNS-18	22-May	Ring	10	20	10	0.9	1.3	0.6	500	187	20
WNS-19	22-May	Ring	10	22	8	0.9	1.4	0.5	500	187	20
WPS-21	24-May	Plasma	0	30	15	0	2	0.9	500	253	30
WPS-22	24-May	Plasma	0	30	15	0	2	0.9	400	253	30
WPS-23	24-May	Plasma	0	30	15	0	2.05	0.95	300	253	30
WNS-27	23-Jul	Plasma	0	30	15	0	2	1.1	300	187	30
WNS-28	23-Jul	Plasma	0	27	18	0	1.8	1.2	300	187	30
WNS-29	24-Jul	Plasma	0	25	20	0	1.7	1.35	300	187	30
WNS-30	25-Jul	Plasma	0	23	22	0	1.6	1.5	300	187	30

Note that the SiN_x films listed in Table 6.1 are not a complete list of deposition parameters studied and are restricted to those films for which trends could be observed with changing parameters. A thorough study of growth rate and refractive index of SiN_x films grown on the McMaster ICP-CVD with SiH_4/Ar flow over 10sccm had not been previously attempted, since higher flow rates are not beneficial to luminescence properties. It was also desired to compare SiN_x films deposited in N_2 plasma versus those deposited in Ar plasma with N_2 introduced through the dispersion ring. Essentially, the films studied here can be divided into four groups:

1. Series of SiN_x films grown at increasing SiH_4 flow with N_2 delivered by plasma source at 500W plasma power (WNS-09 to WNS-12)
2. SiN_x films grown at varying SiH_4 flow fraction with N_2 delivered by dispersion ring at 500W plasma power (WNS-13 to WNS-19)
3. SiN_x films grown at constant gas flows, varying plasma power from 300-500W, N_2 delivered by plasma source (WPS-21 to WPS-23)
4. SiN_x films grown with N_2 delivered through plasma torch at 300W plasma power (WNS-27 to WNS-30)

Directions taken in the modification of the growth parameters were based on the results of ellipsometric characterization of each round of films.

6.1 Ellipsometric Characterization

SiN_x films produced for this study were characterized using the Woollam M-2000U VASE system (with NIR option). Data were collected over 676 wavelengths from 245-1690nm (0.735-5.038eV) at 5 angles (55°, 60°, 65°, 70°, 75°) using a 5-second acquisition time. Samples were stabilized by the in-stage vacuum system during acquisition. The samples were dusted with high-pressure N_2 gas prior to measurement to avoid the effects of contaminant particles. It was intended to quantify the thickness and refractive index of the deposited films while also gaining qualitative data regarding their dielectric properties.

The bandgap of amorphous PECVD SiN_x:H can be expected to range between 1.1eV (amorphous Si) and 4.4eV (stoichiometric Si_3N_4). This means that the onset of bandgap absorption occurs within the energy region measured by the VASE system and necessitates accounting for absorption in the modelling of the data. The Tauc-Lorentz ellipsometric model, used for weakly absorbing materials near their absorption bandgap, has been found effective in the parameterization of PECVD-grown SiN_x films [92] and is used here. The onset of bandgap-related absorption in the SiN_x films was generally observed to occur between 2 and 2.5eV (Figure 6.1).

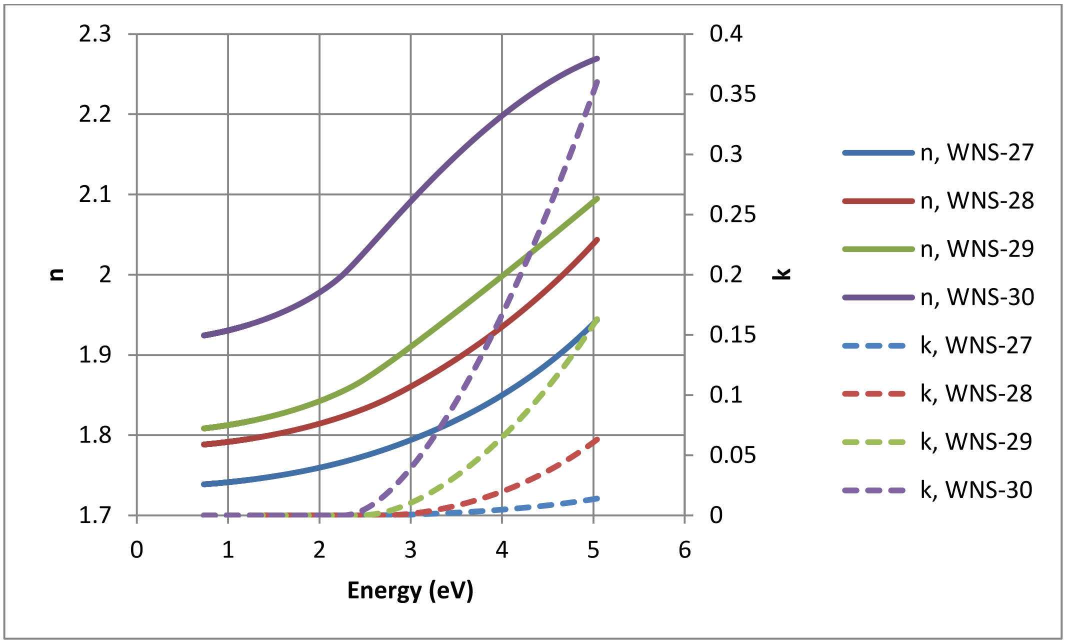

Figure 6.1: Optical constants of WNS-27 to -30 vs. photon energy

A three-layer model (c-Si substrate, Tauc-Lorentz nitride film, surface roughness layer) was able to produce fits to the ψ and Δ spectra of SiN_x films with MSE<12 in all cases, enabling the estimation of thickness and refractive index. Thickness data are presented here as growth rates, since optimizing growth rate was the purpose of this study on the nitride films. To compare the films, we define a SiH_4 flow fraction *R*

$$R_{SiH_4} = \frac{SiH_4(sccm)}{SiH_4 + N_2(sccm)} \tag{6.1}$$

Flow rate fraction is used rather than partial pressure fraction because the limits of the ICP-CVD’s diffusion pump lead to partial pressure being non-linear with flow rate above about 30sccm/2.5 mTorr. The fraction excludes Ar flow, which is not assumed to contribute directly to growth.

Table 6.2: Growth rate and refractive index of SiN_x films

Sample	N_2 source	SiH_4 flow (sccm)	Flow fraction SiH_4	Plasma power (W)	Growth temp (°C)	Growth rate (Å/min)	n @ 632.8 nm
WNS-09	Plasma	3	0.50	500	187	33.7±0.3	2.239
WNS-10	Plasma	3	0.38	500	187	34.7±0.2	2.072
WNS-11	Plasma	3	0.09	500	187	37.5±0.3	1.789
WNS-12	Plasma	4.5	0.13	500	187	59.1±0.7	1.761
WNS-13	Ring	3	0.23	500	187	25.8±0.3	2.273
WNS-15	Ring	4.5	0.31	500	187	35.2±0.4	2.733
WNS-18	Ring	3	0.13	500	187	26.6±0.3	2.055
WNS-19	Ring	2.4	0.10	500	187	25.6±0.3	1.881
WPS-21	Plasma	4.5	0.13	500	253	53.7±0.5	1.807
WPS-22	Plasma	4.5	0.13	400	253	49.2±0.4	1.833
WPS-23	Plasma	4.5	0.13	300	253	50.4±0.4	1.833
WNS-27	Plasma	4.5	0.13	300	187	60.5±0.5	1.758
WNS-28	Plasma	5.4	0.17	300	187	60.7±0.5	1.813
WNS-29	Plasma	6	0.19	300	187	67.8±0.6	1.841
WNS-30	Plasma	6.6	0.22	300	187	65.2±0.6	1.975

In general, for all of the SiN_x films deposited, the refractive index was found to be strongly dependent on the SiH_4 flow fraction while the growth rate was strongly impacted by SiH_4 flow rate. N availability plays a secondary role in determining growth rate (notice the small increase in growth rate from WNS-09 to WNS-12 despite much lower SiH_4 fraction/higher total flow). This indicates that stoichiometric and Si-rich films have comparable rates of growth provided sufficient Si is available for film formation. The refractive index of the films reached a minimum near 1.75 for nitrides grown in N_2 plasma; for those grown in Ar plasma with N_2 introduced through the dispersion ring the minimum was closer to 1.88. In both cases the minimum refractive index was obtained near R =

0.1, and the index trended upward with increasing *R* (Figure 6.2). It is possible that nitrides with N_2 introduced through the dispersion ring could be grown with lower index by further decreasing *R*, but the deposition rate would be quite low.

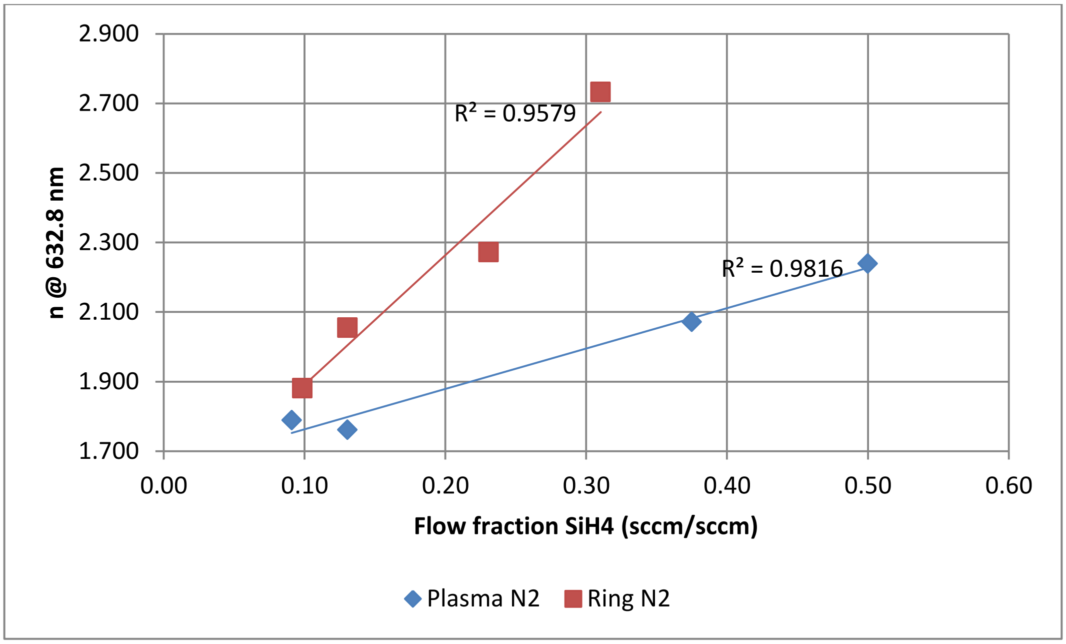

Figure 6.2: Refractive index of WNS-09 to WNS-19 vs. SiH_4 flow fraction

The results of a comparison of ring-N_2 and plasma-N_2 SiN_x films indicated superior N_2 incorporation for the N_2 plasma case, enabling the growth of near-stoichiometric nitrides at a higher rate. It was therefore decided to focus on plasma-N_2 nitrides in the search for a growth-rate optimized deposition recipe. A study of growths at varying plasma power was attempted (WPS-21 to -23), but little variation in refractive index or growth rate was observed (Table 6.2). Accordingly, it was decided to study the effects of small variations in *R* on the growths while keeping total flow (SiH_4+N_2) constant (WNS-27 to -30).

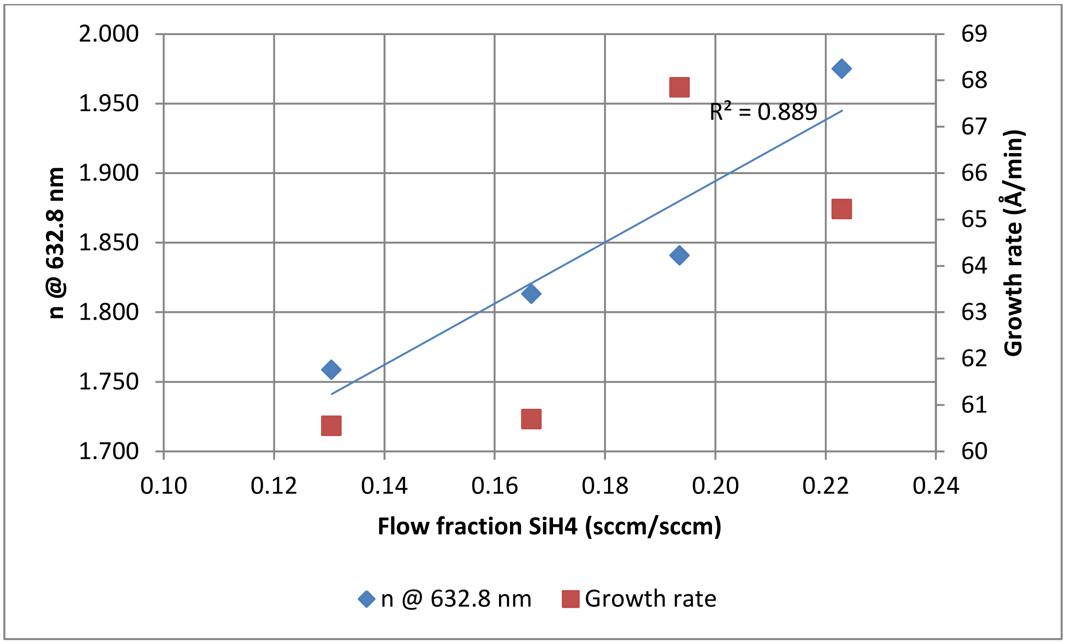

Figure 6.3: Index and growth rate of SiN_x films WNS-27 to WNS-30

Increasing SiH_4 flow fraction from ~0.13 to ~0.22 led to a corresponding increase in refractive index, indicating the production of slightly Si-rich films. A spike in growth rate was observed around *R*=0.2, which is a 1:4 ratio of SiH_4 to N_2. Assuming the film is not significantly Si-rich (a reasonable assumption given the refractive index was around 1.9), this indicates that N_2 activation is much more difficult than SiH_4 activation which leads to the requirement of more N_2 to ensure rapid growth. At this point it was decided that the growth rate of the near-stoichiometric SiN_x films had been sufficiently optimized.

7 Silicon Carbide (SiC_x) Films

It was expected that of the available films on the PECVD systems (Si, SiO_x, SiN_x, SiC_x, combinations, and doped materials), SiC_x films would have the best mechanical properties. It was decided to produce “thin” SiC_x films of varied composition to relate composition with optical properties as well as some “thick” SiC_x films at approximately 4:1 CH_4:SiH_4 gas ratio. This gas ratio was chosen based on the study of the SiN_x films as well as studies on SiC_x films grown by RF-PECVD to yield approximately stoichiometric SiC_x [11]. The “thin” films were deposited on 2” n-Si <100> wafers and glassy carbon plates, while the “thick” films were deposited on 2” undoped Si <100> wafers and cut glass microscope slides. Lessons learned with regards to adhesion from the SiAlO films led to the development of an improved surface cleaning procedure for this study. For films used in mechanical characterization, the following steps were taken to prepare the wafers’ surface for film deposition:

1. Maximum 1 week prior to deposition, RCA-1 clean
2. Store under HEPA filter in clean glass container
3. Immediately prior to loading, UV ozone for 10 min
4. Strip native oxide (60s in buffered HF)
5. Transfer to load lock via clean N_2-filled Ziploc bag
6. Overnight degas in chamber at 700°C heater temperature
7. Immediately prior to deposition, 20min Ar plasma activation at 800W

Modified deposition parameters investigated during the study on SiN_x films were used. The heater temperature was 700°C (corresponding to 253°C substrate temperature) and plasma power was 300W. Due to a chamber ion gauge failure in the ICP-CVD, the chamber base pressure could only be roughly estimated at $3.0 \pm 0.5 * 10^{-6}$ Torr (based on the reading of the ion gauge in the load lock).

Unfortunately, the ICP-CVD suffered a failure of the plasma ignition system shortly after production of the first thick SiC_x film. It was therefore necessary to move to the Group IV-McMaster ECR-PECVD and grow another set of thin SiC_x films for calibrating composition as well as more thick SiC_x films. The second set of films was grown on the ECR-PECVD at 700°C heater temperature, 500W forward power, and base pressure of $7.6 * 10^{-7}$ to $6.4 * 10^{-6}$ Torr.

Table 7.1: SiC films deposited with ICP-CVD and ECR-PECVD

Sample	Date	System	Gas flow (sccm)			Partial pressure (mTorr)				Run time (min)
			Ar	SiH_4 in Ar	CH_4	Ar	SiH_4 in Ar	CH_4	Total	
WNS-32	10-Nov	ICP	14	23	0	1.2	2.1	0	3.3	60
WNS-33	10-Nov	ICP	14	18	5	1.2	1.65	0.45	3.3	60
WNS-34	11-Nov	ICP	14	14	9	1.2	1.55	0.6	3.35	60
WNS-35	11-Nov	ICP	14	9	15	1.2	1.25	0.85	3.3	60
WNS-36	12-Nov	ICP	15	4.5	20	1.25	0.85	1.35	3.45	60
WNS-37	12-Nov	ICP	17	0	23	1.45	0	1.85	3.3	60
WUD-38	13-Nov	ICP	16	9.4	14	1.35	1.1	0.75	3.2	524
WNS-39	15-Nov	ECR	40	40	0	4.1	3.6	0	7.4	30
WUD-40	16-Nov	ECR	40	16	24	4.2	1.4	2.1	7.4	600
WNS-41	17-Nov	ECR	40	16	24	4.1	1.3	2.1	7.3	30
WNS-42	17-Nov	ECR	40	25	15	4.1	2.3	1.1	7.4	30
WNS-43	17-Nov	ECR	40	30	9	4.1	2.7	0.6	7.4	30
WUD-44	18-Nov	ECR	40	16	24	4.1	1.4	1.9	7.4	600

7.1 Ellipsometric Characterization

SiC_x films produced for this study were characterized using the Woollam M-2000U VASE system (with NIR option). Data were collected over 676 wavelengths from 245-1690nm (0.735-5.038eV) at 3 angles (48°, 60°, 72°) using a 5-second acquisition time. Samples were stabilized by the in-stage vacuum system during acquisition. The samples were dusted with high-pressure N_2 gas prior to measurement to avoid the effects of contaminant particles. It was intended to quantify the thickness and refractive index of the deposited films while also gaining qualitative data regarding their dielectric properties.

The bandgap of amorphous SiC_x films such as those produced in this study can be expected to range between 1.1eV (the bandgap of crystalline Si) and 3.2eV (the bandgap of 4H-SiC). This puts the bandgap well within the measured energy range and necessitates accounting for it in the modelling of the data. The Tauc-Lorentz oscillator model is commonly used for describing the optical functions of amorphous dielectric films [93]. Unlike the Cauchy model, it explicitly accounts for the onset of absorption at the material's bandgap energy. For SiC films deposited at a 4:1 CH_4:SiH_4 flow ratio (CH_4 flow fraction of 0.8), this seems to occur around 2.2 eV (Figure 7.1).

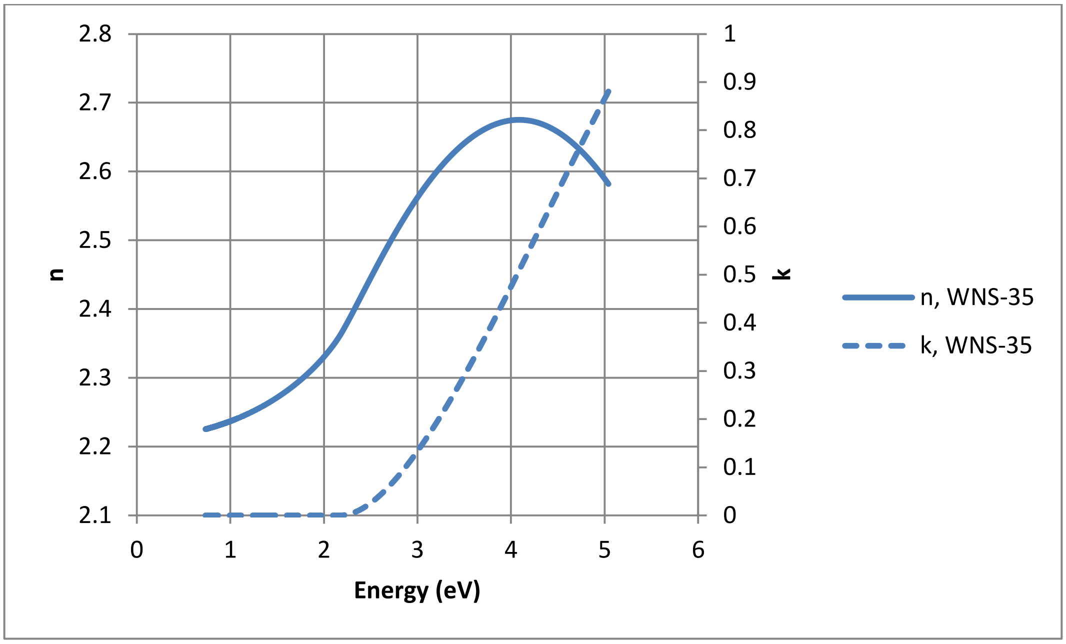

Figure 7.1: Optical constants of SiC_x film WNS-35 vs. photon energy

A three-layer optical model consisting of the *c*-Si substrate, Tauc-Lorentz carbide film, and surface roughness layer produced fits for all of the thin SiC_x films with MSE<10 (Table 7.2).

Table 7.2: Thickness, refractive index, and growth rate of thin SiC_x films

Sample	Reactor	Flow fraction CH_4	Thickness (Å)	n @ 632.8 nm	Run time (min)	Growth rate (Å/min)
WNS-33	ICP	0.48	2226±0.5	3.167	60	37.1±0.2
WNS-34	ICP	0.68	1665.6±0.3	2.887	60	27.8±0.1
WNS-35	ICP	0.85	1267±0.2	2.312	60	21.1±0.1
WNS-36	ICP	0.94	742.7±0.2	2.221	60	12.4±0.1
WNS-37	ICP	1	26.2±0.1	1.959	60	0.4±0
WNS-41	ECR	0.83	721.4±0.1	2.781	30	24±0.1
WNS-42	ECR	0.67	1367.2±0.2	3.152	30	45.6±0.4
WNS-43	ECR	0.5	2157.2±0.8	3.562	30	71.9±0.6

Modelling of the amorphous silicon films WNS-32 and WNS-39 was unsuccessful due to the lack of index contrast with the Si wafer substrate. The model indicated the presence of a very thin (~26Å) film for the deposition with only CH_4 flow (WNS-37), which is presumably *a*-C:H. Films are listed with their CH_4 flow rate fraction

$$R_{CH_4} = \frac{CH_4(sccm)}{CH_4 + SiH_4(sccm)} \tag{7.1}$$

As was stated earlier, flow rate fraction is used rather than partial pressure fraction because partial pressure on the ICP system is non-linear with flow rate above ~3mTorr due to the limits of the chamber's diffusion pump. Refractive index of the films decreasing with increasing R (Figure 7.2)

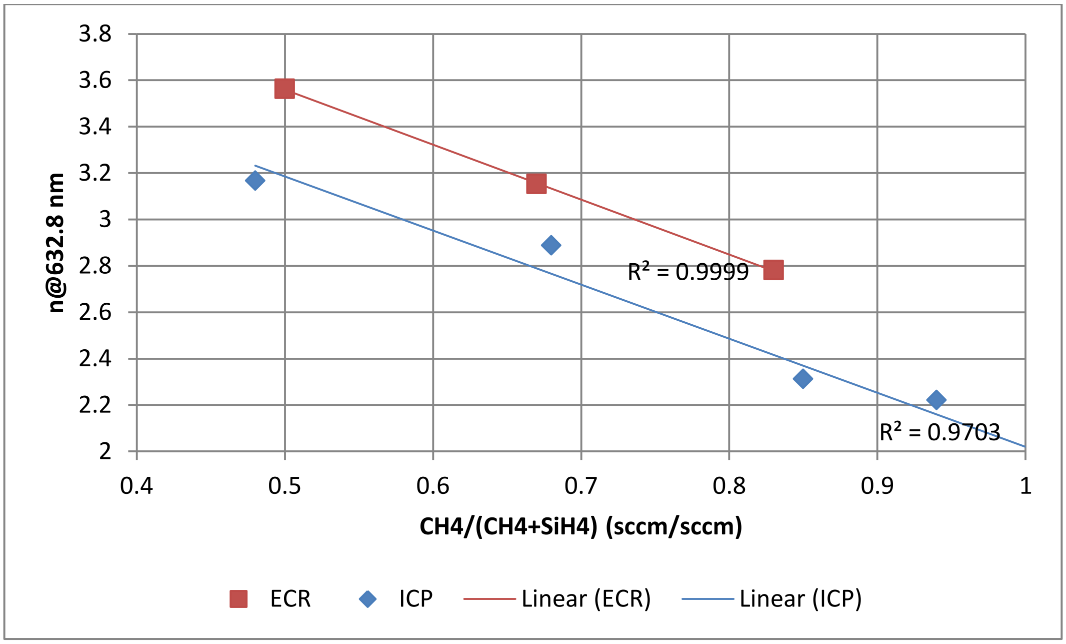

Figure 7.2: Effect of CH_4 flow fraction on refractive index of SiC_x films

Overall, the ICP-grown films had lower refractive index than ECR-grown ones. This could be due to increased C incorporation because of higher electron temperature, or it could be related to porosity or H incorporation. Film growth rate decreased with increasing flow CH_4 fraction (Figure 7.3).

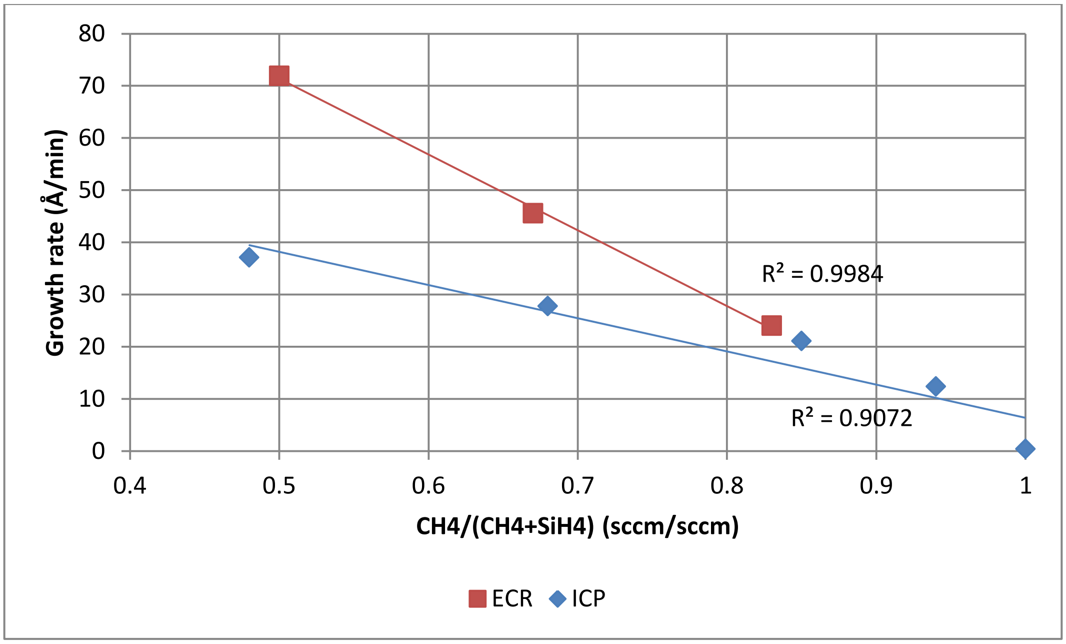

Figure 7.3: Effect of CH_4 flow fraction on growth rate of SiC_x films

The decreased growth rate may indicate that growth of *a*-Si phases is energetically favoured in comparison with SiC phases. Another strong possibility is that the decreased growth rate is related to the Ar fraction in the gas mixture (because SiH_4 is delivered as a 30% mixture in Ar). Reduced Ar fraction would likely reduce the electron temperature of the plasma and thereby slow growth. It was not possible to isolate the effects of Ar flow from those of CH_4 flow within this study; doing so would require the growth of a new set of films. Plotting growth rate against the Ar flow fraction displayed a positive trend, just like plotting against the CH_4 flow fraction (Figure 7.4).

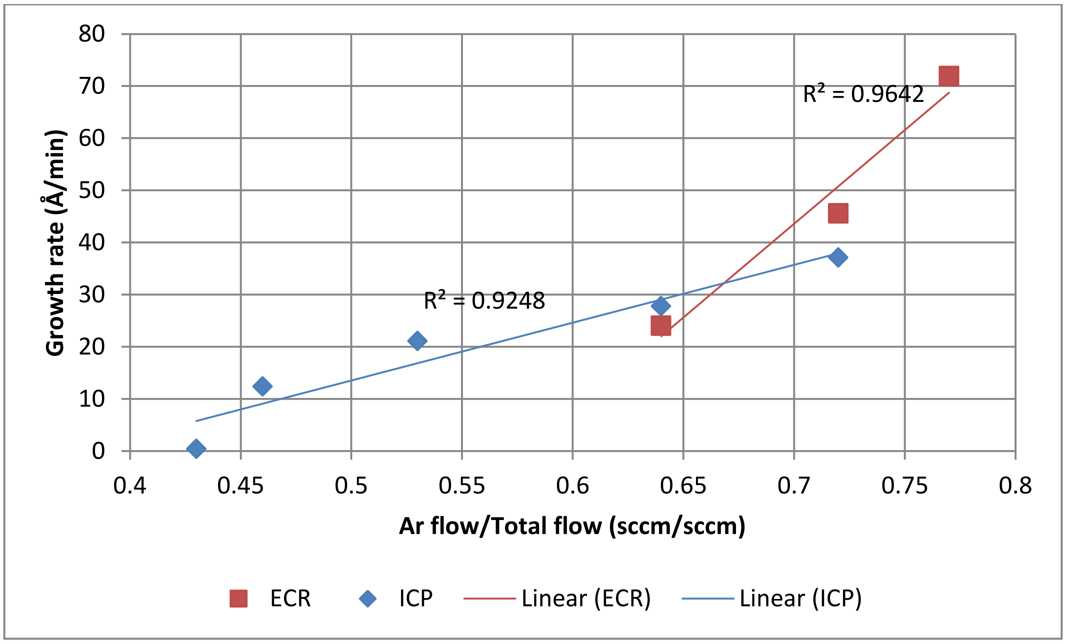

Figure 7.4: Effect of Ar flow fraction on growth rate of SiC_x films

In applying the Tauc-Lorentz model to the thicker SiC_x films it was necessary to restrict fitting to the range 1.378-3.351eV. Thickness determination was not as precise with MSE in the 25-40 range (Table 7.3). This may indicate that the Tauc-Lorentz model is not entirely sufficient for this application.

Table 7.3: Thickness, refractive index, and growth rate of thick SiC_x films.

Sample	Reactor	Flow fraction CH4	Thickness (Å)	n @ 632.8 nm	Run time (min)	Growth rate (Å/min)
WUD-38	ICP	0.83	9320±10	2.403	524	17.8±0.1
WUD-40	ECR	0.83	22600±30	2.526	600	37.7±0.4
WUD-44	ECR	0.83	21140±30	2.569	600	35.2±0.3

7.2 Rutherford Backscattering Spectrometry

In the interest of determining the composition of the thin SiC_x films, each deposition was conducted on a 1 cm^2 glassy C plate in addition to the Si wafer. The series of 6 films from the ICP (PCG-32 to PCG-37) as well as the series of 4 films from the ECR (PCG-39 and PCG-41 to -43) were measured using RBS at the Western University's Tandetron facility. All samples were dosed with 4 μC of He^+ ions at 1.8 MeV. Rather than attempt a channeled measurement, random rotation of the sample was used. An evolution in the shape of the measured spectra was observed for increasing CH_4 flow fraction R.

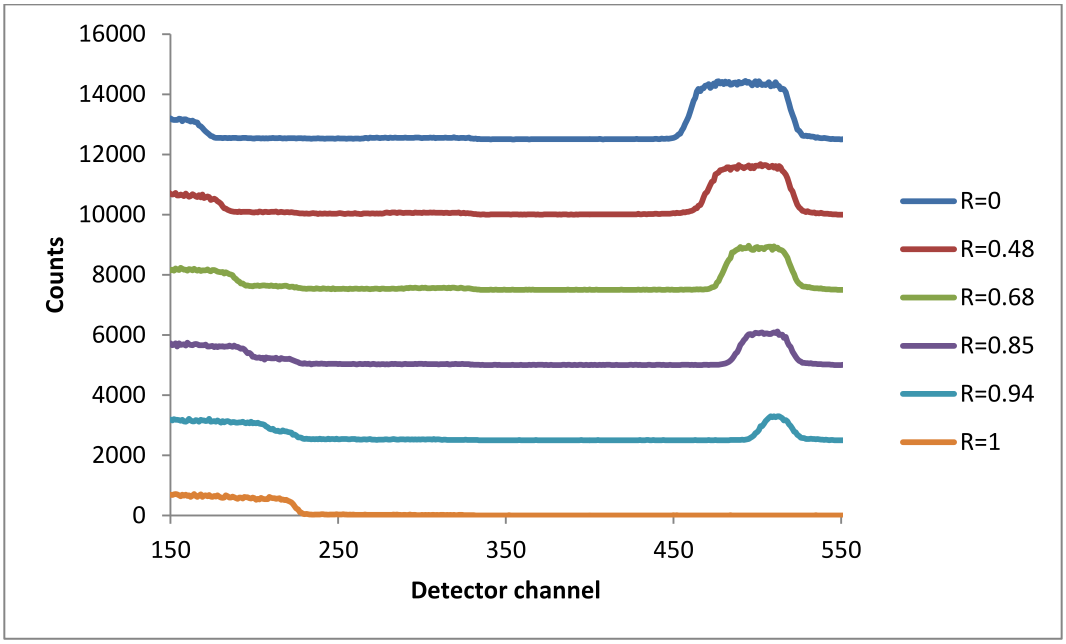

Figure 7.5: RBS spectra of ICP-CVD SiC_x films with varied CH_4 flow fraction

The 4 ECR films exhibit a similar evolution in spectrum shape, but the effect is less noticeable because they are thinner. Films deposited at *R*=0 (no CH_4 flow) exhibit a strong Si peak (around channel 500) which decreases in height as

R is increased, indicating reduced Si incorporation. The Si peak also narrows due to the lower deposition rate and thickness observed for SiC_x films at higher *R*. As the Si peak diminishes, a rising C shoulder from the films is observed (around channel 200, separate from the substrate rise). The substrate rise shifts to higher energy, from channel ~175 to ~225, as *R* increases. This is because films with higher R values are thinner, which means ions recoiling from the substrate travel through less film to reach the detector. Quantification of the observed spectra revealed, as expected, decreasing Si content and increasing C content for higher R values.

Table 7.4: Estimated composition (neglecting H) of SiC_x films

Sample	Reactor	Flow fraction CH_4	C (at%)	N (at%)	O (at%)	Si (at%)
PCG-32	ICP	0	8±1	5±1	7±1	80±2
PCG-33	ICP	0.48	21±1	5±1	8±1	66±2
PCG-34	ICP	0.68	30±1	5±1	8±1	57±2
PCG-35	ICP	0.85	48±1	6±1	4±1	42±1
PCG-36	ICP	0.94	60±2	6±1	2±1	32±1
PCG-39	ECR	0	9±1	2±1	1±1	88±3
PCG-41	ECR	0.83	44±1	7±1	3±1	46±1
PCG-42	ECR	0.67	24±1	7±1	0±1	69±2
PCG-43	ECR	0.5	19±1	4±1	1±1	76±2

Even *a*-Si films deposited at *R*=0 (PCG-32 and -39) showed evidence of C incorporation. It is possible that the C comes from pump oil being broken down by the plasma during the growth process. As one might expect from any vacuum chamber, there is also some O incorporation (likely from water vapour) and N incorporation (from atmosphere). ICP-deposited films exhibited more O incorporation than ECR-deposited ones. The two systems use different Ar sources and O contamination of the ICP Ar source may be to blame. The thicker SiC_x films (WUD-38,-40,-44) would be expected to contain less O and N than these thin films because of the overnight degas cycle employed in their growth.

Plotting the fractional C content of the deposited SiC_x films against the CH_4 flow fraction reveals exponential trends both deposition systems (Figure 7.6).

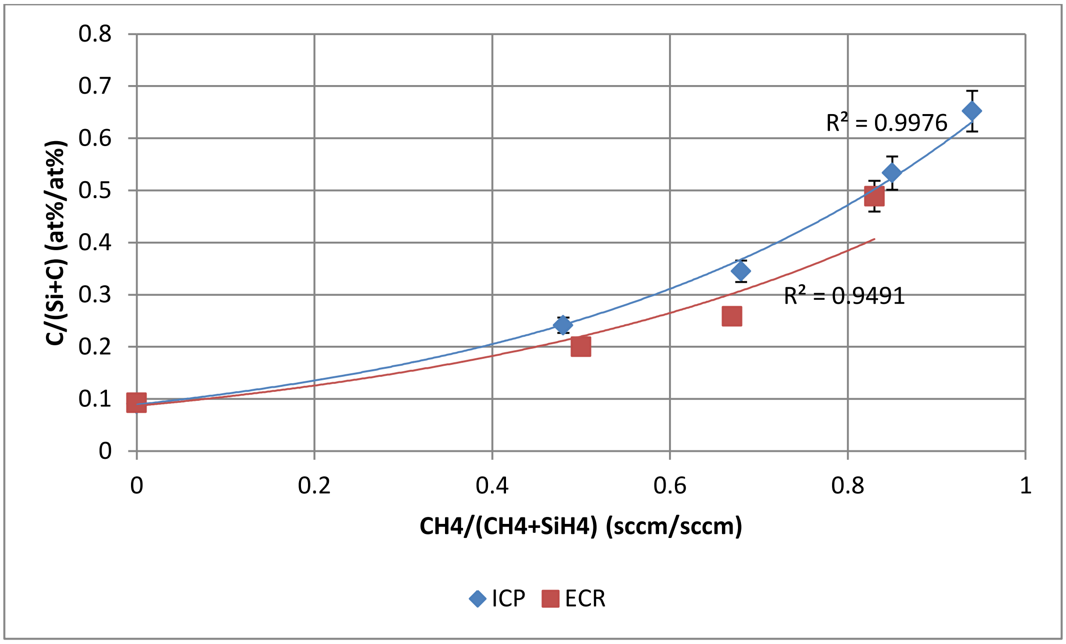

Figure 7.6: C fraction of SiC_x films vs. CH_4 flow fraction

As expected, CH_4 flow fractions of 0.8 led to the production of approximately stoichiometric carbides. This has previously been observed for SiC_x films deposited by RF-PECVD [11].

7.3 Annealing Behaviour

It was expected that annealing the SiC_x films at higher temperatures (600°C and higher) would drive off the H incorporated during deposition and increase film porosity, with implications for the mechanical properties of the films. Small pieces of sample WUD-40 were annealed for 1h under flowing N_2 gas in a tube furnace at temperatures from 400 to 1100°C. Changes in the appearance of the film were observed starting at 500°C. Samples WUD38 and WUD-44 were annealed under the same conditions at 400, 500, and 600°C. WUD-40 and WUD-44 pieces annealed above 400°C were examined under an optical microscope, revealing cracking (Figure 7.7).

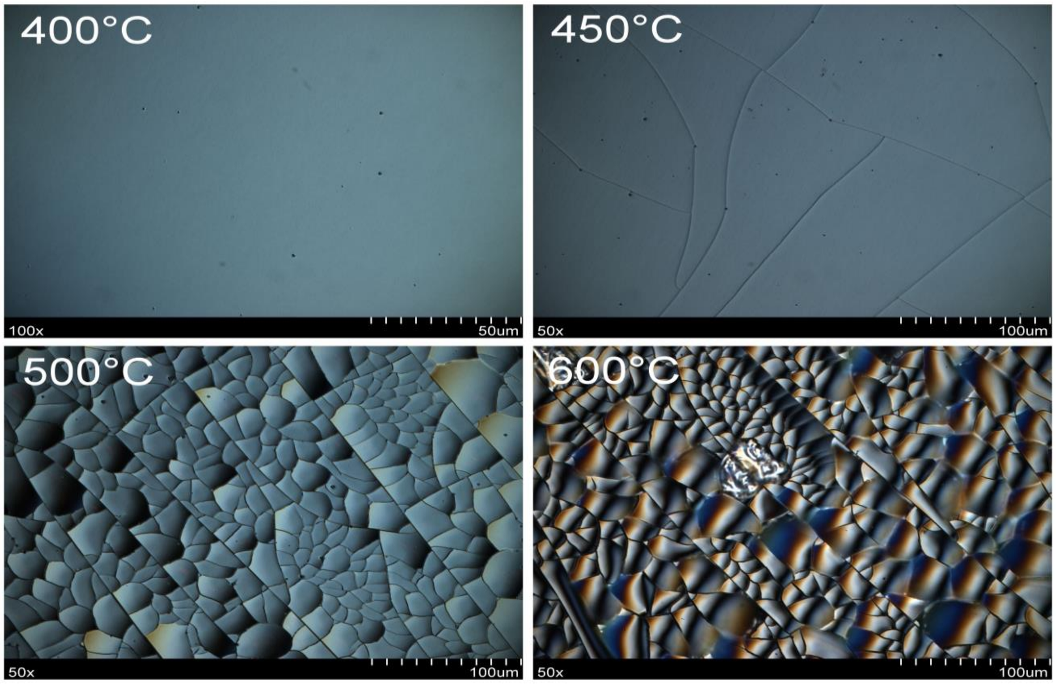

Figure 7.7: Optical micrographs of SiC_x film WUD-40 after annealing

The WUD-38 pieces, by contrast, exhibited no cracking for annealing temperatures up to 600°C. WUD-38 was thinner than WUD-40 and WUD-44 (~930nm vs. ~2.1μm); thinner films generally have lower internal stress and therefore are better able to survive annealing. Another possibility is that the lower deposition rate of WUD-38 caused lower H incorporation compared with the ECR films. The release of bonded H during high-temperature annealing has been known to lead to massive (~2 GPa) increase in the tensile stress of PECVD silicon nitride films and commonly causes them to fail [94]; one might expect a similar effect for the carbides.

The cracks, which begin to form around 450°C, appear to propagate from the "bubble" defects observed in the films; this is not surprising as one would expect high stress concentrations around the area of these voids. It is possible that if the bubble defects (which were also observed in the SiAlO films) could be eliminated, high-temperature annealing of the thick SiC_x films would become feasible. High-temperature annealing is expected to lead to densification of the films and improved mechanical properties, so this might be an avenue worth pursuing.

7.4 Nanoindentation Results

It was desired to determine the hardness and reduced modulus of the SiC_x films and thereby compare films from the ICP and ECR systems and examine the effect of N_2 annealing. The films were characterized using nanoindentation on the Hysitron TriboIndenter at Université de Montreal. Two sets of 25 indentations with a Berkovich diamond were performed on each film at loads ranging from 0.1 to 10mN. Examining stiffness and penetration depth at a range of loads provides information that enables the extraction of film-only mechanical properties from the measured properties which are actually composite properties of the film-substrate system. The three thick SiC_x depositions were performed on Si wafers (WUD-38,-40,-44) as well as glass microscope slides (SGS-38,-40,-44); indentation studies were made on films on both substrates so that substrate effects can be examined.

7.4.1 Reduced Modulus

The reduced modulus E_r measured for a thin film on a substrate will be equal to the film-only modulus at a contact depth h_c=0, trending smoothly toward the substrate modulus with increasing indentation depths. Ideally one would make only very shallow indentations to minimize the substrate influence, but due to limitations in the accuracy of load and displacement measurements this is not always possible. A superior technique is to determine the trend in the measured E_r with depth and extrapolate this depth to h_c=0. For maximum indentation depth

h_c less than 15% of the film thickness t, it is sufficient to use a linear function for the extrapolation of the E_r data to h_c=0 [86].

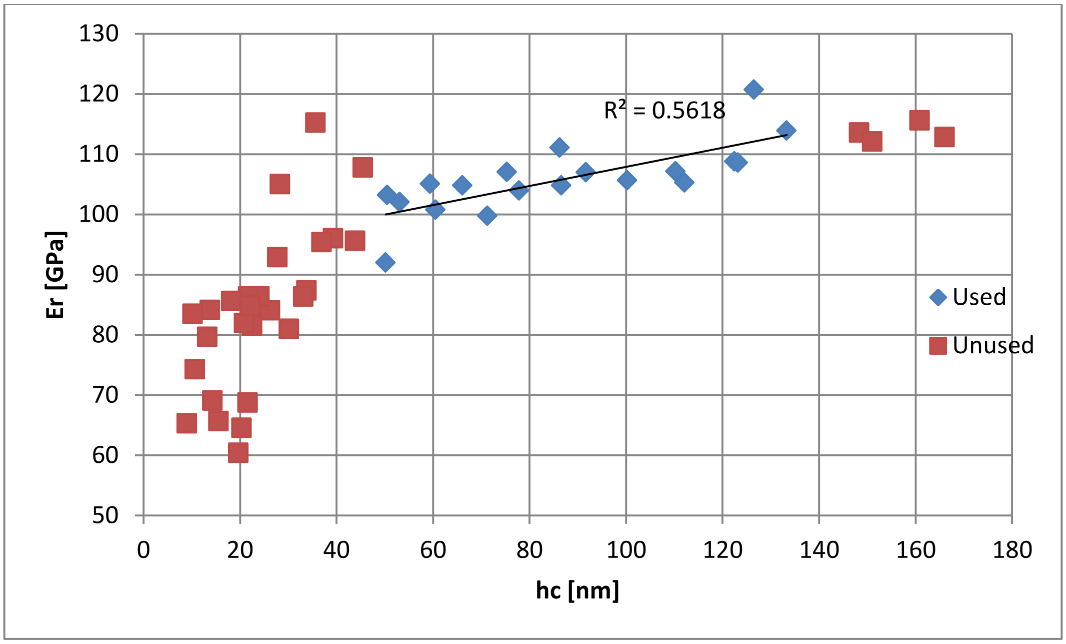

Figure 7.8: Measured elastic modulus vs. depth for film WUD-38-600N_2

Notable in Figure 7.8 is the sharp increase in measured E_r in the region with h_c<50nm. This rising trend is caused by the non-ideal shape of real Berkovich diamond indenters, which generally will have a finite tip radius of at least 50nm [83]. Because the area function used to estimate contact stiffness (and thereby elastic modulus) assumes an infinitely sharp tip, data taken at h_c<50nm will tend to be underestimates of the true E_r. We can therefore determine E_r for all of the SiC_x films by confining our linear fit to the region 50nm<h_c<0.15t and extrapolating this line to h_c=0. Results of the fitting are given in Table 7.5.Table 7.5Table 7.5: Estimated reduced modulus of SiC_x films

Sample	Substrate	Reactor	Thickness [Å]	Er [GPa]
SGS-38	Glass	ICP	9320±10	77±9
SGS-40	Glass	ECR	22600±30	87±3
SGS-44	Glass	ECR	21140±30	82±2
WUD-38-AD	Si	ICP	9320±10	74±7
WUD-38-400N2	Si	ICP	9320±10	83±11
WUD-38-600N2	Si	ICP	9320±10	92±3

From the E_r data in Table 7.5, it is noticeable that E_r estimated using this technique agrees within uncertainty for WUD-38-AD and SGS-38. These films were deposited in the same run and neither received thermal treatment; one would expect the same E_r for the two. This indicates that the data selection and extrapolation technique is effective in eliminating substrate influence on E_r. The higher E_r values observed for the ECR-deposited SiC_x films may indicate higher density compared to the ICP-deposited films, which is also observable in the refractive index measured by VASE (Table 7.3). For the WUD-38 films, E_r improves with increased annealing temperature; this indicates that the positive effects of annealing on film quality (densification) outweigh the negative effects (increased porosity and tensile stress). Finally, it is worth noting that the measured E_r values for all SiC_x films are superior to those reported in [54] for RF-PECVD films, which can be attributed to the comparatively lower growth rate and higher plasma density of the ECR and ICP systems.

7.4.2 Hardness

In general, substrate influence on the hardness measured for the film-substrate system is generally insignificant for indentation contact depth h_c less than 10% of the film thickness [83]. However, hardness data measured at contact depth h_c<50nm are strongly influenced by the non-ideality of the Berkovich tip as is the case for E_r; additionally, at these low contact depths deformation of the film is mainly elastic and therefore not indicative of the true hardness [83].

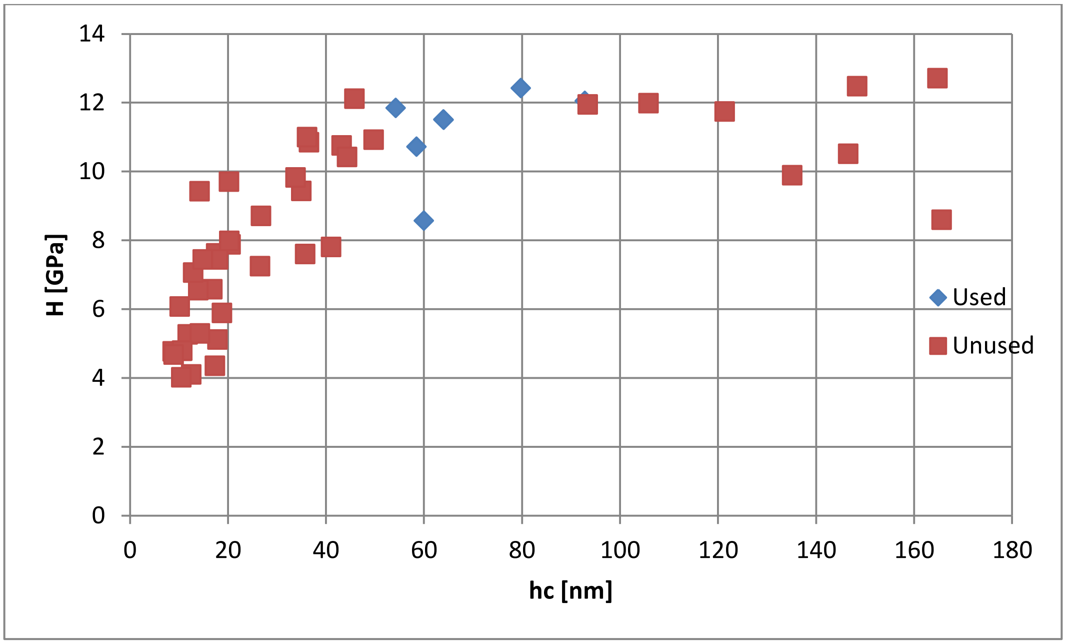

Figure 7.9: Measured hardness vs. depth for WUD-38-400N_2

Ruling out the data deemed inadmissible (h_c<50nm or h_c/t>0.1), the hardness of the SiC_x films can be estimated using the mean of the remaining data with the standard error providing information about the accuracy of the estimate.

Table 7.6: Estimated hardness of SiC_x films

Sample	Substrate	Reactor	Thickness [Å]	H [GPa]
SGS-38	Glass	ICP	9320±10	8.8±0.5
SGS-40	Glass	ECR	22600±30	11.9±0.2
SGS-44	Glass	ECR	21140±30	11.7±0.2
WUD-38-AD	Si	ICP	9320±10	9.9±0.4
WUD-38-400N2	Si	ICP	9320±10	10.9±0.5
WUD-38-600N2	Si	ICP	9320±10	11±0.2

As was the case for E_r, the ECR-deposited films have superior hardness to those produced by ICP; likewise, higher annealing temperature improves the hardness of the films. Again, this is most likely due to higher film density. Unlike the case for E_r, hardness measured for SGS-38 does not agree with that of WUD-38-AD within uncertainty. Since Si is harder than glass, this disagreement can most likely be explained by substrate influence. In comparison with the SiC_x films grown in [54], all films grown in this study exhibited equal or superior hardness. This indicates that the lower growth rate and higher plasma density of the ECR-PECVD and ICP-CVD systems in comparison with the RF-PECVD method used in [54] produce films with superior density and/or lower H incorporation, despite lower deposition temperature and the lack of ion bombardment during growth.

7.5 Scratch Results

Scratch testing was performed on the SiC_x films in the interest of comparing their adhesion and failure mechanisms with those of the SiAlO films studied previously. The tests were performed using the CSM Micro-Combi Tester at the Université de Montreal. While it was desired to use the same test parameters as for the SiAlO films (1-10N load, Al_2O_3 ball tip), initial results indicated that the 3/16" ball indenter was causing cracking within the Si substrate and therefore not producing adhesion information. The flaking effect observed with SiAlO coatings was not present, indicating vastly superior adhesion of the SiC_x films. The indenter type was changed to a 50μm tip radius Rockwell diamond, and three scratches were performed on each SiC_x film at progressive loads of 0-5N over a 1cm scratch track at 10mm/min.

Three critical loads were defined.

1. Load at which the first crack appears in the film
2. Load at which cracking becomes continuous along the scratch track
3. Load at which spallation/chipping is first observed

The appearance of the scratch track at each critical load varied somewhat between films. Many of the films failed by tensile cracking followed by spallation along the sides of the track (Figure 7.10):

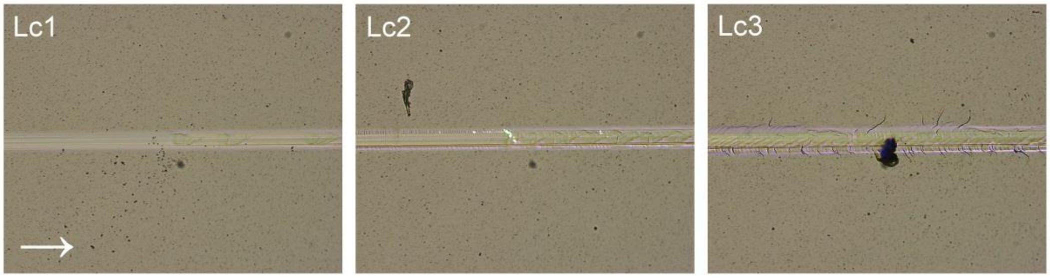

Figure 7.10: Appearance of critical loads 1-3 on sample WUD-38-AD

In other cases the distinctive circular patterns of Hertzian ring cracking were observed, again followed by spallation of the coating (Figure 7.11):

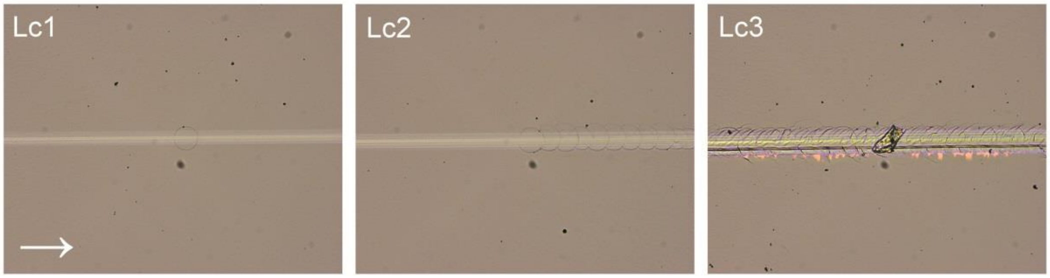

Figure 7.11: Appearance of critical loads 1-3 on sample WUD-44-400N_2

The type of cracking observed prior to failure appeared to be dependent on the temperature at which the film was annealed, with higher anneal temperatures tending to produce Hertzian cracking.

Table 7.7: Scratch test critical loads for six SiC_x films

Sample	Crack type	L_{c1} (N)	L_{c2} (N)	L_{c3} (N)
WUD-38-AD	Tensile	2.2±0.3	2.7±0.1	3.5±0.3
WUD-38-400N2	Tensile	2.3±0.3	2.8±0.1	3.1±0.1
WUD-38-500N2	Hertzian	2±0.2	2.6±0.1	3.7±0.1
WUD-38-600N2	Hertzian	0.6±0.1	2.5±0.5	4.3±0.1
WUD-44-AD	Tensile	2.4±0.1	2.4±0.1	3.4±0.1
WUD-44-400N2	Hertzian	1.1±0.2	1.5±0.1	3.2±0.1

Hertzian cracking is generally indicative of a brittle film, or a brittle film and substrate [90]. The transition of cracking from ductile-tensile to brittle-Hertzian with increasing annealing temperature can be explained by the probable drive-off of H from the films. A drop in the performance of the coatings is observed when comparing as-deposited to 400°C N_2 annealed; this is likely due to an increase in the tensile stress as H starts to evolve from the coating. Higher annealing temperatures tend to increase the resistance of the coatings to spallation (higher L_{c3}). It is also notable that for WUD-38 annealed at 600°C, initial cracking occurred at the very low load of 0.6±0.1N. It is probable that annealing at 600°C leads to increased porosity in the film as H is driven off, causing cracking as voids collapse. But the presence of collapsible voids may also improve the resistance to spallation by providing a means of dissipating strain energy.

Adhesion behaviour at different indenter tip radii was also explored. In general, larger indenter tip radius leads to a less intense stress maximum occurring deeper within the film-substrate system. Coating WUD-38-AD was scratch-tested at three different tip radii. The maximum load for the test was adjusted based on the tip radius, but all tests started at 0N and were 1cm scratches at 10mm/min.

Table 7.8: Scratch test critical loads by tip radius for film WUD-38-AD

Tip radius (μm)	Max load (N)	Mode	L_{c1} (N)	L_{c2} (N)	L_{c3} (N)
50	5	Tensile	2.2±0.3	2.7±0.1	3.5±0.3
100	10	Tensile	5.2±0.8	5.2±0.8	7.1±1
200	30	Hertzian	21.2±1.2	22.2±1.3	Not seen

As expected, the coatings were capable of tolerating much greater loads without cracking or spalling when scratched with a larger radius tip because of lower maximum stress. No spallation at all was observed for scratches with the 200µm Rockwell diamond tip, and the crack type changed from tensile to Hertzian. This almost certainly indicates that the stress maximum for the 200µm tip was located within the brittle Si wafer substrate, and not near the interface. It is nevertheless impressive that the coatings were able to survive loads up to 30N, especially when compared with the performance of the SiAlO films studied previously.

8 Conclusions

8.1 Growth of Wear-Resistant SiAlON Coatings

The coatings produced in this preliminary study did not exhibit significant wear resistance. Wear testing using the pin-on-disk system depends on the coating having sufficient hardness, thickness, and adhesion to avoid complete removal during the test. This usually requires at least 2-3μm of hard coating such as sputtered titanium nitride (TiN). For softer coatings, greater thickness is necessary. The nanoindentation technique for measuring hardness and modulus suffers from reduced accuracy and strong substrate effects for film thicknesses less than about 1μm [86]. Over the course of an 8 hour deposition, the McMaster RPECVD reactors produce about 1 μm (standard recipe) or 2 μm (accelerated recipe) of coating. This does not preclude production of, for instance, a 5μm coating but it does make the process difficult and time-consuming.

The attempt to improve the wear resistance of the thick SiC_x coatings via high-temperature annealing was unsuccessful due to cracking of the films (Section 7.3). Elimination of the “bubble” defects observed in optical micrographs of the coatings (Figure 5.16, Figure 7.7) might enable high-temperature annealing, with corresponding improvement in wear resistance. Of course, the requirement for post-annealing at temperatures 500°C or higher partially negates the advantage of RPECVD as a low-temperature process.

In contrast to previous work on Al-doped SiO_x films produced using the Group IV-McMaster ECR-PECVD system [12], SiAlO films grown in this work were estimated as containing less than 2at% Al. This was ascribed to possible precursor depletion or clogged gas lines. The Al content appeared to have negligible effect on the films' mechanical properties (Figure 5.13, Figure 5.15), which is unsurprising given the low total incorporation.

Energy dispersive X-ray spectroscopy (EDX) was effective in estimating the Al content of SiAlO films. Its advantages compared to the Rutherford backscattering spectroscopy (RBS) technique include the ability to characterize thick (~1μm and up) films and superior distinguishability for Al vs. Si. Disadvantages are the requirement for a thick film and poor precision at low Al content; for example, the Al content of film SiAlO-03T was estimated at 0.6±0.1at% which is a relative standard error of 16.6%.

All of the films with Al incorporation exhibited increased C content compared to films deposited without the Al precursor (Section 5.3). This is consistent with previous work [12]. Based on these results, a SiAlON film grown by the method used here (combined ECR-PECVD and MOCVD) will be a highly complex system with actual chemical formula $SiAl_wO_xN_yC_z$:H and correlation of mechanical or tribological properties with composition becomes extremely difficult.

8.2 Mechanical Characterization of Coatings

In contrast to the difficulties encountered with Al incorporation and the production of wear-resistant coatings, it proved readily possible to measure the mechanical properties of the RPECVD films and perform qualitative adhesion characterization via scratch testing. A film thickness of 1µm is sufficient to provide nanoindentation results given known mechanical properties of the substrate, and a significant enhancement in result quality appears for thicker (2µm) films. SiAlO films produced during this study had similar hardness and modulus (H and E) to thermal SiO_2. The values of H and E measured for the SiC_x films fell within the spectrum for similar films measured in the literature (Table 8.1); as mentioned previously the properties of a thin film are strongly dependent on the method of its growth.

Table 8.1: Comparison of film mechanical properties with literature

Source	Material	Growth method	Growth temp (°C)	E_r (GPa)	H (GPa)
This work	SiAlO:H	ECR-PECVD	137	75±2	8.2±0.4
Matoy et al. [95]	SiO_x:H	RF-PECVD	Not given	68±4	6.2±0.6
Jung et al. [42]	SiO_2	Wet thermal	1100	73±2	11.5±0.2
This work	SiC_x:H	ICP-CVD	253	74±7	9.9±0.4
This work	SiC_x:H	ECR-PECVD	253	87±3	11.9±0.2
Flannery et al. [54]	SiC_x:H	RF-PECVD	300	56±1	8.8±0.6
Porada et. al. [55]	SiC_x:H	RF-PECVD	300	118±2	10±0.5
El Khakani et. al. [25]	SiC_x:H	RF-PECVD	250	162±10	19.2±2

The superior mechanical properties of the a-SiC_x:H films grown in [25] in comparison to the other studies can likely be attributed to the use of a 100kHz RF power supply vs. the standard 13.56MHz. Low-frequency plasma excitation in

RF-PECVD produces higher sheath voltage and stronger ion bombardment; the trade-off is increased compressive stress in the films.

Modified film growth recipes aimed at increasing deposition rate were studied in Chapters 6 and 0 and were successful in this aim. Growth rate was found to be strongly dependent on gas flow, especially SiH_4 flow. By increasing SiH_4 flow three-fold and proportionally increasing the other gas flows, SiC_x films were grown at up to twice the rate of the original SiAlO films despite an increase in the growth temperature from 137°C to 253°C. The development of this “high-speed” recipe significantly eases the process of growing the thick films suitable for mechanical characterization, and it may be possible to further increase growth rates through additional optimization.

The initial attempts at wear testing of the SiAlO films indicated poor adhesion as the likely culprit for their low wear resistance. Accordingly, a thorough surface cleaning procedure (Chapter 0) was developed and followed resulting in greatly improved adhesion as indicated by the scratch testing results of Section 7.5. The SiC_x films survived scratching at loads of up to 30N with a Rockwell C diamond indenter, exhibiting some cracking but no spalling or delamination.

9 Suggestions for Future Study

9.1 Wear-Resistant Coatings

While the first round of SiAlO films were undergoing mechanical testing at Université de Montreal, it was suggested to the author by Dr. Jolanta-Ewa Klemberg-Sapieha that mechanical properties of the coatings could be improved by having them subjected to plasma bombardment during growth. The ICP and Group IV-McMaster ECR-PECVD reactors were purposefully designed to avoid this since it is deleterious to electrical properties. It is possible that controllable ion bombardment could be introduced with the addition of a second (bias) power supply to the reactor designs (in the current design, the substrate is grounded). This bias supply would not need to be exceptionally powerful (50-150W), and could be a low-frequency (kHz range) type. Of course, any such design change would require installation of new electrical feedthroughs in the reactors.

Difficulties were encountered with generating significant (more than a few at%) Al incorporation in SiAlO films using the solid metalorganic precursor method without accompanying C contamination. Possibly, Al incorporation could be improved by the use of a gaseous precursor such as trimethylaluminium (TMA), but such gases are extremely hazardous and could likely still introduce C contamination. A more attractive alternative, suggested by Dr. Jacek Wojcik, is the addition of sputtering capability to the system for Al and rare-earth metals.

9.2 Mechanical Characterization of Coatings

To get a better estimate of the accuracy of the Hysitron indenter used for *H* and *E* determination in this study, it might be worthwhile to perform reference indentations on bare substrates such as Si wafers and glass slides as well as thermal SiO_2 and reference SiO_x:H films produced by the McMaster reactors. This would also provide a basis for direct comparison to the *H* and *E* data measured on the SiAlO films. Measurements on other coating systems from the PECVD reactors (*a*-Si:H, SiO_x:H, SiO_xN_y:H, SiN_x:H, SiC_xN_y:H, etc.) would of course also be of interest, as would more thorough characterization of thermally-treated coatings.

Scratch testing is generally considered to be only a quantitative measure of adhesion when one considers only the critical loads. Nevertheless, the magnitude of the critical loads enables comparison between different coatings provided consistent test methodology is used. A consistent methodology was not implemented in this study due to the widely disparate adhesion observed for the SiC_x films in comparison to the original SiAlO films, but the standardization of a surface cleaning procedure for Si wafers should ensure consistency in any future studies of scratch adhesion. It would also be informative to investigate the adhesion of the RPECVD coatings to other substrates such as steel or float glass.

The surface cleaning procedure developed uses an argon (Ar) plasma surface activation step immediately prior to deposition. Because ion bombardment of the substrate is not a feature of the McMaster RPECVD systems, the effect of this step is likely to be minimal since sputter cleaning will not occur. Several papers published in the early 1990s observed efficient surface cleaning by hydrogen (H) plasma produced by an ECR source even in the absence of any substrate bias [96], [97], [98]. Furthermore, this ECR hydrogen plasma was observed to etch thermal oxides and strip silicon native oxides over the course of 10-20 minutes. This opens up the attractive possibility of stripping wafer native oxide directly in the growth chamber. The current surface cleaning procedure strips the oxide with an HF dip, but during the process of sample transfer to the growth chamber in an N_2-filled Ziploc bag one would expect the introduction of significant organic contaminants to the wafer surface. An H_2 plasma oxide strip, if feasible, would eliminate this possibility and likely lead to improved adhesion.

During the course of this work, it was intended by the author to perform internal stress characterization of the SiN_x and SiC_x coatings. Stress measurements were performed using a Tencor FLX-2320 laser curvature measurement system in the CEDT cleanroom. Unfortunately, due to a failure of one of the lasers these measurements were later discovered to be invalidated and sufficient time was not available to repeat them. Knowledge of the films' internal stress would be very helpful in the design of MEMS devices using the films.

10 References

[1] R. P. Walsh, L. T. Summers, and J. R. Miller, “The 4 K tensile and fracture toughness properties of a modified 316LN conduit alloy,” *Proc. ICEC/ICMC*, vol. 96, 1891.

[2] W. D. Nix, “Mechanical properties of thin films,” *MTA*, vol. 20, no. 11, pp. 2217–2245, Nov. 1989.

[3] J. D. Plummer, *Silicon VLSI technology: fundamentals, practice, and modeling*. Upper Saddle River, NJ: Prentice Hall, 2000.

[4] Institute of Electrical and Electronics Engineers, *Micromechanics and MEMS: classic and seminal papers to 1990*. New York: IEEE Press, 1997.

[5] K. E. Petersen, “Silicon as a mechanical material,” *Proceedings of the IEEE*, vol. 70, no. 5, pp. 420–457, 1982.

[6] H. Hertz, “On the contact of elastic solids,” *J. reine angew. Math*, vol. 92, no. 156–171, p. 110, 1881.

[7] K. G. Budinski, *Surface engineering for wear resistance*. Englewood Cliffs, N.J: Prentice Hall, 1988.

[8] K.-H. Zum Gahr, *Microstructure and wear of materials*, vol. 10. North Holland, 1987.

[9] G. G. Stoney, “The Tension of Metallic Films Deposited by Electrolysis,” *Proc. R. Soc. Lond. A*, vol. 82, no. 553, pp. 172–175, May 1909.

[10] W. C. Oliver and G. M. Pharr, “Improved technique for determining hardness and elastic modulus using load and displacement sensing indentation experiments,” *Journal of materials research*, vol. 7, no. 6, pp. 1564–1583, 1992.

[11] W. Daves, A. Krauss, N. Behnel, V. Häublein, A. Bauer, and L. Frey, “Amorphous silicon carbide thin films (a-SiC:H) deposited by plasma-enhanced chemical vapor deposition as protective coatings for harsh environment applications,” *Thin Solid Films*, vol. 519, no. 18, pp. 5892–5898, Jul. 2011.

[12] R. Dabkowski, “Installation of a New Electron Cyclotron Plasma Enhanced Chemical Vapour Deposition (ECR-PECVD) Reactor and a Preliminary Study ofThin Film Depositions,” *Open Access Dissertations and Theses. Paper 6974.*, Jan. 2012.

[13] K. Dunn, “Luminescent SiCxNy Thin Films Deposited by ICP-CVD,” *Open Access Dissertations and Theses Paper 5818.*, Oct. 2011.

[14] J. Li, O. H. Y. Zalloum, T. Roschuk, C. L. Heng, J. Wojcik, and P. Mascher, “Light emission from rare-earth doped silicon nanostructures,” *Advances in Optical Technologies*, vol. 2008, 2008.

[15] J. Li, O. Zalloum, T. Roschuk, C. Heng, J. Wojcik, and P. Mascher, “The formation of light emitting cerium silicates in cerium-doped silicon oxides,” *Applied Physics Letters*, vol. 94, no. 1, pp. 011112–011112–3, Jan. 2009.

[16] P. Wilson, “Effect of thermal treatment on the growth, structure and luminescence of nitride-passivated silicon nanoclusters,” *Nanoscale Research Letters*, vol. 6, no. 1, pp. 1–12, Dec. 2011.

[17] M. Ohring, *Materials science of thin films: deposition and structure*, 2nd ed. San Diego, CA: Academic Press, 2002.

[18] J. J. Vlassak and W. D. Nix, “New bulge test technique for the determination of Young’s modulus and Poisson’s ratio of thin films,” *Journal of Materials Research*, vol. 7, no. 12, pp. 3242–3249, 1992.

[19] C. B. Carter, *Ceramic materials: science and engineering*. New York: Springer, 2012.

[20] A. Leyland and A. Matthews, “On the significance of the H/E ratio in wear control: a nanocomposite coating approach to optimised tribological behaviour,” *Wear*, vol. 246, no. 1–2, pp. 1–11, Nov. 2000.

[21] H. K. Pulker, A. J. Perry, and R. Berger, “Adhesion,” *Surface Technology*, vol. 14, no. 1, pp. 25–39, Sep. 1981.

[22] P. A. Steinmann and H. E. Hintermann, “A review of the mechanical tests for assessment of thin-film adhesion,” *Journal of Vacuum Science & Technology A: Vacuum, Surfaces, and Films*, vol. 7, no. 3, pp. 2267–2272, 1989.

[23] K. G. Budinski, “Guide to friction, wear and erosion testing,” 2007. .

[24] J. Halling, “The tribology of surface films,” *Thin Solid Films*, vol. 108, no. 2, pp. 103–115, Oct. 1983.

[25] M. El Khakani, M. Chaker, A. Jean, S. Boily, J. C. Kieffer, M. E. O’hern, M. F. Ravet, and F. Rousseaux, “Hardness and Young’s modulus of amorphous a-SiC thin films determined by nanoindentation and bulge tests,” *Journal of materials research*, vol. 9, no. 1, pp. 96–103, 1994.

[26] K. H. Jack, “Sialons and related nitrogen ceramics,” *Journal of materials science*, vol. 11, no. 6, pp. 1135–1158, 1976.

[27] T. Ekstroem and M. Nygren, “SiAION ceramics,” *Journal of the American Ceramic Society*, vol. 75, no. 2, pp. 259–276, 1992.

[28] J. W. H. Van Krevel, J. W. T. Van Rutten, H. Mandal, H. T. Hintzen, and R. Metselaar, “Luminescence Properties of Terbium-, Cerium-, or Europium-Doped< i> α</i>-Sialon Materials,” *Journal of Solid State Chemistry*, vol. 165, no. 1, pp. 19–24, 2002.

[29] R.-J. Xie, M. Mitomo, K. Uheda, F.-F. Xu, and Y. Akimune, “Preparation and Luminescence Spectra of Calcium-and Rare-Earth (R= Eu, Tb, and Pr)-Codoped α-SiAlON Ceramics,” *Journal of the American Ceramic Society*, vol. 85, no. 5, pp. 1229–1234, 2002.

[30] N. Hirosaki, R.-J. Xie, K. Kimoto, T. Sekiguchi, Y. Yamamoto, T. Suehiro, and M. Mitomo, “Characterization and properties of green-emitting β-SiAlON: Eu 2+ powder phosphors for white light-emitting diodes,” *Applied Physics Letters*, vol. 86, no. 21, pp. 211905–211905, 2005.

[31] K. Sakuma, K. Omichi, N. Kimura, M. Ohashi, D. Tanaka, N. Hirosaki, Y. Yamamoto, R.-J. Xie, and T. Suehiro, “Warm-white light-emitting diode with

yellowish orange SiAlON ceramic phosphor,” *Optics letters*, vol. 29, no. 17, pp. 2001–2003, 2004.

[32] R.-J. Xie, N. Hirosaki, K. Sakuma, Y. Yamamoto, and M. Mitomo, “Eu 2+-doped Ca-α-SiAlON: A yellow phosphor for white light-emitting diodes,” *Applied physics letters*, vol. 84, no. 26, pp. 5404–5406, 2004.

[33] R.-J. Xie, N. Hirosaki, M. Mitomo, K. Sakuma, and N. Kimura, “Wavelength-tunable and thermally stable Li-α-sialon: Eu 2+ oxynitride phosphors for white light-emitting diodes,” *Applied physics letters*, vol. 89, no. 24, pp. 241103–241103, 2006.

[34] S. Dreer, “Quantitative analysis of silicon-and aluminium-oxynitride films with EPMA, SIMS, hf-SNMS, hf-GD-OES and FT-IR,” *Fresenius' journal of analytical chemistry*, vol. 365, no. 1–3, pp. 85–95, 1999.

[35] S. Dreer, R. Krismer, P. Wilhartitz, and G. Friedbacher, “Statistical evaluation of refractive index, growth rate, hardness and Young’s modulus of aluminium oxynitride films,” *Thin Solid Films*, vol. 354, no. 1–2, pp. 43–49, Oct. 1999.

[36] T. Akiyama, D. Collard, and H. Fujita, “Scratch drive actuator with mechanical links for self-assembly of three-dimensional MEMS,” *Journal of Microelectromechanical Systems*, vol. 6, no. 1, pp. 10–17, 1997.

[37] A. Kaushik, H. Kahn, and A. H. Heuer, “Wafer-level mechanical characterization of silicon nitride MEMS,” *Journal of Microelectromechanical Systems*, vol. 14, no. 2, pp. 359–367, 2005.

[38] V. Bhatt and S. Chandra, “Silicon Nitride Films Deposited by RF Sputtering for Microstructure Fabrication in MEMS,” *Journal of Elec Materi*, vol. 38, no. 9, pp. 1979–1989, Sep. 2009.

[39] M. Vila, D. Cáceres, and C. Prieto, “Mechanical properties of sputtered silicon nitride thin films,” *Journal of Applied Physics*, vol. 94, no. 12, pp. 7868–7873, Dec. 2003.

[40] B.-S. Yau and J.-L. Huang, “Effects of nitrogen flow on R.F. reactive magnetron sputtered silicon nitride films on high speed steel,” *Surface and Coatings Technology*, vol. 176, no. 3, pp. 290–295, Jan. 2004.

[41] R. A. Levy, X. Lin, J. M. Grow, H. J. Boeglin, and R. Shalvoy, “Low pressure chemical vapor deposition of silicon nitride using the environmentally friendly tris(dimethylamino)silane precursor,” *Journal of Materials Research*, vol. 11, no. 06, pp. 1483–1488, 1996.

[42] Y.-G. Jung, B. R. Lawn, M. Martyniuk, H. Huang, and X. Z. Hu, “Evaluation of elastic modulus and hardness of thin films by nanoindentation,” *Journal of Materials Research*, vol. 19, no. 10, pp. 3076–3080, 2004.

[43] K. J. Winchester and J. M. Dell, “Nano-indentation characterisation of PECVD silicon nitride films,” in *Proceedings Conference on Optoelectronic and Microelectronic Materials and Devices, 2000. COMMAD 2000*, 2000, pp. 117–120.

[44] H. Huang, K. J. Winchester, A. Suvorova, B. R. Lawn, Y. Liu, X. Z. Hu, J. M. Dell, and L. Faraone, “Effect of deposition conditions on mechanical properties of low-temperature PECVD silicon nitride films,” *Materials Science and Engineering: A*, vol. 435–436, pp. 453–459, Nov. 2006.

[45] P.-H. Wu, I.-K. Lin, H.-Y. Yan, K.-S. Ou, K.-S. Chen, and X. Zhang, “Mechanical property characterization of sputtered and plasma enhanced chemical deposition (PECVD) silicon nitride films after rapid thermal annealing,” *Sensors and Actuators A: Physical*, vol. 168, no. 1, pp. 117–126, Jul. 2011.

[46] M. Mehregany and C. A. Zorman, “SiC MEMS: opportunities and challenges for applications in harsh environments,” *Thin Solid Films*, vol. 355–356, pp. 518–524, Nov. 1999.

[47] P. M. Sarro, “Silicon carbide as a new MEMS technology,” *Sensors and Actuators A: Physical*, vol. 82, no. 1–3, pp. 210–218, May 2000.

[48] N. Ledermann, J. Baborowski, P. Muralt, N. Xantopoulos, and J.-M. Tellenbach, “Sputtered silicon carbide thin films as protective coating for MEMS applications,” *Surface and Coatings Technology*, vol. 125, no. 1–3, pp. 246–250, Mar. 2000.

[49] B. K. Gupta and B. Bhushan, “Micromechanical properties of amorphous carbon coatings deposited by different deposition techniques,” *Thin Solid Films*, vol. 270, no. 1–2, pp. 391–398, Dec. 1995.

[50] B. Bhushan, B. K. Gupta, and M. H. Azarian, “Nanoindentation, microscratch, friction and wear studies of coatings for contact recording applications,” *Wear*, vol. 181–183, Part 2, pp. 743–758, Mar. 1995.

[51] X.-A. Fu, J. L. Dunning, C. A. Zorman, and M. Mehregany, “Polycrystalline 3C-SiC thin films deposited by dual precursor LPCVD for MEMS applications,” *Sensors and Actuators A: Physical*, vol. 119, no. 1, pp. 169–176, Mar. 2005.

[52] K. M. Jackson, J. Dunning, C. A. Zorman, M. Mehregany, and W. N. Sharpe, “Mechanical Properties of Epitaxial 3C Silicon Carbide Thin Films,” *Journal of Microelectromechanical Systems*, vol. 14, no. 4, pp. 664–672, 2005.

[53] Y. Yamaguchi, H. Nagasawa, T. Shoki, N. Annaka, and H. Mitsui, “Properties of heteroepitaxial 3C-SiC films grown by LPCVD,” *Sensors and Actuators A: Physical*, vol. 54, no. 1–3, pp. 695–699, Jun. 1996.

[54] A. F. Flannery, N. J. Mourlas, C. W. Storment, S. Tsai, S. H. Tan, J. Heck, D. Monk, T. Kim, B. Gogoi, and G. T. A. Kovacs, “PECVD silicon carbide as a chemically resistant material for micromachined transducers,” *Sensors and Actuators A: Physical*, vol. 70, no. 1–2, pp. 48–55, Oct. 1998.

[55] O. K. Porada, V. I. Ivashchenko, L. A. Ivashchenko, G. V. Rusakov, S. N. Dub, and A. I. Stegnij, “a-SiC:H films as perspective wear-resistant coatings,” *Surface and Coatings Technology*, vol. 180–181, pp. 122–126, Mar. 2004.

[56] R. E. Franklin, “Crystallite growth in graphitizing and non-graphitizing carbons,” *Proceedings of the Royal Society of London. Series A. Mathematical and Physical Sciences*, vol. 209, no. 1097, pp. 196–218, 1951.

[57] W. Kern, “Cleaning solutions based on hydrogen peroxide for use in silicon semiconductor technology,” *RCA review*, vol. 31, pp. 187–206, 1970.

[58] W. Kern, “The Evolution of Silicon Wafer Cleaning Technology,” *J. Electrochem. Soc.*, vol. 137, no. 6, pp. 1887–1892, Jun. 1990.

[59] J. R. Vig and J. LeBus, “UV/Ozone Cleaning of Surfaces,” *IEEE Transactions on Parts, Hybrids, and Packaging*, vol. 12, no. 4, pp. 365–370, 1976.

[60] *Handbook of semiconductor manufacturing technology*, 2nd ed. Boca Raton: CRC Press, 2008.

[61] *Handbook of thin-film deposition processes and techniques: principles, methods, equipment, and applications*. Park Ridge, N.J., U.S.A: Noyes Publications, 1988.

[62] *Plasma deposited thin films*. Boca Raton, Fla: CRC Press, 1986.

[63] S. E. Alexandrov, “Remote PECVD : a Route to Controllable Plasma Deposition,” *Le Journal de Physique IV*, vol. 05, no. C5, pp. C5–567–C5–582, Jun. 1995.

[64] *Semiconductor manufacturing handbook*. New York: McGraw-Hill, 2005.

[65] M. Gupta, V. K. Rathi, R. Thangaraj, O. P. Agnihotri, and K. S. Chari, “The preparation, properties and applications of silicon nitride thin films deposited by plasma-enhanced chemical vapor deposition,” *Thin Solid Films*, vol. 204, no. 1, pp. 77–106, Sep. 1991.

[66] H. Zhang, *Study of optimal deposition conditions for an inductively coupled plasma chemical vapour deposition (ICP-CVD) system*. McMaster University, 2005.

[67] J. Asmussen, “Electron cyclotron resonance microwave discharges for etching and thin-film deposition,” *Journal of Vacuum Science & Technology A: Vacuum, Surfaces, and Films*, vol. 7, no. 3, pp. 883–893, 1989.

[68] National Center for Biotechnology Information, “PubChem Substance Database; SID=24864697.” Sigma-Aldrich, 14-May-2011.

[69] J. A. Woollam, B. Johs, C. M. Herzinger, J. Hilfiker, R. Synowicki, and C. L. Bungay, “Overview of variable angle spectroscopic ellipsometry (VASE), part I: basic theory and typical applications,” *Proc. SPIE CR72*, pp. 3–28, 1999.

[70] H. Tompkins and E. A. Irene, *Handbook of ellipsometry*. William Andrew, 2005.

[71] J. N. Hilfiker, C. L. Bungay, R. A. Synowicki, T. E. Tiwald, C. M. Herzinger, B. Johs, G. K. Pribil, and J. A. Woollam, “Progress in spectroscopic ellipsometry: Applications from vacuum ultraviolet to infrared,” in *Papers from the 49th International Symposium of the American Vacuum Society*, 2003, vol. 21, pp. 1103–1108.

[72] E. D. Palik, *Handbook of optical constants of solids*, vol. 3. Academic press, 1998.
[73] G. E. Jellison and F. A. Modine, “Parameterization of the optical functions of amorphous materials in the interband region,” *Applied Physics Letters*, vol. 69, no. 3, pp. 371–373, Jul. 1996.
[74] M. Mayer, “Rutherford backscattering spectrometry (RBS),” *Garching: Academic press, EURATOM Association*, 2003.
[75] J. Perrière, “Rutherford backscattering spectrometry,” *Vacuum*, vol. 37, no. 5–6, pp. 429–432, 1987.
[76] M. Mayer, “SIMNRA user’s guide,” Max-Planck-Inst. für Plasmaphysik, 1997.
[77] W. Assmann, H. Huber, C. Steinhausen, M. Dobler, H. Glückler, and A. Weidinger, “Elastic recoil detection analysis with heavy ions,” *Nuclear Instruments and Methods in Physics Research Section B: Beam Interactions with Materials and Atoms*, vol. 89, no. 1–4, pp. 131–139, May 1994.
[78] H. J. Whitlow, G. Possnert, and C. S. Petersson, “Quantitative mass and energy dispersive elastic recoil spectrometry: Resolution and efficiency considerations,” *Nuclear Instruments and Methods in Physics Research Section B: Beam Interactions with Materials and Atoms*, vol. 27, no. 3, pp. 448–457, Jul. 1987.
[79] R. Johnson, “Energy-Dispersive X-Ray Microanalysis: An Introduction,” *Noran Instruments, Middleton WI*, 1999.
[80] J. Goldstein, D. E. Newbury, D. C. Joy, C. E. Lyman, P. Echlin, E. Lifshin, L. Sawyer, and J. R. Michael, *Scanning electron microscopy and X-ray microanalysis*. Springer, 2003.
[81] B. Hafner, “Energy Dispersive Spectroscopy on the SEM: A Primer,” *Characterization Facility, University of Minnesota*, pp. 1–26, 2006.
[82] D. Drouin, A. R. Couture, D. Joly, X. Tastet, V. Aimez, and R. Gauvin, “CASINO V2.42—A Fast and Easy-to-use Modeling Tool for Scanning Electron Microscopy and Microanalysis Users,” *Scanning*, vol. 29, no. 3, pp. 92–101, 2007.
[83] A. C. Fischer-Cripps, “Critical review of analysis and interpretation of nanoindentation test data,” *Surface and Coatings Technology*, vol. 200, no. 14–15, pp. 4153–4165, Apr. 2006.
[84] A. C. Fischer-Cripps, *Nanoindentation*, 2nd ed. New York: Springer, 2004.
[85] W. C. Oliver and G. M. Pharr, “Measurement of Hardness and Elastic Modulus by Instrumented Indentation: Advances in Understanding and Refinements to Methodology,” *Journal of Materials Research*, vol. 19, no. 01, pp. 3–20, 2004.
[86] J. Menčík, D. Munz, E. Quandt, E. R. Weppelmann, and M. V. Swain, “Determination of elastic modulus of thin layers using nanoindentation,” *Journal of Materials Research*, vol. 12, no. 09, pp. 2475–2484, 1997.

[87] R. Saha and W. D. Nix, “Effects of the substrate on the determination of thin film mechanical properties by nanoindentation,” *Acta Materialia*, vol. 50, no. 1, pp. 23–38, Jan. 2002.

[88] V. Bellido-González, N. Stefanopoulos, and F. Deguilhen, “Friction monitored scratch adhesion testing,” *Surface and Coatings Technology*, vol. 74–75, Part 2, pp. 884–889, Oct. 1995.

[89] S. . Bull and D. . Rickerby, “New developments in the modelling of the hardness and scratch adhesion of thin films,” *Surface and Coatings Technology*, vol. 42, no. 2, pp. 149–164, Nov. 1990.

[90] S. J. Bull, “Failure modes in scratch adhesion testing,” *Surface and Coatings Technology*, vol. 50, no. 1, pp. 25–32, 1991.

[91] R. P. Nair, D. Griffin, and N. X. Randall, “The use of the pin-on-disk tribology test method to study three unique industrial applications,” *Wear*, vol. 267, no. 5–8, pp. 823–827, Jun. 2009.

[92] D. N. Wright, E. S. Marstein, A. Rognmo, and A. Holt, “Plasma-enhanced chemical vapour-deposited silicon nitride films; The effect of annealing on optical properties and etch rates,” *Solar Energy Materials and Solar Cells*, vol. 92, no. 9, pp. 1091–1098, Sep. 2008.

[93] B. von Blanckenhagen, D. Tonova, and J. Ullmann, “Application of the Tauc-Lorentz Formulation to the Interband Absorption of Optical Coating Materials,” *Appl. Opt.*, vol. 41, no. 16, pp. 3137–3141, Jun. 2002.

[94] M. P. Hughey and R. F. Cook, “Massive stress changes in plasma-enhanced chemical vapor deposited silicon nitride films on thermal cycling,” *Thin Solid Films*, vol. 460, no. 1–2, pp. 7–16, Jul. 2004.

[95] K. Matoy, H. Schönherr, T. Detzel, T. Schöberl, R. Pippan, C. Motz, and G. Dehm, “A comparative micro-cantilever study of the mechanical behavior of silicon based passivation films,” *Thin Solid Films*, vol. 518, no. 1, pp. 247–256, Nov. 2009.

[96] M. Ishii, K. Nakashima, I. Tajima, and M. Yamamoto, “Properties of silicon surface cleaned by hydrogen plasma,” *Applied Physics Letters*, vol. 58, no. 13, pp. 1378–1380, Apr. 1991.

[97] K. Nakashima, M. Ishii, T. Hayakawa, I. Tajima, and M. Yamamoto, “Effects of substrate temperature and ion incident energy on silicon surface cleaning using a hydrogen plasma excited by electron cyclotron resonance,” *Journal of Applied Physics*, vol. 74, no. 11, pp. 6936–6940, Dec. 1993.

[98] Z.-H. Zhou, E. S. Aydil, R. A. Gottscho, Y. J. Chabal, and R. Reif, “Real-Time, In Situ Monitoring of Room-Temperature Silicon Surface Cleaning Using Hydrogen and Ammonia Plasmas,” *J. Electrochem. Soc.*, vol. 140, no. 11, pp. 3316–3321, Nov. 1993.